Univerzita Karlova v Praze
Matematicko-fyzikální fakulta

DIPLOMOVÁ PRÁCE

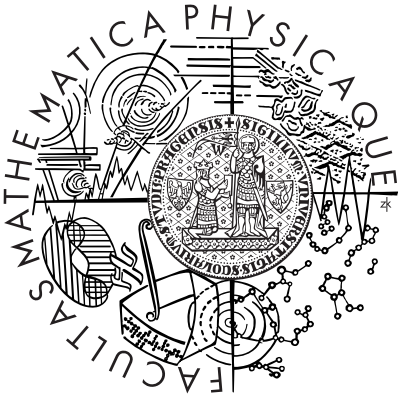

Bc. Michal Vališka

Supravodivost a magnetismus uranových sloučenin

Katedra fyziky kondenzovaných látek

Vedoucí diplomové práce: RNDr. Jiří Pospíšil, Ph.D.

Studijní program: Fyzika kondenzovaných soustav a materiálů

Studijní obor: Fyzika atomových a elektronových struktur

Praha 2013

Charles University in Prague
Faculty of Mathematics and Physics

MASTER THESIS

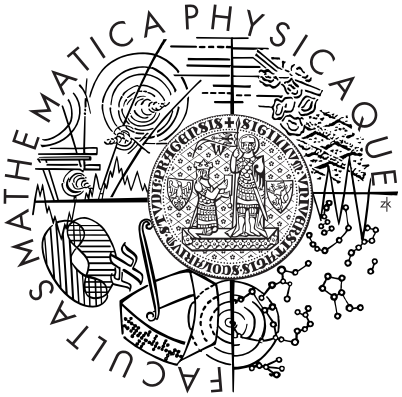

Bc. Michal Vališka

Superconductivity and Magnetism of Uranium Compounds

Department of Condensed Matter Physics

Supervisor of the master thesis: RNDr. Jiří Pospíšil, Ph.D.

Study programme: Condensed Matter and Material Physics

Specialization: Atomic and Electron Structure Physics

Prague 2013

First of all I would like to thank very much to my supervisor RNDr. Jiří Pospíšil, Ph.D. for his helpful support, time, advices and indispensable guidance in my work. Further I want to thank to prof. RNDr. Vladimír Sechovský, DrSc. for his valuable comments and suggestions. Then I would like also to thank to RNDr. Jan Prokleška, Ph.D. for his time and help with the experiments in JLMS. I am really grateful to the local contacts in ILL Grenoble, namely Gwilherm Nénert, Ph.D. and Anne Stunault, Ph.D. for their help with the neutron diffraction experiments and consequent data treatment. On the same place I have to thank to Dr. Karel Prokeš, DrSc. for his worthy recommendations used within the neutron diffraction experiments. Special thanks also belongs to the Dipl.-Ing. Martin Kriegisch and Dr. Herbert Müller from IFP - TU Vienna for their help with dilatometry measurements. I sincerely thank to Ing. Barbora Vondráčková for her time spent with sample preparation.

Last but not the least, I would like to thank to my family and my girlfriend who gave me their support at all times for the successful completion of this thesis.

I declare that I carried out this master thesis independently, and only with the cited sources, literature and other professional sources.

I understand that my work relates to the rights and obligations under the Act No. 121/2000 Coll., the Copyright Act, as amended, in particular the fact that the Charles University in Prague has the right to conclude a license agreement on the use of this work as a school work pursuant to Section 60 paragraph 1 of the Copyright Act.

In Prague date 12.4.2013

Bc. Michal Vališka

Název práce: Supravodivost a magnetismus uranových sloučenin

Autor: Bc. Michal Vališka

Katedra / Ústav: Katedra fyziky kondenzovaných látek

Vedoucí diplomové práce: RNDr. Jiří Pospíšil, Ph.D., Katedra fyziky kondenzovaných látek

Abstrakt: Cílem této práce je studium systému $UCo_{1-x}Ru_xGe$ nacházejícího se na rozhraní magnetické nestability. Podrobná studie magnetických a transportních vlastností polykrystalů s různým obsahem ruthenia odhalila komplexní změnu fyzikálních parametrů v rámci celé série. UCoGe je slabý ferromagnet s $T_C \sim 3\,K$ a malým magnetickým momentem $0,035\,\mu_B$/f.u. Pozorovali jsme strmý nárůst těchto hodnot až po hodnotu koncentrace ruthenia $x_{max} \approx 0,1 (T_{C,max} = 9\,K$ a $\mu_0 = 0,11\,\mu_B)$. Podstata tohoto nárůstu byla studována na mono krystalu o složení $UCo_{0,88}Ru_{0,12}Ge$ získaném metodou plovoucí zóny. Difrakce polarizovaných neutronů provedená na tomto krystalu se složením $UCo_{0,88}Ru_{0,12}Ge$ vysvětlila posílení magnetismu změnou vzájemné orientace magnetických momentů na iontu uranu a kobaltu. Antiparalelní uspořádání, které bylo dříve publikováno pro UCoGe je změněno na paralelní uspořádání v dopovaném $UCo_{0,88}Ru_{0,12}Ge$ kdy dojde k reorientaci momentu na kobaltu. Silná anizotropie $UCo_{0,88}Ru_{0,12}Ge$ se promítá do teplotní závislosti odporu a teplotní roztažnosti, které se dramaticky liší pro všechny tři osy. Tento prvotní nárůst T_C a magnetického momentu je následován poklesem směřujícím ke koncentraci $x_{cr} \approx 0,31$ kde magnetické uspořádání mizí. Podrobná studie kritických exponentů teplotních závislostí elektrického odporu, měrného tepla a koncentrační závislost T_C poukazují na přítomnost Non-Fermi liquid chování, které může značit existenci kvantově kritického bodu.

Klíčová slova: UCoGe, ferromagnetismus, difrakce polarizovaných neutronů, Kvantově kritický bod

Title: Superconductivity and Magnetism of Uranium Compounds

Author: Bc. Michal Vališka

Department: Department of Condensed Matter Physics

Supervisor: RNDr. Jiří Pospíšil, Ph.D., Department of Condensed Matter Physics

Abstract: This thesis studies the $UCo_{1-x}Ru_xGe$ system on the border of magnetic instability. Proper study of magnetic and transport properties of poly crystals with different ruthenium content revealed complex change of these parameters through the series. UCoGe is a weak ferromagnet with $T_C \sim 3\,K$ and low magnetic moment $0.035\,\mu_B$/f.u.. We observed rapid increase of these two quantities up to the concentration of ruthenium of $x_{max} \approx 0.1$. Background of this increase was studied on the single crystal grown by floating zone method. Polarized neutron diffraction experiment performed on this single crystal with composition of $UCo_{0.88}Ru_{0.12}Ge$ explained strengthening of magnetism with a change of mutual orientation of magnetic moments on the uranium and cobalt site. Previously reported antiparallel alignment for the UCoGe is changed to the parallel orientation for the doped $UCo_{0.88}Ru_{0.12}Ge$ when cobalt moment is reoriented. Strong anisotropy of the $UCo_{0.88}Ru_{0.12}Ge$ projects to the temperature dependence of resistivity and to the thermal expansion properties. This primal increase of T_C and magnetic moment is followed by decrease when approaching the concentration $x_{cr} \approx 0.31$ where magnetic order disappears. Closer study of the critical exponents of temperature dependencies of resistivity, specific heat and the concentration dependency of the T_C are pointing on the presence of Non-Fermi liquid behavior possibly indicating the presence of the Quantum Critical Point.

Keywords: UCoGe, ferromagnetism, polarized neutron diffraction, Quantum Critical Point

Contents

1 Introduction

Intermetallic compounds are subject of a careful scientific interest. This endeavor is motivated by the fact, that there is an almost unrestricted number of compounds which already have been or in future can be synthesized. And all these systems bring a palette of even higher number of interesting physical properties that they can exhibit. The aim of the primary research is to describe and interpret the results of various experiments together with the theoretical predictions in order to fully understand the nature of the physical processes.

The process of deeper understanding of some physical phenomena can lead to the point where appropriate theories reach their boundaries. Although they were valid for a broad group of systems and conditions the general validity is frequently lost due to new findings. A similar scenario arose in the case of superconductivity which is one of the subjects of this thesis. This physical phenomena was discovered by Heike Kamerlingh Onnes in 1911 on the example of pure mercury [1] when its resistivity drops down to the zero value at $T_{\mathrm{SC}} = 4.2\,\mathrm{K}$. It took more than 40 years till Bardeen, Cooper and Schrieffer came in 1957 with first microscopic theory (BCS)[2, 3] describing superconductivity with the phonon-mediated condensation of Cooper pairs (paired anti-parallel in s-wave singlet states) which brings electrons (fermions) to the boson-like state. Discovery of first high-temperature superconductors by Karl Müller and Johannes Bednorz [4] revealed that BCS theory is not universal. Another fact indicating, that superconductivity has to be treated as a more complicated issue was its unexpected coexistence with magnetic order, because these two phenomena were supposed to exclude each other. Hints for this coexistence can be traced back to the discovery of SC in Chevrel phases like $RE\mathrm{Mo_6S_8}$ [5] which contains magnetic ions or $\mathrm{ErRh_4B_4}$ where long range ferromagnetic order below 1K destroys the superconducting state which sets on at 9K [6]. Next step was the discovery of heavy fermion compound $\mathrm{CeCu_2Si_2}$ [7] where the interplay between antiferromagnetism and superconductivity of d-wave spin singlet nature was a big surprise. But far the most striking was the report on coexistence of ferromagnetic order and superconductivity in $\mathrm{UGe_2}$ in the pressure range of $1.0 - 1.6\,\mathrm{GPa}$[8]. This was followed by similar evidence of coexistence in the case of a weak ferromagnet URhGe [9]. But in this case SC exists even in the ambient pressure. UIr also exhibits coexistence of SC and FM as has been discovered in 2004[10]. And this family of so called uranium based ferromagnetic superconductors is hitherto closed by the UCoGe[11] - an isostructural compound with URhGe. To date uranium based compounds are the only known ferromagnetic superconductors. In these compounds $5f$ electrons are believed to be itinerant and carrying both the superconductivity and ferromagnetic order. This breaks the standard BCS theory, because the field caused by ferromagnetism would destroy spin-singlet Cooper pairs. New mechanisms are proposed to bring these compound to SC state. Cooper pairs are thought to be in spin triplet-state where pairing mechanism is provided by critical spin fluctuations [12].

It is not only the coexistence of superconductivity and magnetism what makes the URhGe and UCoGe compounds so interesting. They belong to the broad family of UTX compounds where uranium $5f$ electrons are hybridized with d electrons of transition element T from the second half of $3d$, $4d$ or $5d$ series and X denotes one of the p elements. Various combinations of mentioned elements lead to different crystal structures and to broad set of magnetic ground-states and properties. We can observe hexagonal structure of $\mathrm{MgZn_2}$-type or ZrNiAl-type (the ordered variant of $\mathrm{Fe_2P}$-type structure) or the orthorhombic TiNiSi structure (derived from $\mathrm{CeCu_2}$) through the whole family.

Nevertheless examples of other hexagonal or even cubic structures can be found among UTX compounds as well[13]. Magnetically ordered compounds of this family are mostly strongly uniaxial systems with large magnetocrystalline anisotropy.

1.1 Motivation And Aim of the Thesis

This work is focused on the UCoGe compound in the frame of ruthenium doping on the cobalt place. Idea of this study is based on the ground state of the UCoGe itself. It has been already mentioned that it belongs to the group of ferromagnetic superconductors[11], but its magnetic ground state is more or less weak and subtle. In fact, former studies reported no magnetic ordering for UCoGe[14, 15]. It has been already shown, that applied external pressure can suppress its ordering temperature[16] same as for the case of UGe_2[8]. Nevertheless path to the increase of Curie temperature and to the overall stabilization of magnetic order leads to the transition metal doping. Pospíšil et al.[17] have shown that even small amount of different transition element on the site of cobalt dramatically increase robustness of magnetic order. This increase of T_C goes hand in hand with the lowering of temperature for superconducting transition, below the temperature of 0.4 K. URhGe as a second ambient pressure ferromagnetic superconductor offers similar increase of the ordering temperature[18]. It can be achieved by alloying with the isostructural URuGe compound which has paramagnetic ground state[14]. However further increase of ruthenium concentration leads to the suppression of ferromagnetism and whole system ends in the Quantum Critical Point where ordering temperature is zero.

Motivation of this thesis is to carefully study similar influence of ruthenium doping but on the UCoGe compound which itself lies in the vicinity of the ferromagnetic instability. While it is a unique example of very weak ferromagnet we expect that any change caused by doping would be more pronounced then in the case of magnetically more robust URhGe. We expect similar results to the study of U(Co, Fe)Ge system where alloying with paramagnetic UFeGe leads to the decrease of ordering temperature towards the Quantum Critical Point[19].

1.2 Outline of the Thesis

The work has nine parts including this Introduction. Second part brings brief theoretical overview of topics and terms used within this work. It is not focused on rigorous deriving of used models and theories, but it brings their digest recapitulation. Next part summarizes up to date information about uranium based ferromagnetic superconductors and report on magnetic properties of other members of the UTX family. Chapter 4 covers description of used experimental methods and techniques. Main stress is laid on the sample preparation, crystal growth and on the measurement techniques including neutron diffraction. All results, divided to the results on polycrystalline samples and on the single crystal study, are presented in the Chapter 5. These results are consequently discussed in following Chapter 6. Final conclusion can be found in Chapter 7 which is followed by an outlook in the Chapter 8 - Future Plans. Appendix A brings supplementary Arrott plots which meaning is described in the Chapter 5.

2 Theoretical Background

2.1 Localized and Itinerant Magnetism

2.1.1 Magnetic Moments of Free Ions

Atom in Applied Magnetic Field Magnetism of compounds is caused by magnetic moments of their atoms. Each electron at position $\boldsymbol{r}$ with momentum $\boldsymbol{p}$ in an atom has its own spin angular momentum $\boldsymbol{S}$ and the orbital angular momentum $\boldsymbol{r} \times \boldsymbol{p}$ which describes its movement. So total angular momentum for a whole atom $\boldsymbol{L}$ is given as a sum of all angular moments of the Z electrons in this atom.

$$\boldsymbol{L} = \frac{1}{\hbar} \sum_{i=1}^{Z} \boldsymbol{r_i} \times \boldsymbol{p_i} \tag{2.1}$$

The Hamiltonian $\widehat{\boldsymbol{\mathcal{H}_0}}$ for an isolated atom without the influence of magnetic field reflects kinetic energy $\frac{p_i^2}{2m_e}$ and potential energy V_i of each i^{th} electron [20]

$$\widehat{\boldsymbol{\mathcal{H}_0}} = \sum_{i=1}^{Z} \left(\frac{p_i^2}{2m_e} + V_i \right) \tag{2.2}$$

Presence of external magnetic field $\boldsymbol{B}$ leads to the more complicated form with two additional terms

$$\widehat{\boldsymbol{\mathcal{H}}} = \widehat{\boldsymbol{\mathcal{H}_0}} + \mu_B \left(\boldsymbol{L} + g\boldsymbol{S} \right) \boldsymbol{B} + \frac{e^2}{8m_e} \sum_{i=1}^{Z} \left(\boldsymbol{B} \times \boldsymbol{r_i} \right)^2 \tag{2.3}$$

where g is *g-factor*[20]. Second term $\mu_B \left(\boldsymbol{L} + g\boldsymbol{S} \right) \boldsymbol{B}$ quantifies magnetic moment of the atom itself and is called *paramagnetic term*. Third term $\frac{e^2}{8m_e} \sum_{i=1}^{Z} \left(\boldsymbol{B} \times \boldsymbol{r_i} \right)^2$ is *diamagnetic term*.

Diamagnetism If we assume an atom with all closed shells the *paramagnetic term* will be zero. In this case we can calculate magnetic susceptibility dependent purely on the *diamagnetic term*. For N identical ions of Z electrons in the volume V is this magnetic susceptibility given by the following equation

$$\chi = \frac{M}{H} = -\frac{Ne^2\mu_0}{V 6m_e} \sum_{i=1}^{Z} \langle r_i^2 \rangle \tag{2.4}$$

It is obviously negative so it leads to a negative response of material magnetization M on the applied magnetic field H. Although diamagnetism is purely quantum mechanical effect we can look on it as a analogy to the Lenz's law[21]. The diamagnetic susceptibility is generally weak effect that is present in every material in magnetic field. It is also mostly temperature independent. Important exception in this case are superconducting materials. They are from definition ideal diamagnets[22] with susceptibility $\chi = -1$ and this diamagnetic susceptibility is temperature independent. Diamagnetism is a natural property of the atoms (ions) with fully occupied electron shells (i.e. they have $L = S = 0$). Typical examples are inert gasses, metals like copper, gold, mercury, bismuth or compounds like water or petroleum.

Paramagnetism The ions with unpaired electrons in outer shell have L or S (or both) nonzero and therefore both the paramagnetic term (due tot the not fully occupied outer shell) and dia-

magnetic term (due to the closed inner shells) are nonzero. The paramagnetic term is usually temperature dependent and at sufficiently low temperatures much larger then the diamagnetic term. The paramagnetic term reflects existence of permanent magnetic moments which are present even irrespective to external magnetic field. The paramagnetic term is positive and yields positive susceptibility, i.e. positive response of magnetization to the external magnetic field. The applied field tends to align magnetic moments in the paramagnetic system in its own direction. We can expect, that higher field will easily align these moments and increase the magnetization and on the other hand thermal movement being enhanced with increasing temperature will serve in opposite way and reduce the magnetization. Thus the magnetization should be proportional to the ratio $\frac{B}{T}$ and hence the magnetic susceptibility of paramagnetic system should be inversely proportional to temperature.

Quantum mechanics and statistical physics treatment of the second term in Eq. (2.3) yields the magnetization proportional to the so called Brillouin function where $y = \frac{g_J \mu_B J \mu_0 H}{k_B T}$ and g_J is Landé g-factor

$$B_J(y) = \frac{2J+1}{2J} \coth\left(\frac{2J+1}{2J} y\right) - \frac{1}{2J} \coth\frac{y}{2J} \tag{2.5}$$

It covers both the case of $J = \infty$ where $B_\infty(y) = L(y)$ and also for $J = \frac{1}{2}$ we obtain $B_{\frac{1}{2}}(y) = \tanh y$. Restriction on small fields and not so low temperature leads again to the magnetic susceptibility that is inversely proportional to the temperature, which is expressed by Curie's law (2.6)

$$\chi = \frac{n\mu_0 \mu_{\text{eff}}^2}{3k_B T} = \frac{C}{T} \tag{2.6}$$

where proportionality is given by effective moment $\mu_{eff} = g_J \mu_B \sqrt{J(J+1)}$. In practice is susceptibility evaluated and studied in the limit of low field. High applied field would lead to the saturation of magnetization towards the value $\mu_{sat} = g_J \mu_B J$.

We would expect no paramagnetic effect for the state with $J = 0$, because linear paramagnetic term from the first-order perturbation theory would be equal to zero. However, second-order perturbation theory gives paramagnetic contribution to the susceptibility known as a *Van Vleck paramagnetism* [20]

$$\chi = \frac{2\mu_B^2 N}{V} \sum_n \frac{|\langle 0|\boldsymbol{L} + g\boldsymbol{S}|n\rangle|^2}{E_n - E_0} \tag{2.7}$$

This contribution to the susceptibility is rather small and temperature independent.

The susceptibilities mentioned above were not taking into account the contribution of conduction electrons. This has to be included when ion is embed into the metallic lattice. Particular chapter dealing with magnetism in materials is elaborated below. In a nutshell each electron in metal is polarized spin-up or spin-down. If the external magnetic field is applied the energy of an electron would be lowered or raised depending on the orientation of its spin towards the direction of the magnetic field. This is a base for so called *Pauli paramagnetism*. Magnetization of this system will be given as a difference between the number of spin-up $n_\uparrow$ and spin-down $n_\downarrow$ electrons with the density of states at Fermi level $g(E_F)$

$$M = \mu_B (n_\uparrow - n_\downarrow) = \mu_B^2 \mu_0 H g(E_F) \tag{2.8}$$

It leads to the almost temperature independent susceptibility

$$\chi_P = \frac{M}{H} = \mu_B^2 \mu_0 g\left(E_F\right) \tag{2.9}$$

Hund's Rules Many electrons in the atoms are in filled shells and do not contribute to net angular momentum. However, there can be also electrons in incomplete shells like d- or f-electrons where the individual moments are not canceled and form a nonzero net magnetic moment of an atom. Spin and orbital angular moments of all these unpaired electrons will be combined together and form total spin $\boldsymbol{S}$ and orbital $\boldsymbol{L}$ angular momentum of the atom. Naturally there exist a large number $((2S+1)(2L+1))$ of possible combinations of spin and orbital angular moments which will cost different amount of energy. The most energy favorable one can be estimated by applying the set of three empirical rules - *Hund's rules*[20]

First one is based on minimizing of Coulomb energy expressed by Pauli exclusion principle. Reduction of Coulomb repulsion between electrons is acquired by maximizing quantum number of *spin angular momentum* $\boldsymbol{S}$.

We can imagine that electrons rotating in orbits in the same direction can avoid meeting each other more successfully then if they rotate in opposite way. Thus another reduce of Coulomb repulsion can be achieved by maximizing of *orbital angular momentum* $\boldsymbol{L}$.

Minimizing of spin-orbit energy is a fundamental point of a third Hund's rule. It claims, that $\boldsymbol{J}$ has value of $|\boldsymbol{L}-\boldsymbol{S}|$ if the shell is less then half filled and $|\boldsymbol{L}+\boldsymbol{S}|$ for shell filled more than a half.

It has to be noticed, that third rule has limited extent of validity.Other energy terms can be more important then spin-orbit coupling for the real ions in a lattice. Typical example are transition metals were this third rule is mostly disobeyed. Contrary to that stay rare earth ions where Hund's rules are in very good agreement with experimental data. Details of this difference will be explained in following chapters.

2.1.2 Magnetic Moments in Lattice

As has been expressed in equation (2.6) the measurement of susceptibility of a paramagnet can give us the estimation of an effective magnetic moment on one single ion embed in a real lattice. If we compare the effective moment derived from experimental data with the corresponding values calculated from the Hund's rules we obtain satisfying agreement for the rare-earth compounds where magnetism is caused by the unfilled $4f$ shells. Exceptions are Sm and Eu ions where low lying excited states are also significantly populated causing the change of an effective magnetic moment[20]. As has been mentioned in previous paragraph, magnetism of $3d$ ions in lattice (i.e. $3d$ metals) cannot be described fully by Hund's rules. It is caused by high influence of crystal field of the surrounding ions on the studied one. This effect is not so important for $4f$ electrons because their spatial distribution is more centered on the atom and spin-orbit coupling plays the dominant role.

Up to now we have also considered that electrons are well localized on the atoms. It is not always true, specially in the case of metals where conduction electrons form bands and are delocalized over the lattice.

Band (Itinerant Electron) Magnetism Band magnetism is formed by delocalized electrons caused by overlapping of "magnetic" electron orbitals and bonding. It can be shown on the example of the iron atom. Magnetic moment is approximately $2.2\,\mu_B$[20] for this atom. This non-integer value is not compatible with localized moments. The measured magnetization is due to the different mechanism based on the spontaneous spin splitting. In this scenario we imagine moving some electrons near Fermi level (in the region of energy δE) from spin-up to spin-down band. It will lead to the increase of kinetic energy of $\frac{1}{2}g\left(E_F\right)\delta E^2$. This action itself would be energetically unfavorable, but interaction of arisen magnetization with molecular field would lead to the energy reduction. Further refinement of this situation leads to the so called *Stoner criterion*

$$Ug\left(E_F\right) \geq 1 \tag{2.10}$$

which decides whether previously mentioned formation of spontaneous band magnetism is energetically favorable and thus realized. Parameter U is a measure of Coulomb interaction and $g\left(E_F\right)$ is density of states at Fermi level.

Effects of the spin-split can also lead to the change of susceptibility. If we connect both effects from previous paragraph (change of kinetic energy and Coulomb repulsion) and applied magnetic field we obtain *Stoner enhanced susceptibility*

$$\chi_S = \frac{\mu_0\mu_B^2 g\left(E_f\right)}{1 - Ug\left(E_f\right)} = \frac{\chi_P}{1 - Ug\left(E_F\right)} \tag{2.11}$$

that is in fact Pauli susceptibility (Eq. (2.9)) enhanced by the factor of Stoner criterion ((2.10)). This Stoner model can partly solve the ferromagnetic order caused by spontaneous spin-splitting. Details of the magnetic ordering will be discussed in the following chapter. However it is not able to give realistic estimation for the ordering temperature. Better results can be obtained by *Spin fluctuations model*[21].

$3d$ transition metals can be taken as a representatives of the itinerant magnetism. Nevertheless pure itinerant electron magnetism is rare and hardly existing. Really close to this ideal state are $ZrZn_2$ or $NiAl_3$[21]. In other real materials exists certain degree of localization that has to be taken into account.

Localized Electron Magnetism In the limiting case of localized magnetism ions in the real material can be treated like the free ions. Nevertheless even the $4f$ states are involved in some interactions which are absent in the case of a free ions but we can assume them as a perturbation to the ionic magnetic moment which is localized. First one should consider the interaction of "magnetic orbitals" with the electric field (crystal electric field - CEF) caused by neighboring ions and valence electrons which can modify the magnetic symmetry and the size of magnetic moment in ions with nonzero orbital momentum. The magnetic exchange interaction with other magnetic ions can lead to some cooperative phenomena[21].

Magnetic properties of localized moments can be described by microscopic Hamiltonians with parameters which can be obtained either from theoretical approaches or from experimental data.

The ions of *rare earth metals* and some *actinides* can be considered as a typical carrier of localized magnetism in matter. Their incomplete f-shells stand behind their magnetic properties. Outer complete s and d shells are involved in chemical bonding and participate in forming of crystal

field for f electrons.

The theoretical approach used to study the localized magnetism starts with the treatment of a free ion Hamiltonian based on various approximations. Frequently used is *central field approximation* where f electrons move independently in the spherical potential of an ion.

Then follow some perturbations which are necessary for improvement of this idealized model. Strongest electrostatic interaction is *Coulomb interaction* as a repulsive force between f electrons. As a dominant magnetic interaction is assumed spin-orbit interaction quantifying the coupling of spin and orbital moments of the electrons. Systems with localized magnetism frequently exhibit strong magnetocrystalline anisotropy (i.e. magnetic properties differs for various directions in the system). The spin-orbit interaction together with the crystal field interaction are mostly responsible for the strong magnetocrystalline anisotropy in the rare earth materials. This effect is tightly bound to the point symmetry of the rare earth site in the crystal structure of the specific compound.

Appearance of magnetic cooperative phenomena depends on the competition between magnetic coupling of ions and thermal movement which tries to preserve random orientation of the moments. Details of possible types of magnetic ordering will be discussed below.

Uranium Magnetism Mechanisms of magnetism in U compounds is more complex since the U magnetic ($5f$) electron states are not localized but also usually far from being entirely itinerant. Therefore none of the two limiting models of magnetism can successfully describe magnetic properties of the uranium compounds. Delocalization of electrons leading to the band magnetism is reflected by the atomic volume decrease (i.e. electrons contribute to bonding). This effect can be seen in Fig 2.1. We can observe parabolic dependence of atomic volume for d elements connected with the population of bonding states and with forming of the itinerant magnetism. One can see somewhat higher values due to appearing magnetic ordering (splitting of the $3d$ spin up and spin down subband) for $3d$ elements between Mn and Ni. On the other hand weak variation of atomic volumes for almost all $4f$ elements due to the lanthanide contraction shows localized character of their electrons. Finally, actinides show crossover behavior where light $5f$ elements (up to the plutonium) resemble band like magnetism while the heavier ones like americium tend to be more localized. The reason for this behavior is a large spatial distribution of $5f$ electron wave functions in contrast to the localized $4f$ wave functions[21].

One can see that uranium magnetism is on the border between the localized and itinerant electron type. It is characterized (like the most of other $5f$ elements) by strong spin-orbit interaction which yields considerable orbital magnetic moments μ_L (even in the case of strong delocalization) which is antiparallel to the spin momentum μ_S[21]. It is in analogy with lanthanides and also with the third Hund's rule. Magnetic properties of uranium based compounds are strongly influenced by the hybridization of $5f$ states with surrounding ligands. It is also characterized by large magnetic anisotropy and high sensitivity of magnetic properties to the pressure, magnetic field, substitution and other external variables. Delocalization leads to the much smaller magnetic moment on the $5f$ ion site compared to the free ion. These materials also often exhibit large values of γ as an electronic contribution to the specific heat caused by high density of states at the Fermi level E_F.

Presence of magnetic order itself is mostly given by the direct overlapping of widely spread $5f$ electron functions. Large overlap of these electron functions for short distance of U atoms leads to the breaking of the Stoner criterion for magnetic order ($N(E_F)\, I \gg 1$). This observation shows

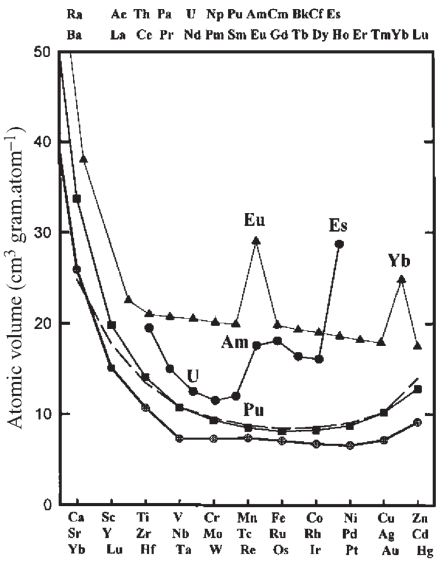

Figure 2.1: Evolution of atomic volume across 3d (hexagons), 4d (squares), 5d (dashed line), 4f (triangles), and 5f (circles) transition metal series. After Johansson and Skriver[23].

that the distance between two nearest Uranium atoms affects the possible existence of magnetic order was done by H.H. Hill[24]. There really exists certain distance between Uranium atoms called "Hill's limit" that separates non-magnetic (and sometimes superconducting) compounds like UCo, $\alpha-$U or URuGe and compounds with magnetic ground state like UGe_2Si_2. Critical distance is approximately in the range of $3.4-3.6$ Å. Magnetic properties of these compounds are not affected only by the $5f$-$5f$ overlap which is strengthened with the shortening of the distance between $5f$ ions. Transition elements in these compounds have strong influence on the exact type of eventual magnetic order as well. Thus the $5f$-nd hybridization has to be treated as a crucial factor. As has been mentioned in the Introduction, uranium-based ferromagnetic superconductors are a group of compounds exhibiting unique coexistence of ferromagnetic order and superconductivity. It is showing that this anomalous phenomena is observed in the vicinity of so called Quantum Critical Point (QCP).

These compounds and also other uranium based systems are the subjects of a huge number of studies which propose to reveal and understand the physical background of their interesting properties.

2.1.3 Exchange Interactions and Magnetic Ordering

Magnetic exchange interactions correlate magnetic moments and therefore stay behind formation of long range magnetic ordering. Exchange interaction energy exceeds the energy of thermal movement of magnetic moments and long range order can be formed, below some characteristic energy. *Exchange interactions* play a major role and have to be treated as a quantum mechanical effect. These interactions can be described by Heisenberg Hamiltonian[20]

$$\widehat{\mathcal{H}}_{ex} = -\sum_{i,j} J_{ij} \boldsymbol{S}_i \boldsymbol{S}_j \tag{2.12}$$

where J_{ij} is an exchange integral and $\boldsymbol{S_i}$ and $\boldsymbol{S_j}$ are localized magnetic spins vectors.

We can sort exchange interactions into the three following categories

Direct Exchange First one is called *direct exchange*. It is due to the fact that it acts directly without the need for any kind of intermediary. This type of interaction is often present in the case of $3d$, $4d$, $5d$ or $5f$ elements (Fe, Co, Ni, some U compounds, etc.) where we find substantial overlapping of wave functions of neighboring magnetic ions. It leads to the resulting value of exchange integral J_{ij} around $10^2 - 10^3$ K. This direct interaction is classified as a short range so it proceeds only between nearest neighbors.

Indirect Exchange - Superexchange The indirect exchange (superexchange) is exchange interaction acting among the non-neighboring magnetic ions while the interaction itself is caused by non-magnetic ions in between them. Exchange integral in this case is mostly smaller and reaches typical values of approximately$10^0 - 10^2$ K. Same as in the case of direct exchange it can be observed in $3d$, $4d$, $5d$ and $5f$ compounds, but it is also presented in the case of $4f$ compounds with p and d elements.

RKKY Interaction In fact rare earth elements and their compounds exhibit special type of indirect interaction called RKKY (after the authors of the theoretical description Ruderman, Kittel, Kasuya and Yosida)[25, 26, 27]. In this case interaction is mediated by polarized conduction electrons which interact with magnetic moments of $4f$ ions. Exchange integral is modulated with increasing distance $\boldsymbol{r}$ in oscillatory character described by equation[20]

$$\boldsymbol{J}_{\mathrm{RKKY}} \propto \frac{\cos(2k_{\mathrm{F}}r)}{\boldsymbol{r}^3} \tag{2.13}$$

where k_{F} is a radius of Fermi surface. Indirect interaction has a much longer range character than the previous cases. It is favorable interaction for $4f$ metals and their intermetallics.

All these exchange interactions can lead to the some kind of long-range ordering of magnetic moments.

Types of Magnetic Order

Ferromagnetism Ferromagnetism is characterized by spontaneous parallel alignment of all spins leading to the spontaneous magnetization even in the case of absent external magnetic field.

If we want to describe this ordered state we can consider the exchange interaction acting on the system as so called effective field. This is also denoted as Weiss molecular field $\boldsymbol{B}_{\mathrm{mf}}$. We can parametrize the strength of this molecular field with constant λ. It is temperature independent and positive value acting like a inverse susceptibility, i.e. it assumes linear dependence of molecular field on the magnetization

$$\boldsymbol{B}_{\mathrm{mf}} = \lambda \boldsymbol{M} \tag{2.14}$$

Now we enlarge magnetic field with the value of added external magnetic field $\boldsymbol{B}_{\mathrm{e}}$ and we rewrite

paramagnetic susceptibility from Curie law (Eq. (2.6))

$$\chi_{\mathrm{P}} = \frac{\mu_0 M}{(B_{\mathrm{e}} + B_{\mathrm{mf}})} = \frac{C}{T} \tag{2.15}$$

Application of linear change of external field from Eq. (2.14) gives equation with singularity at $T = C\lambda = \theta_{\mathrm{P}}$

$$\chi = \frac{M}{\mu_0 B_{\mathrm{e}}} = \frac{C}{T - C\lambda} \tag{2.16}$$

This temperature θ_{P} is called *Weiss temperature*. We can rewrite above equation in the form of well known *Curie-Weiss law*[20]

$$\chi = \frac{C}{T - \theta_{\mathrm{P}}} \tag{2.17}$$

It describes temperature dependence of paramagnetic susceptibility above the ordering temperature. We can also define *modified Curie-Weiss law*.

$$\chi = \frac{C}{T - \theta_{\mathrm{P}}} + \chi_0 \tag{2.18}$$

where χ_0 represents the temperature independent contribution to the paramagnetic susceptibility. In the case of simple ferromagnets the paramagnetic Curie temperature $\theta_{\mathrm{P}} \approx T_{\mathrm{C}}$ which is called *Curie temperature*. A typical temperature dependence of the spontaneous magnetization, paramagnetic susceptibility and inverse paramagnetic susceptibility for a ferromagnet is plotted in Figure 2.2.

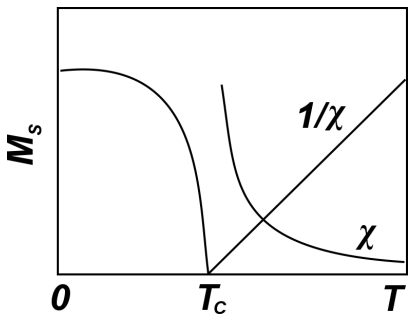

Figure 2.2: Temperature dependence of the susceptibility, inverse susceptibility and the spontaneous magnetization of a ferromagnetic material. T_{C} is the *Curie temperature*.

Antiferromagnetism Antiferromagnetic order is characterized by antiparallel alignment of adjacent magnetic moments. This is established at temperatures below *Néel temperature* (T_{N}). Antiferromagnet can be considered as being composed of two ferromagnetic and equivalent sublattices where magnetic moments of one sublattice points up and of the second one down.

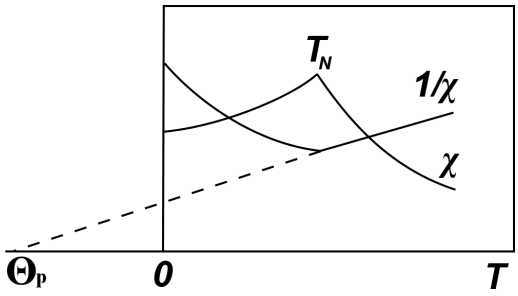

Figure 2.3: Temperature dependence of the susceptibility and inverse susceptibility of a antiferromagnetic material. θ_{P} is the *Weiss temperature.*

We can also define *magnetic susceptibility* in paramagnetic region as well [20], with C as a Curie constant

$$\chi = \frac{2C}{T + T_{\mathrm{N}}} \tag{2.19}$$

Typical temperature dependence of the magnetization and susceptibility for a antiferromagnet is plotted in Figure 2.3.

Relations for susceptibilities of paramagnets, ferromagnets and antiferromagnets can be generalized by general *Curie - Weiss law*

$$\chi \propto \frac{1}{T - \theta_{\mathrm{p}}} \tag{2.20}$$

There are three possible values for θ_{p}. For $\theta_{\mathrm{p}} = 0$ material is paramagnet, as mentioned above for $\theta_{\mathrm{p}} > 0$ we expect $\theta_{\mathrm{p}} = T_{\mathrm{C}}$ and it is ferromagnet and last case, for $\theta_{\mathrm{p}} < 0$ it exhibits antiferromagnetic order with the predicted value of ordering temperature $\theta_{\mathrm{p}} = -T_{\mathrm{N}}$. The relation between the Weiss temperature and the ordering temperature is not as simple and straightforward and must be treated individually in real compounds.

2.2 Non-Fermi Liquid Behavior and Quantum Phase Transitions

2.2.1 Quantum Phase Transitions

Quantum critical point (QCP) is kind of an exotic continuous phase transition which takes place at absolute zero temperature[28]. No thermal fluctuations can exist at zero temperature but nevertheless some phase transition can appear. This so called Quantum phase transition is based on quantum-mechanical fluctuations associated with Heisenberg´s uncertainty principle. Thus, even when random thermal fluctuations can not exist at zero temperature, atoms are not allowed to stay at rest because it would fix both their position and velocity. As a result of that quantum fluctuations - same as thermal movement - are able to melt the long range order. Its existence at zero temperature might make the Quantum phase transitions only theoretical problem without possible experimental evidence. It has its classical analog - Critical Point - as a part of phase diagram where ordinary continuous phase transition passes over. It means that symmetric or disordered system with some additional symmetry in Hamiltonian is turned to the broken-symmetry or ordered state, but Hamiltonian keeps its symmetrical form. A good example is transition from paramagnet to

Heisenberg ferromagnet[29]. Hamiltonian describing both states has rotational symmetry in spin space. This particular property is conserved only in the case of paramagnet. Ferromagnetic order spontaneously breaks this symmetry and chooses one preferred orientation for its spins. These ordinary phase transitions at finite temperature T_c are driven by random thermal fluctuations which lead to the divergence of correlation length ξ (typical length scale of short-range correlations present in disordered state and defined in Eq (2.21)).

$$\xi \propto \left(\frac{|T - T_c|}{T_c} \right)^{-\nu} \tag{2.21}$$

And it also develops the ordering parameter M on the boarder between the ordered and disordered phase. Spatial correlation of order parameter at T_c decays as a power law depending on the coefficient η (see Eq (2.22)).

$$\langle M(\mathbf{x}) M(\mathbf{y}) \rangle_{T=T_c} \propto |\mathbf{x} - \mathbf{y}|^{-d-2+\eta} \tag{2.22}$$

In this equation d stands for spatial dimension of the system.

Long-range correlations in space are followed by temporal effects in the system behavior. We can define equilibrium time τ_c measuring the time interval needed to recapture the equilibrium after the system was disturbed. This quantity also diverges at critical point and it can be related to the correlation length with power law dependence described by Eq. (2.23).

$$\tau_c \propto \xi^z \tag{2.23}$$

Reciprocal value of equilibrium time τ_c is a critical frequency scale ω_c which reflects the transition as it goes to zero value (Eq (2.24)).

$$\omega_c (T \to T_c) \propto 1/\tau_c \to 0 \tag{2.24}$$

Above mentioned exponents ν, z and also η are so called *critical exponents* and describes decays of some measurable properties near the critical point. There are three more critical exponents of power law dependence of other quantities near phase transition. First one is β that stands for the vanishing of the order parameter - Eq. (2.25)

$$M \left(\frac{|T - T_c|}{T_c} \to 0 \right) \propto \left(\frac{|T - T_c|}{T_c} \right)^{\beta} \tag{2.25}$$

Next one γ describes the order parameter susceptibility (i.e. magnetic susceptibility $\chi = M/H$) in Eq (2.26).

$$\chi \left(\frac{|T - T_c|}{T_c} \to 0 \right) \propto \left(\frac{|T - T_c|}{T_c} \right)^{-\gamma} \tag{2.26}$$

And last one is critical exponent δ which describes the dependence of the ordered parameter on the external field at criticality

$$M(T = T_c, B \to 0) \propto B^{1/\delta} \tag{2.27}$$

Temperature T_c of this thermal phase transition can be tuned by some non-temperature param-

eter δ like pressure, magnetic field or chemical doping down to the 0 K.

This observation can be explained on the example of the transition between disordered and ordered state. We can sketch the dependence of transition temperature T_c and control parameter δ. This phase diagram is plotted in Figure 2.4.

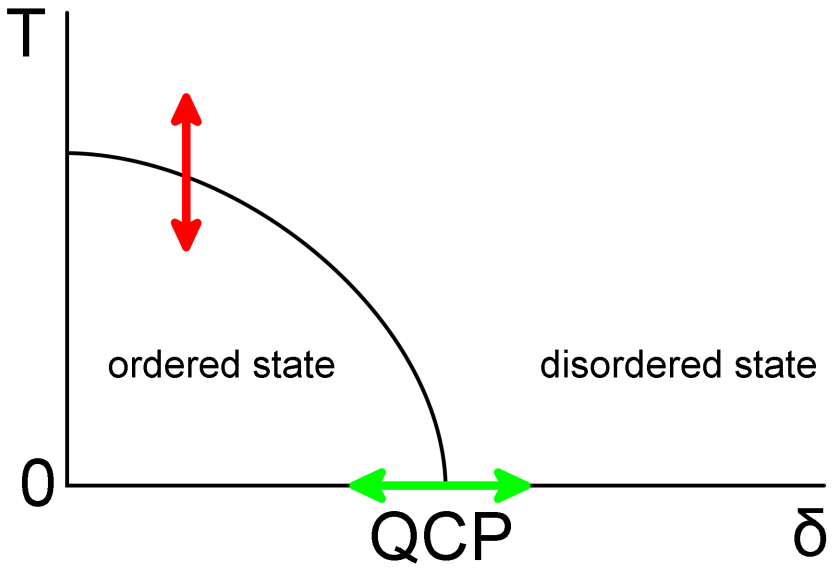

Figure 2.4: Schematic phase diagram showing a disordered and a ordered state. The path indicated by the red arrow represents a classical phase transition where temperature is changed while δ stays constant. Green arrow represents quantum phase transition at zero temperature while parameter δ is changed.

Set of critical points forming the coexistence curve $T_c(\delta)$ separates the ordered and disordered state in this phase diagram. In ordinary situation the parameter δ is fixed for each system and with temperature change going over the T_c the phase transition occurs. But nevertheless we can assume that in our material we can also change δ (with alloying, pressure change, magnetic field, etc.) so then for fixed temperature (and possibly even $T = 0\,\mathrm{K}$) we also perform phase transition.

Fortunately there is a possibility to observe the results of this phenomena even at the finite temperature. In the temperature region where $\hbar\omega > k_\mathrm{B}T$ quantum oscillations with typical frequency ω dominate the system so quantum critical region is spread above the QCP (see Fig 2.4).

2.2.2 Non-Fermi-Liquids (NFL)

The ordinary used Landau's Fermi liquid model brings temperature dependencies of some physical quantities at low temperatures (i.e. $< 1\,\mathrm{K}$)[30]. It predicts that for specific heat divided by temperature should be constant ($C/T \sim const.$). Analogous estimation is also made for temperature dependence of susceptibility ($\chi \sim const.$). The resistivity should exhibit some constant temperature independent value together with the term quadratic in temperature, i.e. $\rho = \rho_0 + AT^2$. This model correctly describes metallic behavior of physical properties at low temperatures where electron interactions should be temperature independent and are only short range. However these relations are not universally valid. Seaman et al. [31] observed almost linear temperature dependence of resistivity in the case of $Y_{1-x}U_xPd_3$. Ratio of the heat capacity and temperature also showed

	NFL theories					FL theory	
	AFM, $d=3$	AFM, $d=2$	FM, $d=3$	FM, $d=2$	Ref.		Ref
C/T	$\gamma - a\sqrt{T}$	$c\log(T_0/T)$	$c\log(T_0/T)$	$T^{-1/3}$	[33, 32]	$\gamma_0 T$	[36]
	$\gamma - aT^{1/2}$	$-\log T$	$-\log T$	$T^{-1/3}$	[34]		
	$\gamma + \sqrt{T}$	-	$-\log T$	$T^{-1/3}$	[35]		
χ	$T^{3/2}$	$\chi_0 - dT$			[33, 32]	χ_0	[36]
	$T^{-3/2}$	$-(\log T)/T$	$T^{-4/3}$	$-T^{-1}/\log T$	[34]		
	$T^{-3/2}$	-	$T^{-4/3}$	T^{-1}	[35]		
ρ	$T^{3/2}$	T	T		[33, 32]	$\rho_0 + AT^2$	[37]
	$T^{3/2}$	T	$T^{5/3}$	$T^{4/3}$	[34]		
	$T^{3/2}$	-	$T^{5/3}$	$T^{4/3}$	[35]		
$T_{C/N}$	$(\delta_c - \delta)^{2/3}$	$(\delta_c - \delta)$	$(\delta_c - \delta)^{3/4}$	$(\delta_c - \delta)$	[33, 32]		

Table 2.1: Comparison of temperature dependence for heat capacity, susceptibility, resistivity and ordering temperature according to some NFL theories with results for Landau's FL theory. We kept original notation from references.

rather logarithmic then constant progress. These results were not in agreement with Fermi liquid theory. We can call it Non-Fermi liquid behavior. However it has to be mentioned that not all phenomena not consistent with Fermi liquid theory are necessary Non-Fermi liquid behavior.

NFL behavior is quite often observed in the vicinity of a magnetically ordered state. Its position in phase diagram near magnetic instability at $T = 0\,\mathrm{K}$ is promising sign of a link between those two effects. We can find a number of theories dealing with the explanation of NFL behavior. They use general ideas of critical points in finite temperature to quantum critical phenomena and try to predict temperature properties of physical quantities at $T > 0\,\mathrm{K}$. In this work we present results of theoretical work of Hertz[32] and Millis[33] using renormalization-group theory, self-consistent renormalization study of Moriya and Takimoto[34] and also theory of Lonzarich [35]. All these spin-fluctuation theories give predictions of temperature dependence of resistivity, susceptibility and heat capacity. Moriya and Takimoto predicts dependence of ordering temperature on the control parameter δ mentioned above (not to be confused with critical exponent δ). Results of these theories are in general results in good agreement and are summarized and compared with the ordinary Fermi liquid behavior in Table 2.1.

2.3 Superconductivity

Superconductivity was discovered by Heike Kamerlingh Onnes in 1911 on mercury [1]. It was a result of giant advance in a low temperature physics that lead to the observation of a massive drop of resistance down to the zero below temperature of $\sim 4.2\,\mathrm{K}$. Zero resistivity is one of the two crucial properties of the superconductor. Second one is perfect diamagnetism. Both phenomena are realized below so called *critical temperature* (T_{SC}) [22]. At higher temperatures superconductors behave as an ordinary metal with rather low conductivity (lead, tin, ..). It has been also observed that typical band ferromagnets like Ni, Fe are not superconducting. Exception is non-magnetic structure type $\epsilon - \mathrm{Fe}$ that exhibit superconductivity below $2\,\mathrm{K}$ but only under the applied external pressure of the $15 - 30\,\mathrm{GPa}$[38].

2.3.1 Conventional Superconductivity

The study of superconductivity highly stimulated progress both on the field of experimental and theoretical physics. The above mentioned diamagnetic property of superconductors was first observed by Meissner and Ochsenfeld in 1933[39]. This perfect diamagnetism expels the magnetic flux from the inside of a superconductor - *Meissner effect*. Contrary to that some critical value of external magnetic field B_C exists that can destroy superconducting state. If it is connected with steep decrease of diamagnetism we can talk about Type I superconductor (See Fig. 2.5). Type I superconductors are by rule elements[40]. If the destabilization of diamagnetism is gradual we can distinguish two important values for external magnetic field (B_{C1} and B_{C2}). At first one (B_{C1}) diamagnetism starts to vanish and at the second one (B_{C2}) it is completely lost. It is also observed that so called *upper critical field* B_{C2} corresponds with the sharp increase of resistivity from zero up to some positive value (See Fig. 2.5). Compounds with these more complex properties are denoted as Type II superconductors. Examples of Type II superconductors are some elements and also alloys.

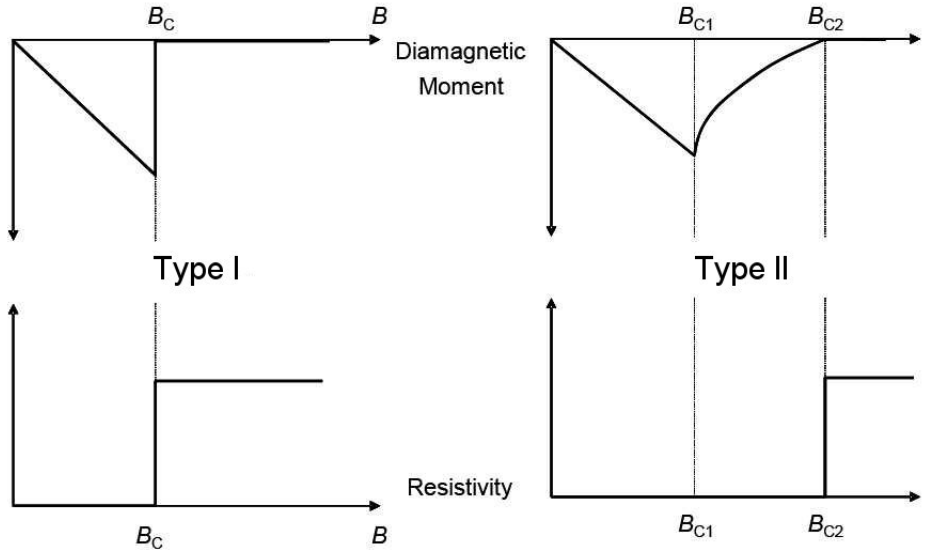

Figure 2.5: Field dependence of the resistivity and diamagnetic moment of Type I and Type II superconductors. B_C is the critical field.

Results of the microscopic BCS (after Bardeen, Cooper and Schrieffer Bardeen et al. [2, 3]) theory can be summarized to the simplified view on the emergence of superconductivity. Despite repulsive interaction between two electrons they can form a pair with opposite spin and momentum. This pairing is mediated by phonons and we can imagine it like polarization of positive ions behind one conduction electron passing through the matter that attracts another electron passing behind. It means that below certain temperature this attractive interaction can overcome repulsion between two electrons and they pair-up to the quantum state with zero angular and spin momentum. In fact they condensate in microscopic way in the momentum space. Thus they have zero and consequently integer spin they cannot be no longer treated by Fermi-Dirac, but according to the Bose-Einstein statistic. This pairing is due to its symmetry called s-wave and superconductors

which obey properties mentioned in this chapter are called *conventional superconductors.*

2.3.2 Unconventional Superconductivity

From the early beginning of the investigation of superconducting state was the critical temperature a crucial parameter. Nevertheless up to the 1980 the compound with the highest critical temperature was Nb_3Ge with 30 K[41]. Dramatic increase of maximal critical temperature is connected with the discovery of high T_{SC} cuprates by Bednorz and Müller[4]. Theoretical approaches which tried to describe these anomalously high ordering temperatures worked with idea, that superconducting state can be built even without the presence of electron-phonon interaction[42]. It seemed that strong electron-electron interaction would be the correct keystone for this kind of superconductors[22]. Contrary to the BCS theory where key property of electrons in Cooper pair was their charge causing the local displacement of positive ions in the case of unconventional superconductors is mostly important spin of the paired electrons. In conventional superconductors are spin paired together with opposite spins. As an unconventional superconductor we denote a system that has different symmetry of the energy gap for paired electrons in the momentum space or their electrons are paired in triplets. Spherical symmetry for the BCS theory stands for the s-wave. If this energy gap exhibits some point- or line-nodes or another zero regions it is a sign of unconventional d-wave, p-wave or even f-wave symmetry, respectively[43]. Thus unconventional superconductivity allows also to pair spins with the same orientation. In the case of ferromagnetic superconductors like UGe_2 we observe triplet pairing. From the three possibilities for triplet pairing only those two with equal spin are paired together. Mechanism, which glues electrons in this case are most probably quantum mechanical spin fluctuations or magnetically induced pairing[44]. The BCS theory deals with isotropic and spherical energy gap in the reciprocal space $\Delta(k)$ that exhibits the same symmetry as the Fermi surface of the system. Triplet pairing leads to lowering of the symmetry of the superconducting gap and thus it is no more isotropic and some line-nodes (polar symmetry) or point-nodes (axial symmetry) occur. Fay and Appel[12] found a coexistence of itinerant ferromagnetism and triplet paired superconductivity as a possible and they also predicted, that superconductivity can exist both in the ferromagnetic and paramagnetic phase - as can be seen in the case of UCoGe. Mineev [45] shows in his theoretical work based on the group theory that superconducting phase coexisting with ferromagnetic order could be of different nature than that one in the paramagnetic region.

3 Uranium Based Ferromagnetic Superconductors and Orthorhombic Members of the UTX Family

As has been mentioned in Introduction there exists group of compounds where superconductivity coexists with true itinerant ferromagnetism. These compounds are so called uranium based ferromagnetic superconductors and up to date we know four members of this family. These are UGe_2, UIr, URhGe and UCoGe. In the case of UGe_2 and UIr superconductivity is observed only when external pressure is applied. On the other hand URhGe and UCoGe are ambient pressure superconductors and members of UTX family as well. Later paragraphs will summarize basic properties of the UGe_2 compound for its historical importance as the first ferromagnetic superconductor. Ambient pressure superconductors will be discussed in the frame of other orthorhombic compounds which belongs to the UTX group. Therefore their magnetic properties will be discussed in detail as well.

3.1 UGe_2 - The First Ferromagnetic Superconductor Under Pressure

This compound posses the orthorhombic structure where U atoms forms zig-zag chain along the a axis. Shortest distance between two nearest U atoms is $d_{U-U} = 3.85\,\text{Å}$ which is quite far from the Hill's limit on the side where magnetism is expected. This quantity seems to be very important for the basic properties of magnetic order in uranium based intermetallics. UGe_2 orders ferromagnetically at $T_C = 52\,\text{K}$[46]. Ferromagnetic order with magnetic moments on the uranium sites ($\sim 1.5\,\mu_B$) aligned along the a axis can be suppressed by pressure. We can observe paramagnetic behavior (PM) above the critical pressure of 1.5 GPa[47]. This suppression is followed by surprising appearance of superconductivity at 1 GPa. With higher pressure the temperature of SC transition is increased and reaches its maximal value $T_{sc} \approx 0.7\,\text{K}$ at 1.2 GPa[8]. It means that this compound was the first example of a system where Curie temperature is higher than the temperature of superconducting transition - $T_C > T_{sc}$. Coexistence of superconductivity and ferromagnetic order in the region between $1 - 1.5\,\text{GPa}$ was confirmed by the neutron diffraction[48] and NQR [49] studies. Further investigation of this unique pressure induced coexistence brings another interesting information. Huxley et al.[50, 51] observed that maximum of T_{sc} at 1.2 GPa corresponds to the point where the ordered phase exhibits the first order phase transition between two different ferromagnetic phases. This point is called Critical Endpoint (CEP). It can be nicely seen in the phase diagram (Figure 3.1). One of these phases denoted as FM2 is observed at low pressure and exhibits large magnetic moment $M_0 \sim 1.5\,\mu_B$. Second phase FM1 - high pressure phase posses lower magnetic moment $M_0 \sim 1\,\mu_B$. Abrupt change of magnetic moment ($0.5\,\mu_B$) between these two phases showing its first order nature is also observed between the FM1 and PM phase with the change of $0.8\,\mu_B$[52]. The border between PM and FM phase shows to be an example of tricriticality[53]. At certain point corresponding to the pressure of approximately 1.42 GPa and at the temperature of 24 K the nature of this phase transition is changed from the second to the first order. Additionally applied external magnetic field along the magnetic easy axis a leads to the steady decrease of the ordering temperature while its second order nature is conserved. Magnetic order finally disappears at Quantum Critical Endpoint (QCEP) at the pressure of 3.5 GPa and magnetic field of 18 T[53, 54] - see Fig 3.1.

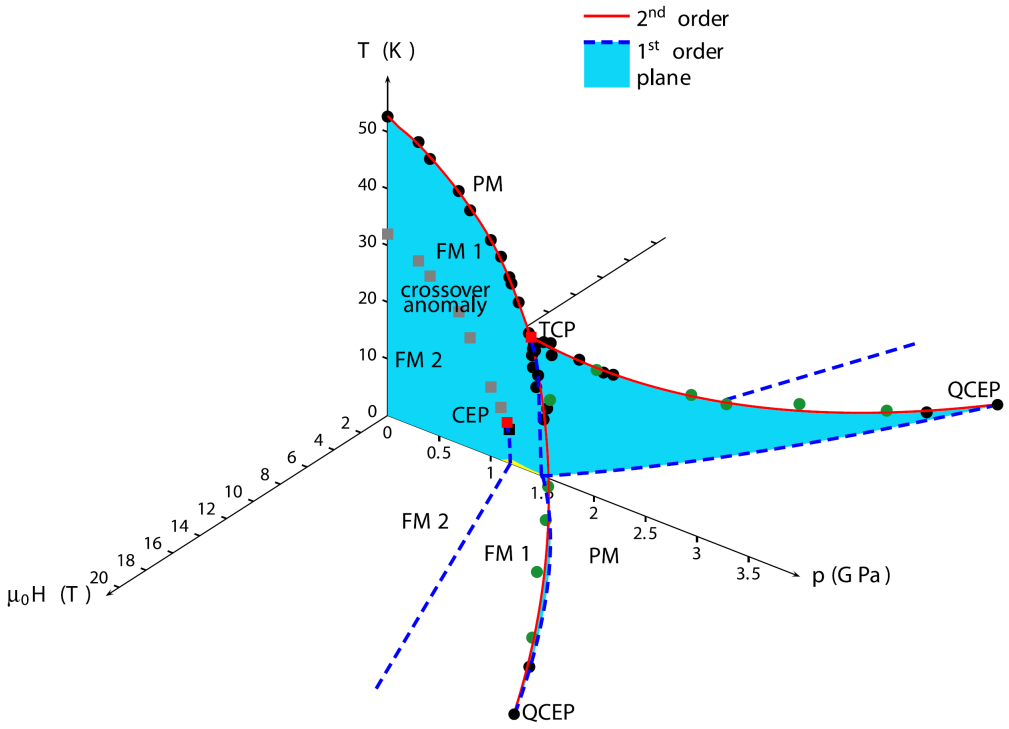

Figure 3.1: Temperature and pressure phase diagram of UGe2. Magnetic field was applied along the easy axis - a. Figure is taken from [55].

3.2 Orthorhombic Members of the UTX Family

As has been already mentioned in Introduction, intermetallic compounds of uranium with some transition metal T and p element X form quite numerous UTX group. Magnetic properties of the whole group are strongly affected by overlapping of spatially extent $5f$ wave functions of uranium[13]. Thanks to that is the shortest distance between two nearest uranium atoms ($d_{\mathrm{U-U}}$) crucial property. Nevertheless hybridization of the $5f$ states with s, p or d states of the T and X ligands should not be neglected.

This work is focused on the members of this family which posses orthorhombic structure. However representatives of hexagonal compounds of the ZrNiAl-type structure should be briefly mentioned as well. Structure of these compounds consists of the alternating layers of $\mathrm{U}-T$ and $T-X$ which are piled along the c axis. One of the most interesting compounds of this subgroup is UCoAl. It has paramagnetic ground state, but it exhibits metamagnetic transition in the external magnetic field of 1 T applied along the c axis at temperatures below 16 K[56, 57, 58]. UCoGa is ferromagnetic below 47 K[59], UNiAl is antiferromagnet below 19 K[13], URhAl is becomes ferromagnetic at 27 K[60] and list of other compounds could follow.

Following part will be devoted to the compounds from UTX family which exhibit orthorhombic structure. Except for few compounds, all of them posses TiNiSi-type structure[13]. It is ordered type of more complex $CeCu_2$-type structure where uranium atoms occupy cerium positions. Schematic view of the structure for general UTX compound is in Figure 3.2.

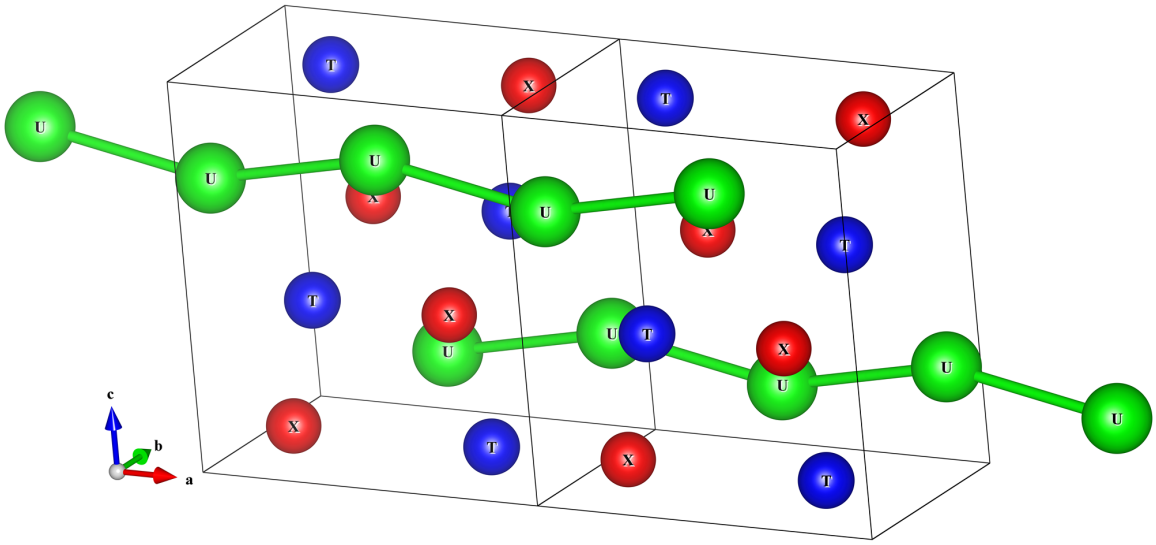

Figure 3.2: View of the TiNiSi-type structure. Uranium atoms are connected to emphasize the zig-zag chain along the a axis. T and X are transition d metal and p element, respectively.

UFeSi and UCoSi are examples of two compounds with paramagnetic ground state[61][14]. While UFeSi was studied also in the form of single crystal with signs of spin fluctuations[62] the UCoSi compound was studied only as a polycrystal. Density functional theory calculations done by Diviš et al. predict instability of the paramagnetic ground state for UFeSi[63] but there is no experimental evidence supporting this prognosis.

UNiSi compound exhibits more complex magnetic properties. Anomalies that are observed in the temperature dependence of the susceptibility, specific heat and electrical resistivity show that UNiSi is magnetically ordered below 87 K[64]. Another transition occurs at 18 K and UNiSi is ferromagnetic below this temperature[64].

URuSi is another example of compound with paramagnetic ground state with signs of spin-fluctuations[14]. Now additional study performed on single crystal is available up to date.

URhSi was studied in the form of single crystal and it is analogous compound to its germanium based equivalent URhGe. Compared to this well known ferromagnetic superconductors URhSi exhibit more or less ordinary strongly uniaxial ferromagnetic properties with Curie temperature of 10.5 K[65] and with no sign of superconductivity down to the 2 K.

UPdSi Proper powder neutron diffraction experiments on UPdSi revealed that ground state of this compound is commensurate antiferromagnet with magnetic moments on uranium aligned along the b axis[66]. Nevertheless incommensurate phase is observed in the temperature region between 27 K and 33 K . High field experiments revealed two metamagnetic transitions at 4 T and 7 T which change the antiferromagnetic order to the high field ferromagnetic phase[67].

UIrSi Although the structure of UIrSi compound was determined from the single crystal X-ray diffraction there are no information available about expected magnetocrystalline anisotropy[68]. Possible Kondo fluctuations behavior[68] is also reported for this compound with paramagnetic ground state.

UPtSi One exception that crystallizes in disordered $CeCu_2$-type structure is UPtSi[14]. It is antiferromagnet with sinusoidally modulated moments along the b axis below 51 K[69].

UFeGe UFeGe has been already mentioned in Introduction as a suitable compound with paramagnetic ground state that can be alloyed with ferromagnets like UCoGe or URhGe and suppress their magnetic order. Despite the fact that UFeGe possess the monoclinic distortion[61] of TiNiSi-type structure, U(Co,Fe)Ge system keeps undistorted type up to the 70% of iron atoms on the cobalt site[70]. Iron substitution on the cobalt site leads to the initial increase of T_C up to the 9 K for 7.5%. Further increase of doping leads to the suppression of ferromagnetic order and to the Quantum Critical Point near 22% of iron, where the temperature dependence of the specific heat and electrical resistivity reveal sign of Non-Fermi liquid behavior[19]. There is no study of the U(Rh,Fe)Ge system available. The value of $d_{U-U} = 3.47$ Å[14] for UFeGe is close to the Hill's limit (see Figure 3.8).

UCoGe As has been mentioned above, UCoGe used to be described as a compound with paramagnetic ground state [14, 15]. Breakthrough came with the report of Huy et al.[11] presenting this compound as a new member of ferromagnetic superconductors family. Its ferromagnetic instability corresponds with the value of $d_{U-U} = 3.48$ that is really close to the Hill's limit. Cobalt atoms are 2.87 Å distant from uranium, thus it can lead to the additional and significant $5f$-$3d$ hybridization. It exhibits Curie temperature of 3 K and quite low magnetic moment of $0.03\,\mu_B$[11] but with robust magnetocrystalline anisotropy with c axis as a magnetic easy axis. Transition to the superconducting state is at $T_{sc} = 0.7$ K[11] at ambient pressure, what is quite deep in the ferromagnetic phase. Coexistence of ferromagnetism and superconductivity is not compatible with standard BCS theory. Therefore some unconventional scenario is needed to describe this coexistence. Spin-triplet Cooper pairing is the most probable type of the superconducting state according to the temperature dependence of upper critical field[71]. Real coexistence of superconductivity and true itinerant ferromagnetism on the microscopic scale was confirmed by μ-SR measurements[72]. Pressure phase diagram constructed on the results of Slooten et al. (Figure 3.3) dramatically differs from the UGe_2 one.

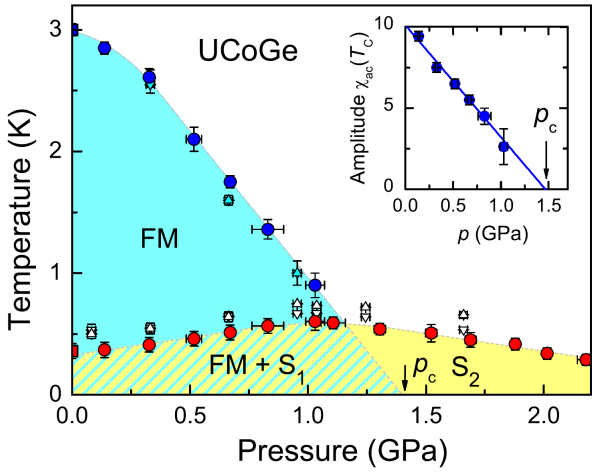

Figure 3.3: Pressure phase diagram of UCoGe showing how superconducting region is spread in to the paramagnetic phase. After Slooten et al.[73].

While this previously mentioned ferromagnetic superconductor has superconducting region fully emerged in the ferromagnetic state, superconducting phase of UCoGe is spread in to the paramagnetic region. There naturally arise question, whether ferromagnetism and superconducting state are tightly bounded together. And if so, why they exhibit different pressure dependence and how is possible, that superconductivity is present even in the absence of ferromagnetic order?

We have already presented that Mineev[45] propose another nature of the superconducting state coexisting with the ferromagnetic order which is spread in to the paramagnetic region. Situation becomes complicated if we chose different tuning parameter then pressure. Substitution of the silicon on the germanium site leads to the simultaneous suppression of ferromagnetism and superconductivity for approximately 12% of silicon[74]. So at least in this case are these two phenomena tightly bounded together. This observation can be an evidence for the triplet superconductivity mediated by ferromagnetic spin fluctuations[12, 35, 44, 42].

If we put aside superconductivity present in the UCoGe and focus our interest on the magnetic properties we can found large discrepancies between experimental data and theoretical calculations. There exist theoretical works trying to elucidate low magnetic moment of the UCoGe. They predict small total magnetic moment on the uranium site ($0.1\,\mu_B$) which is caused by almost complete cancellation of anti-parallel spin and orbital momentum[75, 76, 77]. It is followed by presence of magnetic moment on the cobalt site which can point parallel[76, 77] or anti-parallel[75] to that one on the uranium ion. Anti-parallel alignment of the total magnetic moment of uranium and cobalt was confirmed by polarized neutron diffraction study done by Prokeš et al.[78]. They confirmed that magnetic moment on the uranium is almost completely canceled and that there is also magnetic moment on cobalt pointing in the opposite direction.

It has been already discussed in Motivation of this thesis, that transition metal doping on the cobalt site changes magnetic properties of the system. Small amount of few percents of transition metal dopant supports the ferromagnetic order[17]. Further study of this phenomena based on the alloying with URuGe compound is the main aim of this work, where we expect similar results as for the U(Co,Fe)Ge system with the presence of the Quantum Critical Point[19].

UNiGe is antiferromagnetic compound with strong magnetocrystalline anisotropy. It undergoes two antiferromagnetic transitions, one at 50 K to the incommensurate magnetic phase and second at 42 K to the commensurate ordered phase[79]. If we plot the $d_{U-U} = 3.54$ Å value to the Figure 3.8 together with the value of Néel temperature it fits to the overall trend of suppression of the magnetic order with shortening of the d_{U-U}.

URuGe is the compound with paramagnetic ground state which we decided to use for tuning the magnetic properties of the UCoGe. $d_{U-U} = 3.54$ Å far below the Hill's limit corresponds with the lack of magnetic order. Features in susceptibility for this compound might be sign of possible spin fluctuations[14].

URhGe represents the historically first ferromagnetic superconductor at ambient pressure. It has the distance between two nearest U atoms of 3.50 Å[80]. This is in the interval of Hill's limit pointing on the physical properties on the border of a magnetic order. Quite short distance between U and Rh atoms (2.82 Å) can lead to the further delocalization caused by $5f$-$4d$ hybridization. Curie temperature for this compound is $T_C = 9.5$ K with spontaneous magnetic moment of $0.4\,\mu_B$ and superconductivity appears at ambient pressure at $T_{sc} = 0.26$ K[9]. If we start to applying pressure on this system we will observe very uncommon development of the Curie temperature. T_C is linearly increased at least to the pressure of 13 GPa[81] where it reaches 17 K. Nevertheless this unique dependence is in agreement with Ehrenfest relations based on the heat capacity and thermal expansion measurements. Thermal expansion coefficients measured for all three directions shows positive change below T_C. It leads to the positive pressure dependencies of the ordering temperature for all three directions and for hydrostatic pressure as well. It means that external pressure in the case of URhGe cannot be used for the suppression of the ferromagnetism. Instead negative pressure with estimated value of -8 GPa would be needed[82]. Compared to the ferromagnetism, superconductivity is slowly suppressed and finally disappears at $\sim 2-4$ GPa leading to the retreat from the ferromagnetic instability. These facts are summarized in the pressure phase diagram in Figure 3.4.

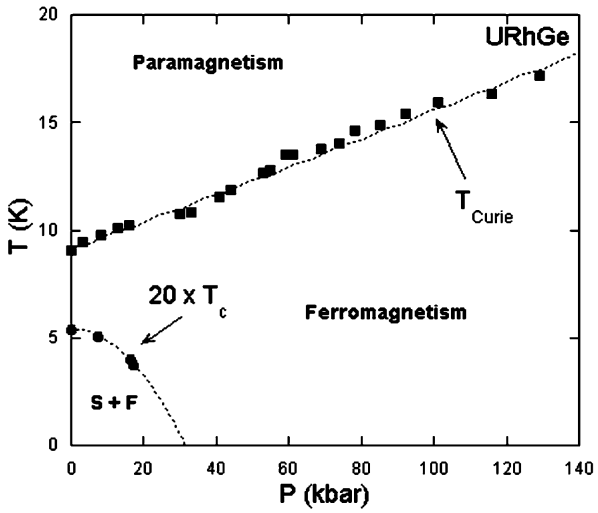

Figure 3.4: Pressure phase diagram of the URhGe compound. Squares are data from AC susceptibility and circles from resistivity measurements. Mind the enlarged value of T_C for clarity[81].

Rather than pressure dependence of T_{sc} the field dependence shows to be more dramatic. Measurement of magnetization curves revealed expected fact, that magnetic easy axis is c. But striking information is higher slope of the $M(H)$ when the external magnetic field is applied along the b axis compared to the c direction. This is followed by metamagnetic field induced spin reorientation at $\sim 12\,\mathrm{T}$ aligned with b direction. Result of this spin transition is unique field-induced re-entrance of superconductivity at $\sim 12\,\mathrm{T}$ as is plotted in Figure3.5. Further increasing of the applied field leads to the creation of a superconducting dome that finally disappears at $\sim 14\,\mathrm{T}$. Maximal temperature of the superconducting transition in this region is even higher ($0.42\,\mathrm{K}$)[55] than in the case of a zero field superconducting phase ($0.26\,\mathrm{K}$). Observation of this behavior depends strongly on the sample quality and also misorientation of the applied field even slightly to the direction of an easy axis c destroys the re-entrant superconducting phase (RSC). On the other hand nonzero projection of an applied field to the a axis leads to the quite stable RSC. RSC phase can be shifted to the higher field if we apply pressure. It is no longer observed above $\sim 1.5\,\mathrm{GPa}$.

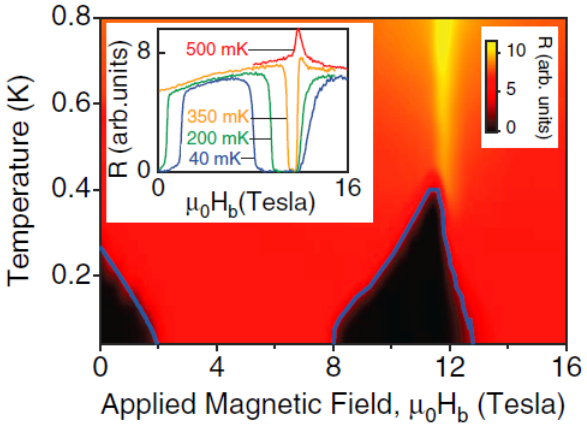

Figure 3.5: Magnetic field phase diagram of URhGe, where field is applied along the b axis. It shows suppression of a low field superconducting phase and unique existence of re-entrant superconducting phase at higher fields. Suppression of ferromagnetism is plotted as well. Inset shows the field dependence of resistivity at [9].

We can compare all three ferromagnetic superconductors at this point. Figure 3.6 shows that for URhGe we are lower in energy then in the case of UGe_2. Plotting the ordering temperature against the shortest distance between two nearest uranium atoms d_{U-U} (See Figure 3.8) also reveals, that URhGe is in vicinity of the region where rather paramagnetic ground state is present. If we plot energy scale of UGe_2 and compare it with URhGe and UCoGe it is obvious that thanks to the high Curie temperature it is far above other ferromagnetic superconductors (See Figure 3.6).

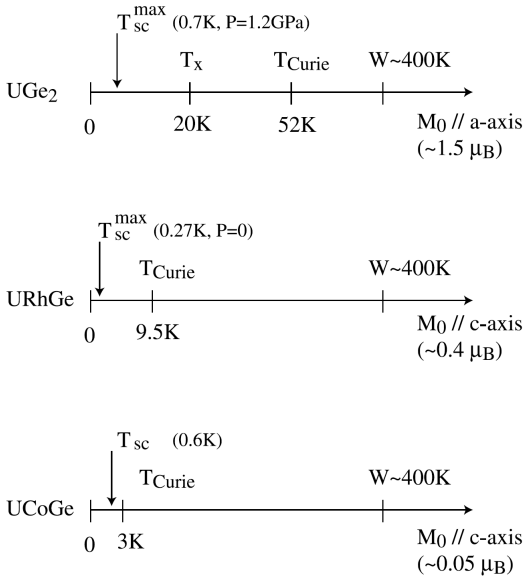

Figure 3.6: Characteristic energy scales for UGe_2, URhGe and UCoGe. After Aoki et al. [83]

UCoGe lies even lower in energy (see Figure 3.6) on the border between paramagnetic and ferromagnetic compounds (See Figure 3.8).

UPdGe exhibits transition to the antiferromagnetic state at 50 K, further transition to the ferromagnetic phase is present at lower temperature of ≈ 30 K[14, 15].

Basic magnetic properties and ground states of above mentioned compounds are schematically summarized in Figure 3.7. This illustration treats UCoGe as a paramagnet. Recent state of art ranks it to the group of compounds with ferromagnetic ground state, together with the URhSi, URhGe and UPdGe.

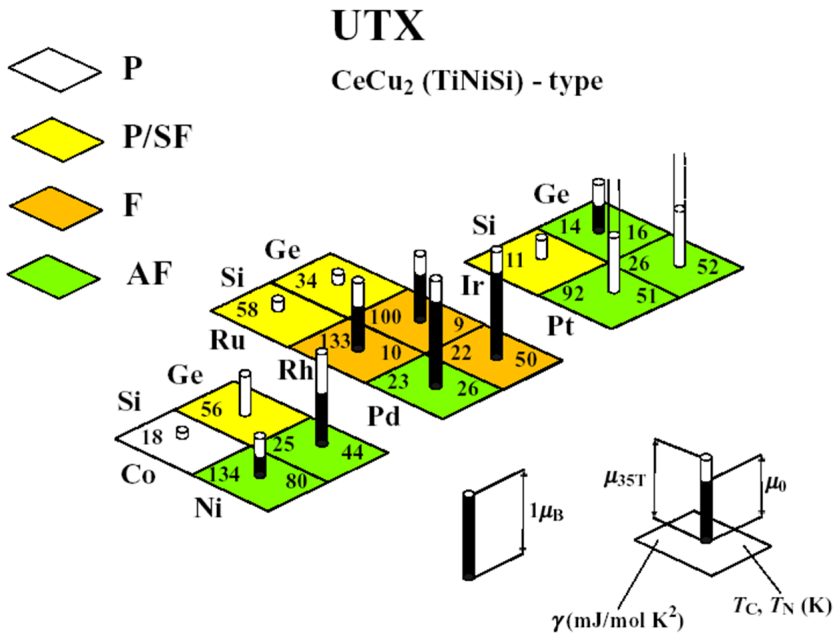

Figure 3.7: Schematic illustration summarizing the properties of the compounds from UTX family that exhibit orthorhombic crystal structure. It shows type of magnetic ground state, appropriate ordering temperature, Sommerfeld gamma coefficient of the specific heat, spontaneous magnetic moment and magnetic moment from high field study in 35 T. After Sechovský et al.[13].

Closer look on the Figure 3.8 reveals that lowering of the $d_{\mathrm{U-U}}$ distance pushes the UTX system out of the ordered state. Higher overlap of the $5f$ wave functions leads to the destabilization of magnetic order. Nevertheless this observation has to be treated only as one possible parameter that affects the magnetic properties of the UTX compound. Hybridization with the ligand orbitals plays important role as well.

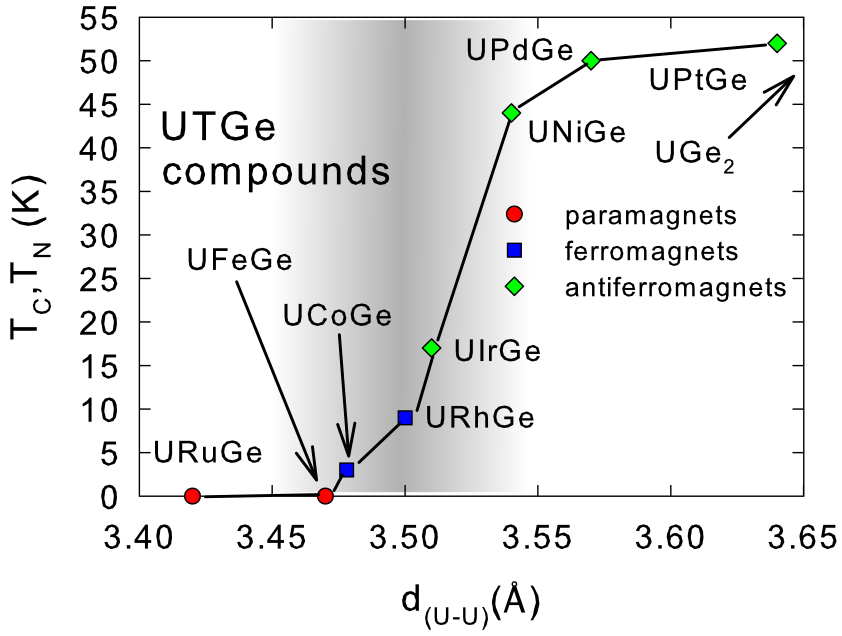

Figure 3.8: Ordering temperature of some of the UTX compounds as a function of the shortest distance between two nearest Uranium atoms d_{U-U}.

4 Experimental Methods

4.1 Sample Preparation

Polycrystalline intermetallic materials are mostly prepared by melting. Final stoichiometric composition is determined by the initial properly weighted amount of the individual elements. Our samples were melted in the mono-arc furnace which volume was properly evacuated down to the order of 10^{-6} mbar. Evacuated space was than filled by the Argon gas of high purity (99.9999 %) as a protective atmosphere and preserves the stability of the arc. Whole procedure was at least three times repeated to ensure sufficient homogeneity of the button shaped melted samples. Purity of the used elements is crucial factor implying the quality of our samples. Thus we used initial elements of high purity. Used natural uranium was additionally purified using the Solid State Electrotransport (SSE) technique[84].

4.1.1 Czochralski Method

Many techniques were developed for crystal growing through the years. One of the often used and most important at least commercially is pulling method named after Jan Czochralski[85]. This method is used for various types of materials like semiconductors (Si, Ge, GaAs), optical crystals (YAG - $Y_3Al_5O_{12}$) or various intermetallic compounds. Input feed material is melted in the crucible either with resistance or radio frequency heater or by electric arc. Growing process itself starts by dipping the seed in vertical way in to the melt. Seed itself can be single crystal with the same composition as the melt. This procedure is usually practiced in industry. In the absence of a precedent crystal it is necessary to use different material as a seed. It is suitable to use some metal with high melting point like wolfram. When the seed is immersed in the melt and consequently pulled up above its surface the feed material sticks to the seed and growing process starts. Seed is than slowly pulled up with the speed of few millimeters per hour with additional rotation of less then five rotations per minute. Change of the temperature of the feed material, rotation of the seed and pulling speed can lead to the change of the diameter of the pulled ingot. When using seed of different material its necessary to decrease the diameter - "necking procedure" - in order to prefer only one crystal grain in the growing crystal. Then the diameter can be increased and we can grow a crystal with the demanded and sufficient diameter. Despite of the fact that main idea of pulling growth is simple, the growing process itself and its success is difficult procedure.

For preparation of our samples was used home-made tri-arc furnace where electric arcs are used for melting the feed material in the water cooled copper crucible. Whole procedure is performed in argon protective atmosphere. As a seed we used a wolfram rod.

4.1.2 Floating Zone Method

Floating zone method is another technique for crystal growing. It is based on the pulling the material vertically through hot zone where it is melted. Feed material in the shape of a rod is placed above the hot zone while the seed and originated crystal is below. Hot zone in the case of optical furnace is achieved by concentrated light of four bulbs which are placed in the focal points of the ellipsoidal mirrors. Common focal point of all four mirrors is centered in the hot zone. Necking process, same as in the case of Czochralski method, is necessary to perform necking procedure for

stabilizing of one grain within the crystal. Both the feed rod and grown crystal are rotated in order to achieve better homogeneity. Whole growing process was performed in the optical furnace - Crystal Systems Corp. FZ-T-4000 - under the protective argon atmosphere.

4.2 Characterization of Structure and Composition

Proper structure characterization and verification of the correct composition is essential condition for further study of physical properties of each material. Structure can be studied with broad spectrum of methods ranging from refinement on the basis of X-ray powder diffraction patterns over neutron diffraction to the simple Laue method confirming single-crystalline state of the sample. With X-ray or neutron diffraction we can also investigated sample composition averaged over some specific volume which interacts with the beam. More localized probe for the composition study is Energy-dispersive X-ray Spectroscopy (EDX) mostly used as a part of the Scanning Electron Microscope (SEM).

4.2.1 X-ray Methods

Production of X-rays which are used as a probe for physical studies can be divided in to the two groups.

First one and most sophisticated production is in synchrotron. In this large facilities circular motion of electrons in the magnetic field leads to the emission of X-rays in narrow beam tangential to the trajectory of the electrons.

However X-ray methods are not dependent on synchrotron sources, so they can be also performed in ordinary laboratories. In this second case X-ray tubes are used.

X-ray diffraction is based on the constructive interference for wavelengths which are similar to the inter-planar spacing in the investigated crystal lattice. This interference (often called reflection) can be observed only when Bragg's law expressed as [86]

$$2d_{hkl}\sin\theta = n\lambda \tag{4.1}$$

is fulfilled. Here n is an integer denoting the order of corresponding reflection. λ is the wavelength of the incident X-rays under the Bragg's angle θ [87] which shows deviation from the planes hkl (described by Miller indices) distanced by the d_{hkl}.

X-ray Powder Diffraction - XRPD Powder diffraction is method where the sample is in the form of small and randomly oriented grains. Thus there is large probability that Eq. 4.1 will be satisfied. Result of XRPD is a diffractogram showing dependence of measured intensity for different diffraction angle 2θ.

We performed our XRPD measurements on Bruker AXS D8 Advance[88]. This diffractometer is equipped by Cu X-ray tube which is monochromatized on the K_α doublet - $K_{\alpha_1} = 1.540600$ Å and $K_{\alpha_2} = 1.544300$ Å. It operates in the so called Bragg-Brentano geometry (see Fig 4.1) where beam impacts the sample which is placed in the center of a fixed diameter (measurement circle). Angle between the sample surface and the direction of impacting beam is the Bragg's angle θ. Diffracted beam is than analyzed by the detector which rotates around the sample keeping the fixed angle

with impacting beam as 2θ. Center of the sample together with the lamp and detector determine the so called focusing circle with varying diameter.

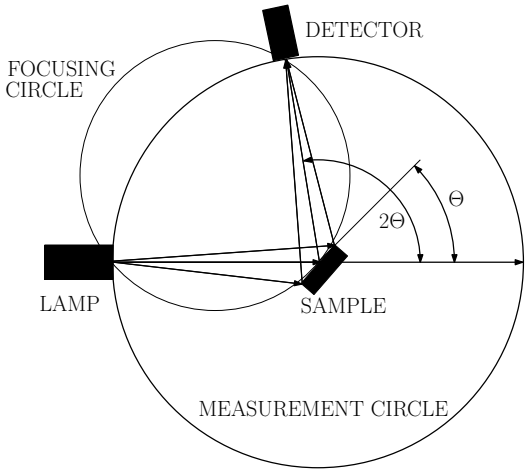

Figure 4.1: Bragg-Brentano geometry for the X-ray powder diffractometer. θ is the Bragg's diffraction angle. Detector is moved with two times higher angular speed to keep the 2θ against the direction of the impacting beam.

Data Treatment We used Rietveld method [89] that uses least square algorithm to refine predicted theoretical model line to match the measured data as best as possible. The peak shape of a powder diffraction reflection is dependent on X-ray spectral distribution, monochromator mosaic distribution and the parameters of sample (shape, crystallinity, etc.). These profiles can be fitted by modified Gaussian or Lorentzian profiles. There is also non-negligible angular dependence of the widths of the shapes of diffraction peaks. It can be described by formula [90] for half-width H_k

$$H_k^2 = U \tan^2 \theta_k + V \tan \theta_k + W \tag{4.2}$$

where U, V and W are half-width parameters. Positions of peaks are dependent on lattice spacing and relative intensities of the peaks in diffractogram are also significant for a particular phase that is obtained in researched sample. That give us opportunity to recognize the phases present in multiphase sample. All we have to do is to create the model defined by parameters with known input values and fit that model to measured data. This procedure was done by FullProf[91]/WinPlotr[92] software.

Laue Method Laue method is commonly used for precise orientation of the single crystals of known or at least expected crystal structure. Compared to the XRPD, where we change the angle θ in Eq. 4.1, in order to find constructive interference for one wavelength λ, Laue method deals with polychromatic radiation to fulfill Bragg's law. For each set of planes hkl with spacing d_{hkl}, when θ is fixed, there is a particular wavelength that satisfies the Bragg's law (Eq. 4.1). So diffracted beams defines the surface of an imaginary cone. This cone intersects with the detecting plate which is perpendicular to the incoming beam direction. It can be arranged either in *transmission* or *back-scattering* geometry. In both cases arrays of dots for each cone forms a conic section on the

detecting plate. Obtained pattern is in fact the stereographic projection of the crystal planes. Final crystal orientation can be deduced from the spots on the detector. Each spot can be indexed with *hkl* indices and thus assigned to the specific set of planes. Shape and character of the spots also reveal quality of the studied crystal.

We used Mikrometa device for crystal orientation by Laue method. It uses Cu lamp and crystal is mounted on the goniometer head allowing rotation along the three independent directions.

4.3 Neutron Diffraction

4.3.1 Introduction

Neutron diffraction is technique which is close to the X-ray diffraction. They both have a lot in common but different nature of scattering properties makes them rather complementary techniques. While the scattering amplitude of the X-rays depends on the atomic number of the scattering center, in the case of neutrons this quantity has no significant dependence and can vary even between two isotopes of the same element. This is described by structure factor $F_N(\mathbf{Q})$. Another important difference is the fact that despite its neutrality neutron has a spin and thus it interacts with the magnetic moments in the matter - this is described by magnetic structure factor $F_M(\mathbf{Q})$. In conclusion neutron diffraction can be used, among other purposes, for determination of the crystal structure and also of the magnetic structure of the studied system. In real experiment we measure intensity given as a quadratic absolute value of the structure factor.

Neutron with one direction of the spin interacts with certain magnetic field in different way then another one with opposite direction of the spin. This observation is used in the so called Polarized Neutron Diffraction (PND).

PND is a very useful tool for investigation of magnetism for example in ferromagnets with low magnetic moment. Otherwise it is very difficult and mostly almost impossible to calculate magnetic structure factor $F_M(\mathbf{Q})$ from the unpolarized neutron experiment intensity due to the high nuclear structure factor $F_N(\mathbf{Q})$. Sensitivity of the measurement is rapidly increased while using polarized neutrons. An external magnetic field is applied on the sample and the incoming beam can be polarized parallel or antiparallel to the direction of this field.

In the case of randomly polarized beam we can analyze energy and momentum of the scattered neutrons. Using the polarized beam we can measure additionally the spin state of scattered neutrons.

We have already mentioned intensity as a observable quantity. It is in fact cross-section of the scattering process and it can be described by Eq. (4.3) [93, 94]

$$I(\mathbf{Q}) = F_N(\mathbf{Q}) F_N^*(\mathbf{Q}) + F_M(\mathbf{Q}) F_M^*(\mathbf{Q}) + \mathbf{P_i}\left(F_M(\mathbf{Q}) F_N^*(\mathbf{Q}) + F_M^*(\mathbf{Q}) F_N(\mathbf{Q})\right) \tag{4.3}$$

where $\mathbf{P_i}$ is a polarization of the incident beam. Eq. (4.3) shows, that for ideally unpolarized incoming beam ($\mathbf{P_i} = 0$) measured intensity depends only on the sum of the squares of structure and magnetic factor. On the other hand, polarized beam ($\mathbf{P_i} \neq 0$) brings two additional terms which contribute to the measured value of $I(\mathbf{Q})$. Ideal polarization is characterized by $|\mathbf{P_i}| = 1$, in this case intensity can be simply written as

$$I(\mathbf{Q})^{\pm} = |F_N(\mathbf{Q}) \pm F_M(\mathbf{Q})|^2 \tag{4.4}$$

Lets assume typical example where the value of magnetic factor is much smaller than structural - e.g. $F_M(\mathbf{Q}) = 0.1F_N(\mathbf{Q})$. In this case unpolarized intensity reaches the value $I_{unp}(\mathbf{Q}) = F_N^2(\mathbf{Q}) + \frac{2}{3}F_M^2(\mathbf{Q}) \approx 1.01F_N^2(\mathbf{Q})$, where $\frac{2}{3}$ is due to the spherical averaging[94].

If we perform the same hypothetical measurement, but this time with polarized beam we come to much better results. At first we measure intensity for one polarization resulting in $I^+ = F_N^2(\mathbf{Q}) + 2 \cdot F_N(\mathbf{Q}) \cdot F_M(\mathbf{Q}) + F_M^2(\mathbf{Q}) = F_N^2(\mathbf{Q}) + 0.2F_N^2(\mathbf{Q}) + 0.01F_N^2(\mathbf{Q}) = 1.21F_N^2(\mathbf{Q})$. Opposite polarization gives the intensity of $I^- = 0.81F_N^2(\mathbf{Q})$. Measured quantity of such experiment is called *flipping ratio* and it is given as

$$R = \frac{I^+}{I^-} = \frac{F_N(\mathbf{Q}) + F_M(\mathbf{Q})}{F_N(\mathbf{Q}) - F_M(\mathbf{Q})} \tag{4.5}$$

Flipping ratio for previous case gives $R = 1.49$ affording much higher contrast between structure and magnetic factor. This advantage is useful for studying systems with small magnetic moments.

4.3.2 Data Refinement

If the structure factor $F_N(\mathbf{Q})$ is precisely measured from some different scattering experiment then together with the measured flipping ratio R stays magnetic structure factor $F_M(\mathbf{Q})$ the only unknown variable in equation (4.5). It can be consequently evaluated for each $\mathbf{Q}$ i.e. for each set of reflections h, k, l. Because the unpaired electrons which stand behind the magnetism of the investigated materials are very extended in real space, magnetic structure factor $F_M(\mathbf{Q})$ is consequently lowered for higher $\mathbf{Q}$ (for higher Bragg indices h, k, l). To suppress this disadvantage it is favorable to use instruments with hot neutrons having short wavelength. These diffractometers allow us to go far in reciprocal space and thus measure also for the high $\mathbf{Q}$ values.

While spatial density of magnetic moment is Fourier transformation of magnetic structure factor (Eq. (4.6) where V is the volume of the unit cell and $\mathbf{r}$ is the vector in real space) it is tempting to simply calculate it.

$$m(\mathbf{r}) = \frac{1}{V}\sum_{\mathbf{Q}} F_M(\mathbf{Q}) \exp(-i\mathbf{Q}\mathbf{r}) \tag{4.6}$$

Serious problem is, that in finite amount of time we are never able to measure the whole reciprocal space so the summation in Eq.(4.6) will always be incomplete. It means that all unmeasured reflections will be equaled to zero and it leads to truncation effects and spin density maps of poor quality. There were developed some direct and indirect methods for better refinement of measured flipping ratios data from polarized neutron diffraction experiments.

One of the direct ones is method based on the Bayesian statistics and maximalization of information entropy - *MaxEnt* [95, 96]. It works with larger group of spin density maps which are consistent with the measured magnetic structure factors. Probability is calculated for each map of this set and the one with the highest one is taken as a best result which has maximal Boltzmann entropy. This method gives much better results then simple Fourier transformation of the magnetic form factors from Eq. (4.6).

Indirect methods of data refinement need some theoretical model that is adjusted to the mea-

sured data. This approach can give much more exact and detailed results then *MaxEnt* method. Nevertheless good knowledge of the studied systems is essential for the data treatment, because even model with unphysical background can be in very good agreement with measured magnetic form factors. One of the mostly used indirect methods, specially on the field of intermetallic compounds, is multipolar expansion technique. Magnetic density is calculated from the spherical harmonics centered on the atoms which are tabulated for each ion[97]. This method allows to distinguish the size and sign of the spin and orbital component of magnetic moment on each atom. It was originally developed for the description of electron densities for the X-ray studies[98]. Magnetic form factor for each ion can be written using spherical harmonics $\langle j_i(\mathbf{r})\rangle$ and parameters W_i in the form

$$f(\mathbf{r}) = W_0 \langle j_0(\mathbf{r})\rangle + W_2 \langle j_2(\mathbf{r})\rangle = \mu_T \left(\langle j_0(\mathbf{r})\rangle + C_2 \langle j_2(\mathbf{r})\rangle\right) \tag{4.7}$$

where μ_T is total magnetic moment. Thus orbital contribution to the magnetic moment is $\mu_L = \mu_T C_2 = W_2$ and spin contribution is $\mu_S = \mu_T - \mu_L = W_0 - W_2$.

4.3.3 Instruments

Precise structure characterization of single crystalline sample was done with neutron diffraction on hot neutron four-circle diffractometer D9 in ILL using Eulerian cradle. Monochromator is formed by copper crystal in transmission geometry using the (220) crystallographic planes produces the wavelength of 0.83860 Å. Neutron beam is detected by two-dimensional multidetector[99].

Polarized neutron diffraction experiment was performed on the D3 diffractometer in ILL equipped by neutron flipper based on adiabatic fast passage[100]. It is equipped by CoFe and Heusler alloy monochromator producing the wavelength of 0.82500 Å. Sample is placed in the external magnetic field up to the 9 T applied along the c-axis. Measurement on both devices can be performed at various temperatures in the range of $3-300$ K. 5 cm diameter single ^{3}He detector is used for recording of the diffracted intensity.

4.4 Physical Property Measurement System (PPMS)

PPMS is multipurpose device manufactured by Quantum Design[101] allowing measurement of a wide range of physical properties. These can be performed in the temperature range of approximately $0.35\,\mathrm{K} - 400\,\mathrm{K}$ and in the external magnetic field up to the 14 T. This magnetic field is produced in the solenoidal superconducting magnet surrounding the cooling annulus (see Fig.(4.2)). Central part of the device is reserved for the sample space that can be evacuated down to the 10^{-5} mbar. Measured sample has to be placed on the specific insert which differs for each type of measurement. Fast and easy exchange of these inserts makes this device a powerful tool for basic study of the physical properties.

4.4.1 Heat Capacity Measurement

Heat capacity is thermodynamic quantity representing amount of the heat per unit mass of system, required to increase its temperature by one degree. heat capacity is additive and can be written as a sum of the different terms

$$C_\mathrm{p} = C_\mathrm{e} + C_\mathrm{ph} + C_\mathrm{mag} + \widetilde{C} \tag{4.8}$$

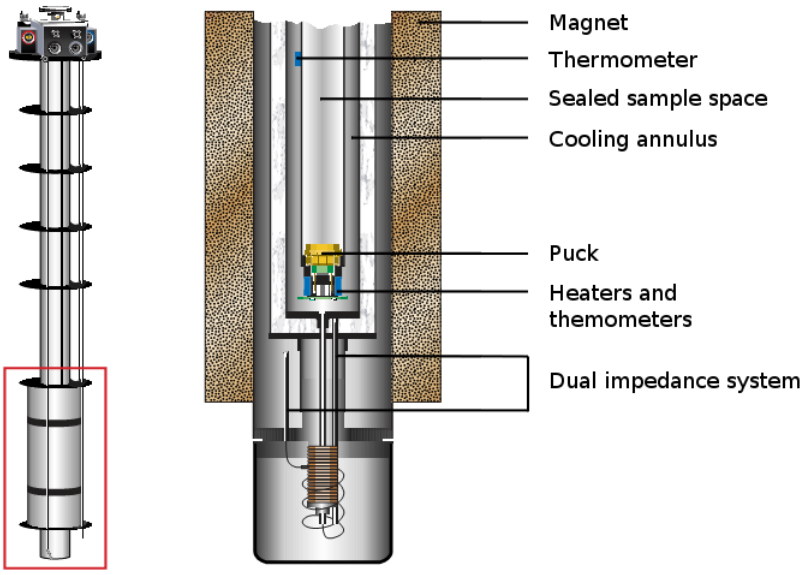

Figure 4.2: PPMS probe and detailed vertical cut of its lower part showing the position of the measuring puck on the bottom of the sample space[101].

where C_{e} represents the electronic contribution (electronic heat capacity). C_{ph} stands for contribution given by vibrations of atoms in the crystal lattice represented by the quasi-particle called phonon. Another term that can be taken into account is C_{mag} representing the magnetic contribution. And finally all other contributions which are not treated separately are summarized in the term $\widetilde{C}$.

Electronic heat capacity is given as a derivative of internal energy with respect to temperature. Change of this internal energy is caused by the increase of temperature from 0 K to T. It is given by equation

$$C_{\mathrm{e}} = \frac{\partial \triangle U}{\partial T} = \frac{\partial}{\partial T}\left(n\left(\varepsilon_{\mathrm{F}}\right) k_{\mathrm{B}}^{2} T^{2}\right) = 2n\left(\varepsilon_{\mathrm{F}}\right) k_{\mathrm{B}}^{2} T = \gamma T \tag{4.9}$$

where $n\left(\varepsilon_{\mathrm{F}}\right)$ represents the density of electronic states at Fermi level ε_{F} and γ is a coefficient that represents linear temperature dependence of the electronic heat capacity.

Phonon contribution of the solid can be treated a set of like linear quantum harmonic oscillators vibrating independently on each other with frequency ω_{E}. This idea of Albert Einstein is resumed in following equation

$$C_{\mathrm{ph,E}} = 3R\left(\frac{\Theta_{\mathrm{E}}}{T}\right)^{2} \frac{\exp\left(\frac{\Theta_{\mathrm{E}}}{T}\right)}{\left(\exp\left(\frac{\Theta_{\mathrm{E}}}{T}\right)-1\right)^{2}} \tag{4.10}$$

here Θ_{E} is the Einstein temperature defined by equation

$$\Theta_{\mathrm{E}} = \frac{\hbar \omega_{\mathrm{E}}}{k_{\mathrm{B}}} \tag{4.11}$$

This so called Einstein model gives realistic zero value for heat capacity at 0 K and also leads

to the classical limit of $3R$ for high temperatures. Nevertheless it is not in agreement with the T^3 dependence which is observed at low temperatures, it gives exponential increase of heat capacity in that region.

Debye came with more complex model involving the distribution of different frequencies ω_{D} corresponding to the so called acoustic waves. It leads to the formula

$$C_{\mathrm{ph,D}} = 9R\left(\frac{T}{\Theta_{\mathrm{D}}}\right)^3 \int_0^{\frac{\Theta_{\mathrm{D}}}{T}} \frac{e^x}{\left(e^x-1\right)^2} x^4 dx \tag{4.12}$$

where $\Theta_{\mathrm{D}} = \frac{\hbar\omega_{\mathrm{D}}}{k_{\mathrm{B}}}$ is the so called Debye temperature and $x = \frac{\hbar\omega}{k_{\mathrm{B}}T}$. This model gives $3R$ for high temperatures as well but primarily varies like T^3 at low temperatures. It gives much better agreement wit the experimental data and in simplified way can be phonon (lattice) contribution at low temperatures (i.e. far below the Debye temperature) described as

$$C_{\mathrm{ph}} = \beta T^3 \tag{4.13}$$

where $\beta = \frac{12k_{\mathrm{B}}\pi^4}{5\Theta_{\mathrm{D}}}$ scales the T^3 dependence.

Heat capacity as a temperature derivative of internal energy can be also used for indicating of transitions which are characterized by anomalies in heat capacity.

Measurements of heat capacity in the PPMS is performed by the so called *two tau method*. It is focused on measuring the time dependence of the temperature on the sample during heating and cooling process. Measured data are fitted with the exponential model and relaxation times resulting from this fit lead to the final heat capacity. Typical mass of measured sample is 20 mg. It has to be placed on the measuring platform of the special puck (Figure 4.3) and also thermally coupled to its surface. It requires precisely polished surface of the sample and for the best contact with the micro-calorimetric platform is used the special *Apiezon* grease. Thermometer and heater for temperature pulses is mounted on the opposite site of the platform. Measurement details are described in the device manual [101]

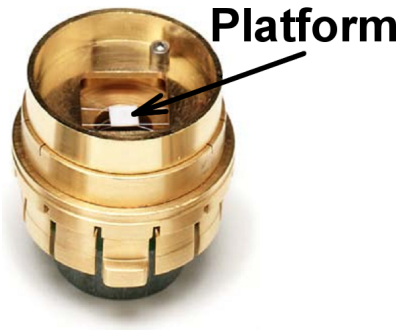

Figure 4.3: Special puck for heat capacity measurements. Sample is placed on the platform in the center[101].

4.4.2 AC Transport Measurement (ACT)

Electrical resistivity of metals is given by collisions of conduction electrons on other particles and quasi-particles. Similarly to the heat capacity can be electrical resistivity treated as an additive quantity.

$$\rho = \rho_0 + \rho_{\mathrm{ph}} + \rho_{\mathrm{mag}} \tag{4.14}$$

where ρ_0 is residual resistivity, ρ_{ph} describes scattering on phonons and ρ_{mag} is spin-disorder term. This empirical observation is called Matthiessen's rule and sets the total electrical resistivity as a sum of different contributions. At higher temperatures is electrical resistivity of metals scaled linearly with temperature due to the electron scattering on phonons. At lower temperatures is observed more general power law dependence. It can be described by Bloch–Grüneisen formula

$$\rho\left(T\right) = \rho_0 + A\left(\frac{T}{\Theta_{\tilde{\mathrm{D}}}}\right)^n \int_0^{\frac{\Theta_{\tilde{\mathrm{D}}}}{T}} \frac{x^n}{\left(\exp\left(x\right)-1\right)\left(1-\exp\left(-x\right)\right)} dx \tag{4.15}$$

where ρ_0 is temperature independent residual resistivity at zero temperature. Exponent n express the scattering mechanism, where for $n = 5$ are electrons scattered on phonons, for $n = 3$ is scattering process of the $s - d$ electrons and finally $n = 2$ describes electron-electron interaction. Value of $\Theta_{\tilde{\mathrm{D}}}$ is typically close to the Debye temperature Θ_{D} obtained from the heat capacity measurements.

The AC transport measurement uses alternating current in the sample as a known variable for the calculation of the electrical resistivity. It is produced in the current source with maximum of 2 A and the precise resolution of 0.02 μA. Frequency for this AC source is between 1 Hz and 1 kHz. Sample itself is contacted for the *four-wires* type of measuring (Fig 4.4). Two outer contacts realize the connection with current source and the inner pair is used to measure voltage on the sample. Voltage is measured by the voltage detector with sensitivity of 1 nV at 1 kHz. For known current and measured voltage we can easily calculate resistance using Ohm's law. If we want to obtain resistivity of the sample it is essential to know the distance between two inner voltage contacts and the cross-section area of the sample perpendicular to the current direction. For this reason the bar shaped sample with typical dimensions of $1 \times 1 \times 6$ mm is preferred. This bar is placed on the special ACT measurement puck (Figure 4.5) and contacts are provided by golden wires and spot welded to the sample.

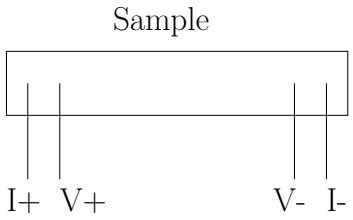

Figure 4.4: Schematics of *four-wire* measurement method. Outer pair of contacts are connected to the AC source and the inner pair is used for the measuring of voltage.

Figure 4.5: Puck for ACT measurements with labeled regions for welding the contacts of *four-wire* method[101].

4.5 Magnetic Property Measurement System (MPMS)

Magnetic property measurement system is a magnetometer of SQUID (Superconducting Quantum Interference Device) construction. It allows us to measure magnetization. The measured sample is fixed to a long rod and dropped down in to the probe. Rod is consequently moved by servomechanism and the sample, in between the detection SQUID coils, produces oscillating AC signal. Magnetization of the sample can be also measured in combination with DC SQUID magnetometry. This measurement technique is very precise and can reach the limit of $\leq 10^{-8}$ emu showing enormous sensitivity. Cryostat allows broad temperature range $\sim 1.9 - 400$ K and also applying of external magnetic field up to 7 T.

4.6 Thermal Expansion Measurements

Thermal expansion measurement is very difficult and it requires really precise and well developed methods. There exist broad range of such techniques where some of them gives immediately absolute values whereas the others also need some reference material to adjust relative results. Some of them are also non-contact like some optical measurements[102] or x-ray[103] and neutron diffraction[104]. On the other hand, the change of the sample dimensions can be in practice measured with contact methods using strain-gauges[105, 106], mechanical dilatometry[107] or direct capacitance method[108].

Our interest was naturally focused on the thermal expansion at temperatures below room temperature and mostly at so called low temperatures. That is the reason why we choose a measurement method which can be performed in the environment of cryostat and also under external magnetic field for further magnetostriction measurement. Method that fits these requirements and is enough sensitive and precise for our purposes is capacitance based measurement[109].

We used miniature capacitance dilatometer of Vienna type suitable for thermal expansion and magnetostriction measurements[109].

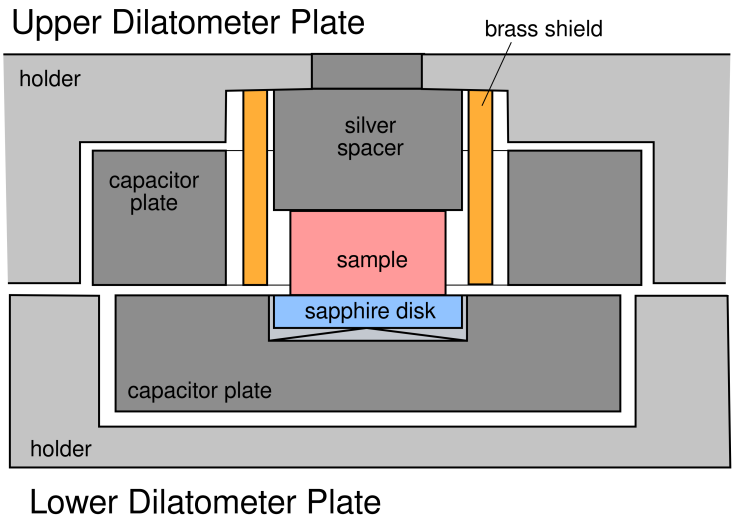

Figure 4.6: Section of the dilatometry cell showing the placement of the sample on the sapphire disk. Change of the sample length varies the distance of the capacitor plates and according to that changes their capacity. After Müller et al. [110]

Construction of the dilatometry cell is based on the tilted plate principle[111, 112] where the sample is placed in between these capacitor plates (See Figure 4.6. Body of the cell is made of silver and two capacitor plates are separated by two brass needle bearings. These bearings and the sample as well are isolated from the silver body of the cell by sapphire washers[113]. It works on the basis of inverting construction[114] where expansion of the sample opens the capacitor and lowers its capacity. This change can be easily measured by capacitance bridge. However this gives only relative information of the length change so calibration measurements are necessary. Finally can be temperature change of capacitance $C\left(T\right)$ measured on the cell used to calculate the thermal expansion of the sample $\frac{\Delta l}{l}$.

From the thermal expansion can be using semiclassical approach[115] obtained information about vibrational or electron-magnetic contribution. Vibrational contribution to the thermal expansion is given by equation

$$\langle x\rangle_{phonon} = 3k_{\mathrm{B}}TA\left(\frac{T}{\Theta_{\mathrm{D}}}\right)^{3}\int_{0}^{\frac{\Theta_D}{T}}\frac{z^{3}}{\exp\left(z-1\right)}\mathrm{d}z \tag{4.16}$$

where Θ_{D} is Debye temperature and A is fitted parameter. Electron-magnetic contribution has the form of

$$\langle x\rangle_{em} = BT^{2} \tag{4.17}$$

where B is a free parameter.

5 Results

5.1 Study of $UCo_{1-x}Ru_xGe$ compounds

5.1.1 Preparation of Polycrystalline Samples

In order to study the development of magnetic state of the UCoGe compound with the additional Ru doping in detail we prepared series of polycrystalline samples. For first rough view on the problematic of the $UCo_{1-x}Ru_xGe$ we prepared samples with $x = 0.1, 0, 2, 0.3, 0.4, 0.5, 0.6, 0.7, 0.8, 0.9$. After further refinement of the data we were able to distinguish interesting regions of doping of the system. Thus we prepared another batch of samples with finer step of 0.01 in the region between $x = 0.2 - 0.35$ and few additional ones for $x = 0.01$ and $x = 0.05$. All these samples were prepared by the same procedure. We weighed proper stoichiometric amount of pure elements for each concentration. For achieving as high quality of our samples as possible we used commercially accessible initial elements of high purity. Namely Co 99.995%, Ge 99.9999 + % and Ru 99.95%. Further we used natural uranium with initial purity of 99.85%. According to the known influence of uranium purity on the quality of the UCoGe compound[84] we used technique of solid state electrotransport (SSE) for additional purification. Thanks to this process we obtained U of much higher purity which should lead to better quality of our samples. Melting process itself was realized in the mono-arc furnace under protective argon atmosphere. Poly crystals were melted on the copper crucible cooled by water. All samples were re-melted at least three times and flipped before each melting process in order to achieve better homogeneity. No sign of evaporation was observed during the melting process. Resulting masses of our button shaped samples were typically 2.5 g. Each sample has been separately wrapped into the tantalum foil with purity of 99.99% and consequently sealed in a quartz tube under the vacuum of 10^{-6} mbar. They have been additionally annealed in resistance furnace at 885 °C for 14 days and then slowly cooled down to the room temperature to avoid internal stresses.

5.1.2 Characterization of the Sample Composition and Structure

We cut part of the each sample by precise wire saw and powderized it in the agate mortar. Hereby prepared samples were used for X-ray powder diffraction (XRPD). It was performed on Bruker AXS D8 Advance diffractometer at room temperature. Thus obtained diffraction patterns were evaluated by standard Rietveld technique [89] using FullProf[91]/WinPlotr[92] software as a refinement of measured data with respect to the already published crystallographic data for UCoGe ($a = 6.852$ Å, $b = 4.208$ Å, $c = 7.226$ Å)[61] and URuGe ($a = 6.678$ Å, $b = 4.359$ Å, $c = 7.539$ Å)[14] compound.

Results of the refinement confirmed composition of our samples without any additional impurities or different phases. As has been already mentioned both UCoGe and URuGe compounds posses orthorhombic TiNiSi structure. Volume of the unit cell of UCoGe is smaller ($V = 208.3$ Å^3) of about 5% than for the URuGe compound ($V = 219.5$ Å^3). Thus the isostructural doping of the Ru on the Co site leads to linear variation of the lattice parameters according to the Vegard's law[116]. While the b and c unit cell parameters are increased with higher concentration of Ru atoms (0.0013 Å/at.% of Ru and 0.0033 Å/at.% of Ru) the a parameter is shortened (−0.0018 Å/at.% of Ru). This change of unit cell parameters results in the volume expansion of the whole unit cell. It follows linear trend with the slope of 0.101 Å^3/at.% of Ru. These dependencies are plotted in

Figure 5.1 and 5.2.

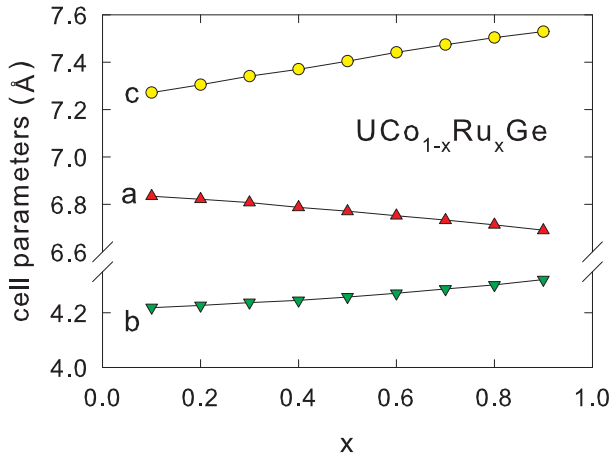

Figure 5.1: Linear evolution of the cell parameters with increased concentration of Ru on the Co site. Lines serve as a guide for the eye.

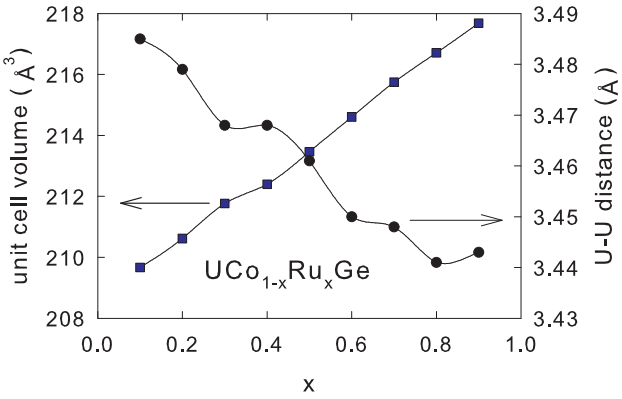

Figure 5.2: Opposite dependence of the volume changed and the change of the distance between two nearest uranium atoms on the Ru concentration.

Expected volume increase is also in agreement with the difference of the covalent radii of Co (126 pm) and Ru (146 pm)[117]. Despite this negative pressure effect we can observe unexpected contraction of the distance between two nearest uranium atoms d_{U-U} (-0.0006 Å/at.% of Ru) leading to the higher overlap between the $5f$ wave functions centered on the uranium ions (see Fig.5.2). It might look like a conflicting evidence with the volume increase, but the zig-zag chain of uranium atoms with two nearest uranium neighbors lies approximately along the a axis and it is the only cell parameter that is contracted with the doping (see Figure 3.2 and 5.3).

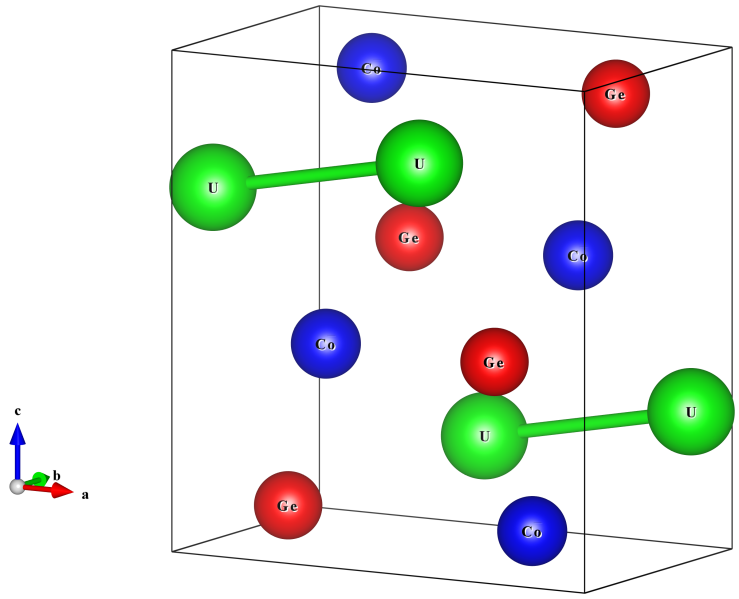

Figure 5.3: Unit cell of the UCoGe with the marked distance between two nearest uranium atoms pointing approximately along the a axis.

Angle of the zig-zag chain for UCoGe compound is approximately 147° while the URuGe exhibits more straight angle of 156°.

5.1.3 Magnetization Measurements

When alloying ferromagnetic UCoGe with the URuGe which has paramagnetic ground state we should expect changes in the magnetic properties within the $UCo_{1-x}Ru_xGe$ system. Thus we measured temperature and field dependence of magnetization for all polycrystalline samples of UCoGe with gradually increasing concentration of Ru. Measurements have been performed in broad temperature range from 1.8 K to the room temperature and up to external magnetic fields of 7 T. Samples for the measurements were cut by precise wire saw in to the roughly cubic shape with dimension of $2 \times 2 \times 2\,\mathrm{mm}^3$. We used bulk material instead of powder, because powderizing brings additional internal stress in to the system[84]. It would in fact destroy the effect of annealing that should release these stresses and could lead to the change of magnetic properties (e.g. shift of the Curie temperature). We supposed that size of the bulk material used for measurement is significantly bigger then grains so we treated it as texture free poly crystal. At first we focused on the development of ordering temperature T_C. The estimation of ordering temperature from the temperature dependence of magnetization is affected by the necessary presence of, even if small, external magnetic field. Thus we decided to estimate the value of T_C for each concentration as a result of the Arrott plot[118] (M^2 over H/M) analysis of isotherms. For each sample we measured magnetization curves up to the 7 T at various temperatures around expected T_C. Thus obtained Arrott plots are strongly nonlinear. This effect can be the first sign of the nearness of a magnetic instability[119]. Then we fitted calculated Arrott plots by the third degree polynomial function (see modeling example in Figure 5.4) in order to find the interception with the M^2 axis of the plot. Extrapolation of the cross-sections with M^2 axis for the different temperatures to the value for $M^2 = 0$ was figured out as an estimation of the final Curie temperature. Example of this

construction is in the inset of Figure 5.4. Thus obtained values for each concentration are plotted in the phase diagram in Figure 5.6. Arrott plots for all other concentrations of ruthenium are presented in Appendix A.

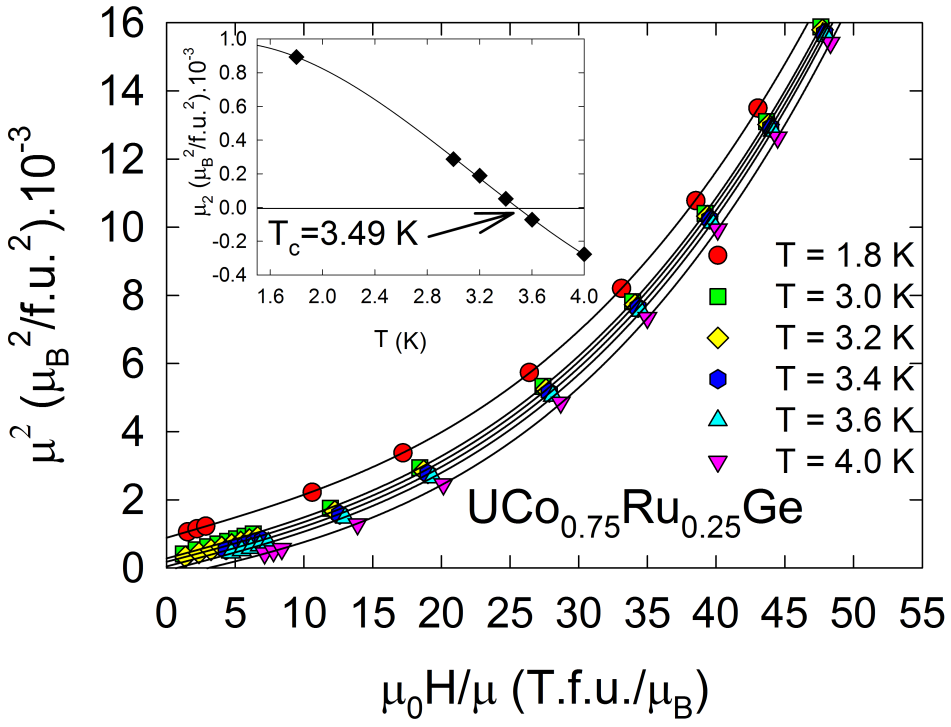

Figure 5.4: Arrott plot constructed for the estimation of the Curie temperature. Example is given for the $UCo_{0.75}Ru_{0.25}Ge$ compound. Solid lines are fitted by the third order polynomial function. Inset shows that the Curie temperature is taken as a value for which the intersection with the μ^2 axis would be zero.

Nevertheless we also performed the derivative of a temperature dependence of magnetization. Minimum of this derivative corresponding to the inflexion point was taken as another estimation of ordering temperatures which are consequently plotted in the phase diagram in Figure 5.6. We have also performed measurement of AC susceptibility where the maximum of the real part χ' roughly corresponds with the inflexion point on the high temperature side of the imaginary part peak. These values are also plotted in the phase diagram in Figure 5.6. AC susceptibility at low temperatures together with the first derivative of a temperature dependence of magnetizations are plotted in Figure 5.5 and thus obtained values are plotted in the phase diagram in Figure 5.6. Blue dashed line in Figure 5.6 represents the temperature limit for magnetization measurements on the samples. Only exception is the sample with $x = 0.29$ which was used for AC susceptibility measurement in lower temperatures using the same device as Prokleška et al.[120] used for the study of UCoGe single crystal.

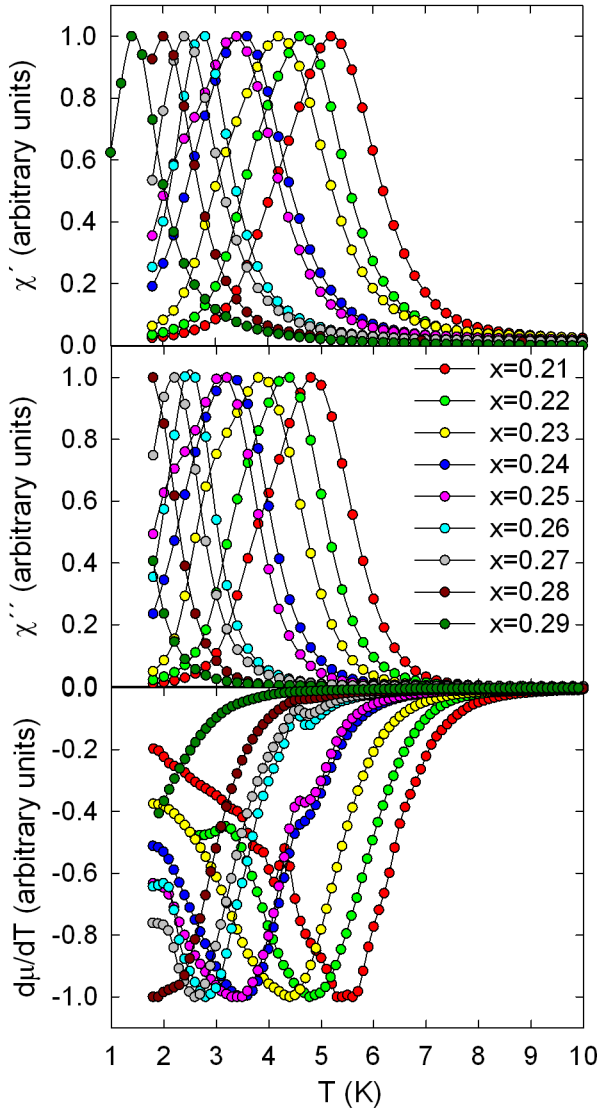

Figure 5.5: Comparison of the AC susceptibility and the first derivative of a temperature dependence of magnetizations for various concentration of ruthenium measured down to the 1.8 K. $\chi^{'}$ component of AC susceptibility for the sample with $x = 0.29$ was also measured in temperature region of $0.5 - 1.8$ K and consequently connected to the data from the measurement above 1.8 K. Details of this measurement are described in the text. All quantities are plotted in arbitrary units.

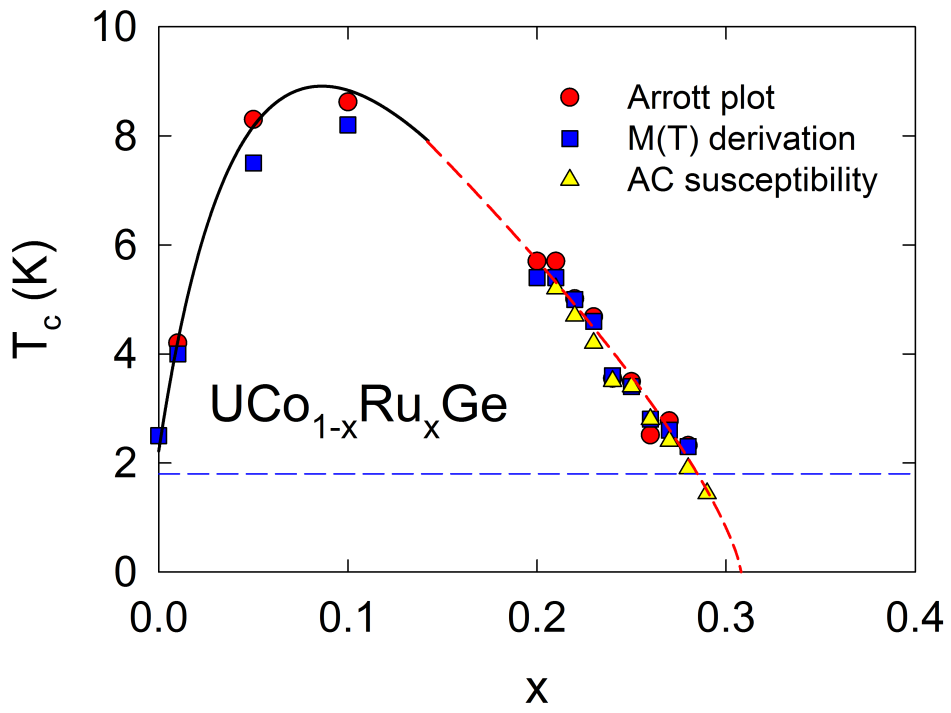

Figure 5.6: Phase diagram based on measurements of polycrystalline samples. T_C is taken as a result of Arrott plot analysis. Other estimations from the derivative of the temperature dependence of magnetization and from the maximum at real part of AC susceptibility is plotted as well. Black solid line is only guide for the eye while the red dashed part is a fit of $T_C \sim (x_{cr} - x)^{3/4}$. Details of this fit are described in the text and also plotted in Figure 5.10. Blue dashed line represents the lowest temperature limit for performed measurements (1.8 K). AC susceptibility measurement for the sample with $x = 0.29$ was performed in lower temperatures, details are described in the text.

Low temperature part of the temperature dependence of magnetization is plotted in Figure 5.7. Results of previous measurements revealed that both the original spontaneous magnetic moment of $0.03\,\mu_B$ and ordering temperature $T_C = 3$ K of parent UCoGe are rapidly increased when we increase the concentration of Ru (see inset of Figure 5.7 and Figure 5.6). This trend changes at concentration $x_{max} \approx 0.1$ where ordering temperature is enhanced up to the $T_{C,max} = 9$ K and magnetic moment reaches its maximum of $0.11\,\mu_B$. This is more than three times higher than in the case of the undoped parent UCoGe compound. Increase of the magnetic moment can be the sign of progress towards the more localized magnetism compared to the itinerant one in the case of UCoGe.

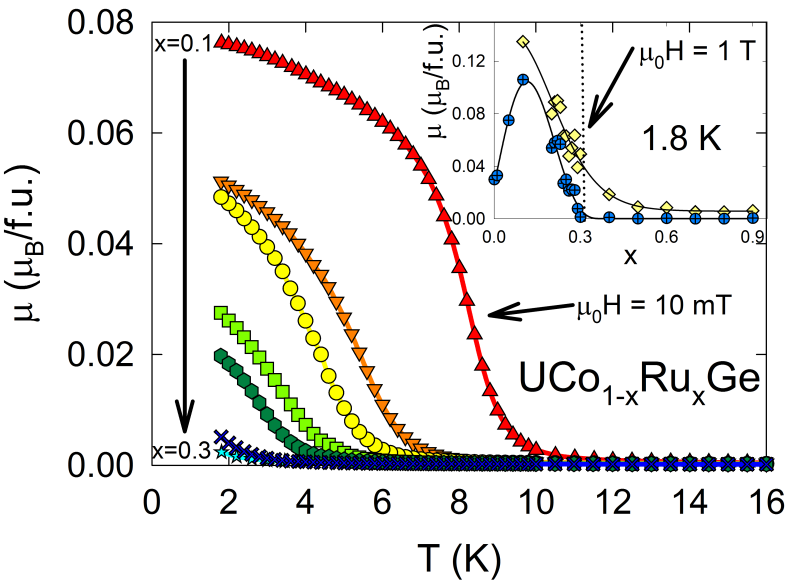

Figure 5.7: Temperature dependence of magnetization for different concentrations of Ru measured in external magnetic field of 10 mT. Vertical arrow on the left side shows decreasing value of magnetic moment with increased x. Inset shows development of spontaneous magnetic moment with increased Ru content (blue circles) from the magnetization curves measured at 1.8 K. Bright yellow diamonds show values of magnetic moment from the same magnetization loop in 1 T. Dotted line in the inset shows the approximate position of the critical concentration.

With increased concentration of ruthenium we observe decrease of the Curie temperature as well as the magnetic moment. Curie temperature goes to zero at some critical concentration of $x_{\mathrm{cr}} \approx 0.3$ where magnetic order disappears. The evolution of the value of the spontaneous magnetic moment (obtained from the magnetization curves measured at 1.85 K in Figure 5.8) is displayed in the inset of Figure 5.7. This inset also shows the value of magnetic moment measured in the higher magnetic field of 1 T. While the spontaneous magnetic moment is suppressed to the zero, there is still some induced moment in the higher field of 1 T. This fact together with the positive slope of Arrott plots[121] brings us to the conclusion, that the transition from ferromagnetic order to the paramagnetic state forced by the Ru substitution is continuous and thus of second order. Development of the spontaneous and saturated magnetic moment is also observable on the change of the shape of magnetization curves (see Figure 5.8). These values are summarized in Table 5.1.

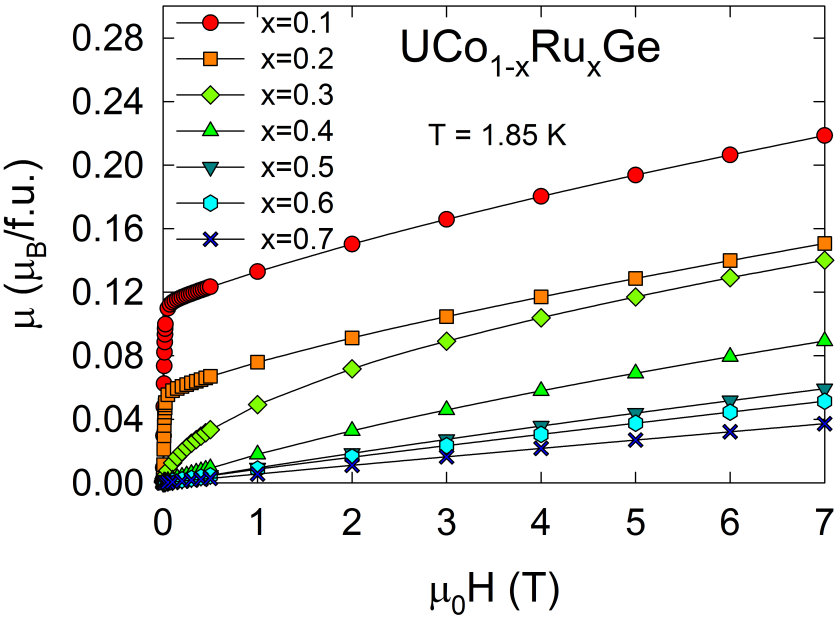

Figure 5.8: Magnetization curves measured at $T = 1.85\,\mathrm{K}$ for different concentrations of ruthenium up to the 7 T. Only some concentrations are plotted for clarity.

x	μ_{spont} (μ_{B})	μ_{sat} (μ_{B})	μ_{eff} (μ_{B})
0.10	0.11	0.22	1.79
0.20	0.054	0.15	1.62
0.21	0.058	0.16	1.59
0.22	0.059	0.17	1.63
0.23	0.057	0.17	1.72
0.24	0.027	0.12	1.51
0.25	0.030	0.14	1.63
0.26	0.021	0.13	1.63
0.27	0.022	0.14	1.63
0.28	0.022	0.16	1.56
0.29	0	0.12	1.57
0.30	0	0.14	1.49
0.40	0	0.09	1.48
0.50	0	0.06	1.39
0.60	0	0.05	1.38
0.70	0	0.04	1.31
0.80	0	0.03	1.45
0.90	0	0.03	1.54

Table 5.1: Values of the spontaneous magnetic moment μ_{spont}, saturated magnetic moment μ_{sat} and effective magnetic moment for different concentration of ruthenium x. Spontaneous magnetic moment μ_{spont} was obtained from magnetization curves in Figure 5.8 measured at 1.85 K. As a saturated magnetic moment μ_{sat} is taken value of the magnetization in the external magnetic field of 7 T measured at 1.85 K. Effective magnetic moment is a result of the modified Curie-Weiss law (Equation (2.18)) fit in the temperature range $120 - 300$ K.

Fitting of the modified Curie-Weiss law (Equation (2.18)) on the susceptibility data measured in external magnetic field of 10 mT on samples with different ruthenium concentration x in the temperature region of $120 - 300$ K revealed steady decrease of the θ_{P} value from -25 K for $x = 0.1$ to the -256 K for $x = 0.9$. This trend is expected because according to the Troć et al.[14] URuGe compound (i.e. in our notation $x = 1$) exhibits high negative $\theta_{\mathrm{P}} = -900$ K[14]. On the other hand we observe almost constant value for the effective magnetic moment per formula unit. Value of the effective moment μ_{eff} is in the range of $1.3 - 1.8\,\mu_{\mathrm{B}}$. These values are significantly lower then the values of the effective moments for the free U^{3+} or U^{4+} ions that are $3.62\,\mu_{\mathrm{B}}$ and $3.58\,\mu_{\mathrm{B}}$ respectively. In the concentration dependence of effective moment is only shallow minimum near the $x = 0.7$ followed by gradual upturn. We can expect, that this upturn can dramatically increase its slope with higher concentration of ruthenium, because URuGe exhibits large effective moment of $3.8\,\mu_{\mathrm{B}}$[14]. Results of our fit are plotted in the Figure 5.9 and effective moments are summarized in the Table 5.1.

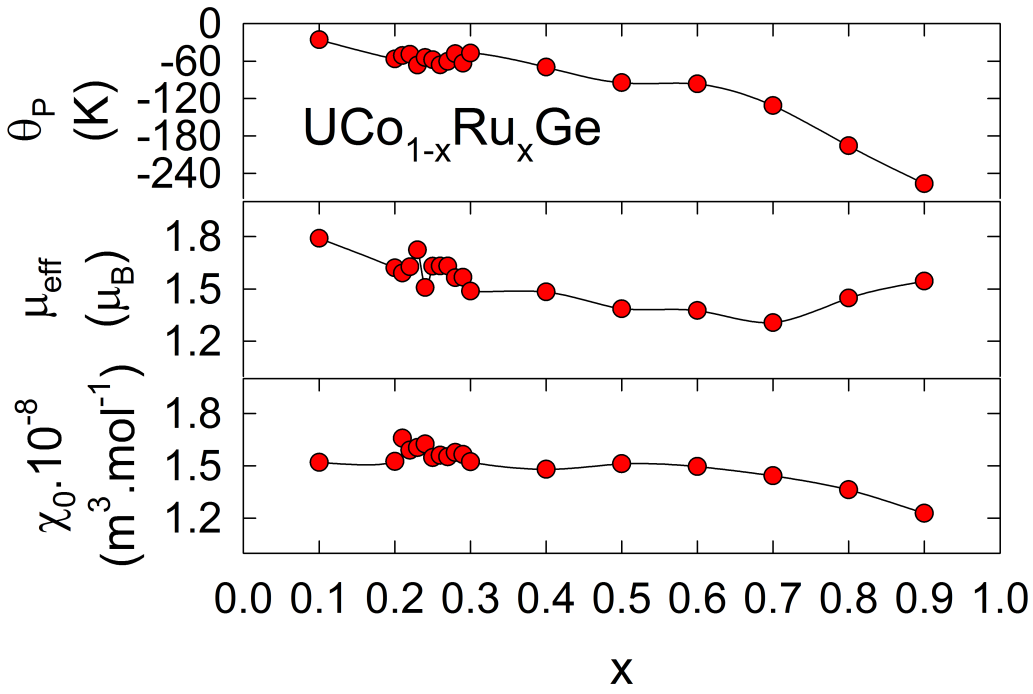

Figure 5.9: Results of the modified Curie-Weiss law (Equation (2.18)) fitting in the temperature range of $120 - 300\,\mathrm{K}$.

According to the prediction for the dependence of Curie temperature (T_C) on the value of control parameter (x) by Millis and Hertz[33, 32] we are able to estimate the value of critical concentration x_cr. Ordering temperature should obey $T_\mathrm{C} \sim (x_\mathrm{cr} - x)^{3/4}$. If we plot Curie temperatures in the region of $x = 0.2 - 0.3$ as a $T_\mathrm{C}^{4/3} \sim x$ plot we should expect linear behavior. This dependence is plotted in Figure 5.10 together with the linear fit giving the estimation for the critical concentration as $x_\mathrm{cr} \approx 0.308(9)$.

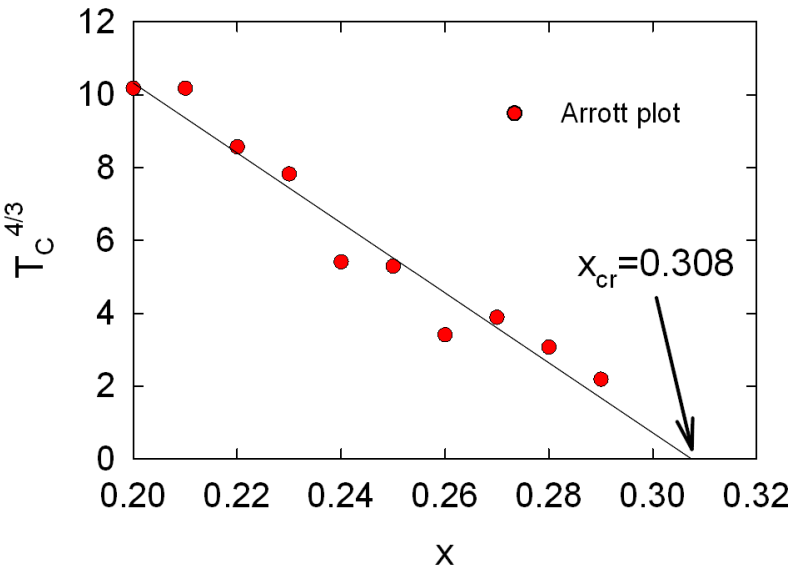

Figure 5.10: Estimation of the critical concentration x_{cr} performed by fitting of the linear dependence of the Curie temperatures T_{C} obtained from the Arrott plots in the $T_{\mathrm{C}}^{4/3} \sim x$ plot.

5.1.4 Heat Capacity Measurements

Samples for the heat capacity measurements were prepared by cutting with precise wire saw in to the shape of flat plates ($2 \times 2 \times 0.1\,\mathrm{mm}^3$) and consequently polished to assure the best thermal contact during the measurement. Usual mass of the samples were 10 mg.

Heat capacity measurements were performed at temperatures in the range of $0.4 - 300\,\mathrm{K}$ and under the applied external field up to the 14 T. Data treatment revealed, that we can observe dramatic change of the temperature dependence of the C/T ratio for different concentrations of ruthenium. Due to the broad transitions for $0.1 < x < 0.3$ we used inflection points of the C/T vs. T curve for an estimation of the Curie temperatures T_{C}. Thus obtained values are plotted in the revised phased diagram in Figure 5.11 showing good agreement with previous results from magnetization measurements.

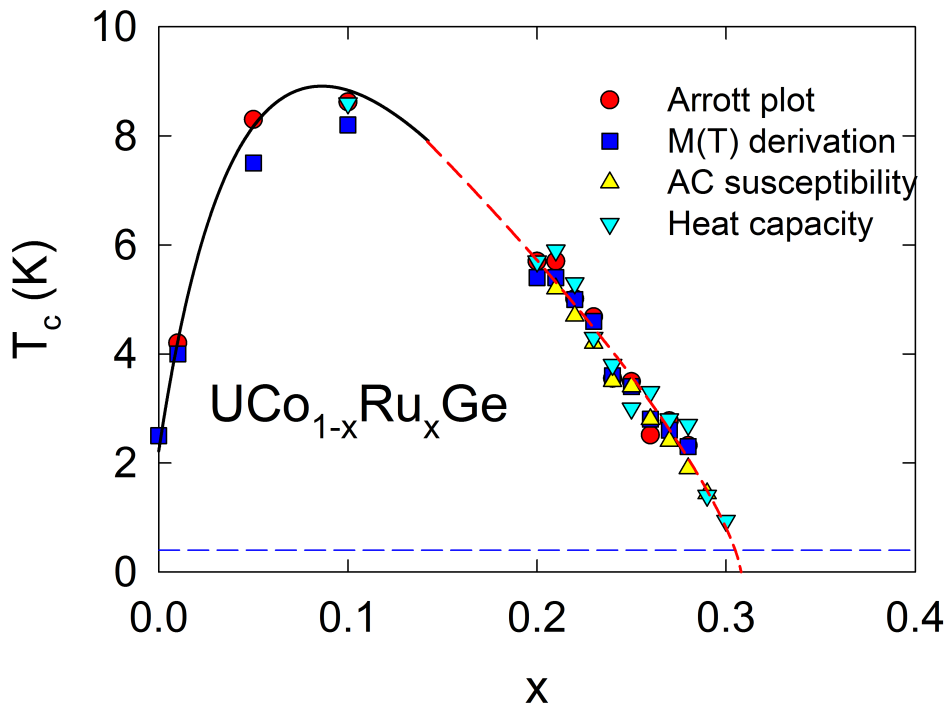

Figure 5.11: Revised phase diagram extending the previous one in Figure 5.6. Additional data points from the specific heat are added. These are inflection points of the temperature dependence. These new set of Curie temperatures well follows the fitted $T_{\mathrm{C}} \sim (x_{\mathrm{cr}} - x)^{3/4}$ dependence marked with the red dashed line. Blue dashed line is a temperature limit for the heat capacity measurements at 0.4 K.

We consequently subtracted phonon contribution resulting from the fit of the lattice specific heat $C_{lat}(T) = \beta T^3$ (giving the values of $\beta \approx (0.52 - 0.56) \cdot 10^{-3}\,\mathrm{J \cdot mol^{-1}K^{-4}}$ i.e. Debye temperature of $151 - 155\,\mathrm{K}$) in the temperature interval between T_{C} and approximately 20 K for each sample with different concentration of ruthenium. For further analysis we plotted magnetic contribution of heat capacity (resulting from the subtraction of the C_{lat}) C_m/T as a function of a logarithm of T (see Figure 5.12).

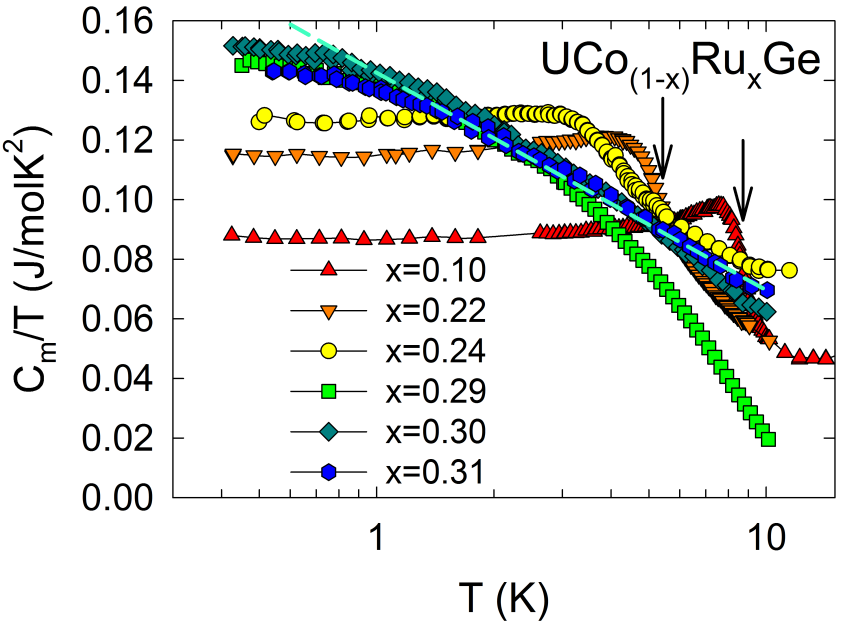

Figure 5.12: Electron specific heat divided by temperature for samples with different ruthenium content in the logarithmic scale. Only few concentrations are plotted for clarity. Black arrows shows the position of Curie temperatures for the $x = 0.10$ and $x = 0.22$ at the inflection point. Dashed cyan line shows linear dependence of the specific heat for $x = 0.31$.

It shows almost linear trend indicating possible presence of NFL behavior for $x \approx 0.31$. As mentioned above Non-Fermi liquid behavior is characterized by logarithmic dependence of specific heat divided by temperature $C_m(T)/T = c \ln(T_0/T)$[33, 32]. This is expected for critical concentration where it might indicate presence of QCP. Anomaly at T_C is smeared down and shifted to lower temperatures with higher concentration of ruthenium. If we calculate magnetic entropy S_{mag} integrated over the temperature range from 0.7 K up to the T_C for each sample we can observe steady decrease of this value from $0.13\,R \ln 2$ for $x = 0.1$ down to the $0.006\,R \ln 2$ at $x = 0.30$ (see Figure 5.13). This also indicates more itinerant nature of the magnetism near QCP ($x \approx 0.31$) then in the region with maximal T_C ($x \approx 0.1$). As the system approaches the QCP we can also observe dramatic increase of Sommerfeld gamma coefficient from former $57\,mJ/mol \cdot K^2$[122] for parent UCoGe up to the $160\,mJ/mol \cdot K^2$ at $x = 0.3$ near x_{cr} (see Figure 5.6). This quantity is consequently lowered for higher concentrations $x > x_{cr}$ (see Figure 5.14). Values of the Sommerfeld gamma coefficients for different concentrations in the range $0 < x < 0.35$ are listed in the Table 5.2.

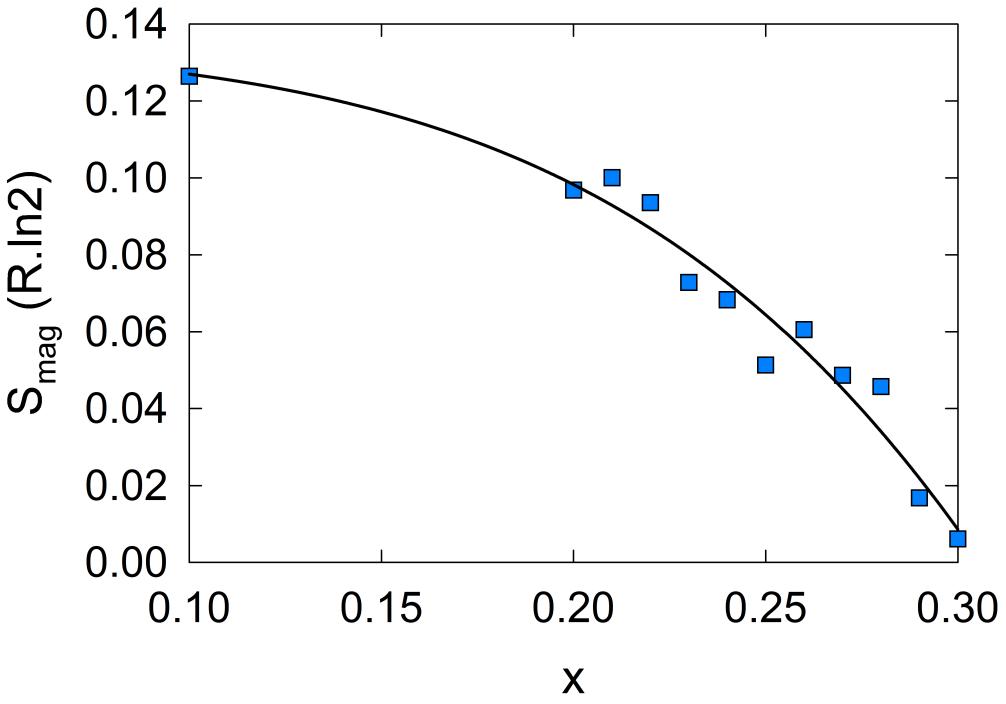

Figure 5.13: The concentration development of the f-electron magnetic entropy integrated from the 0.7 K to the appropriate T_C.

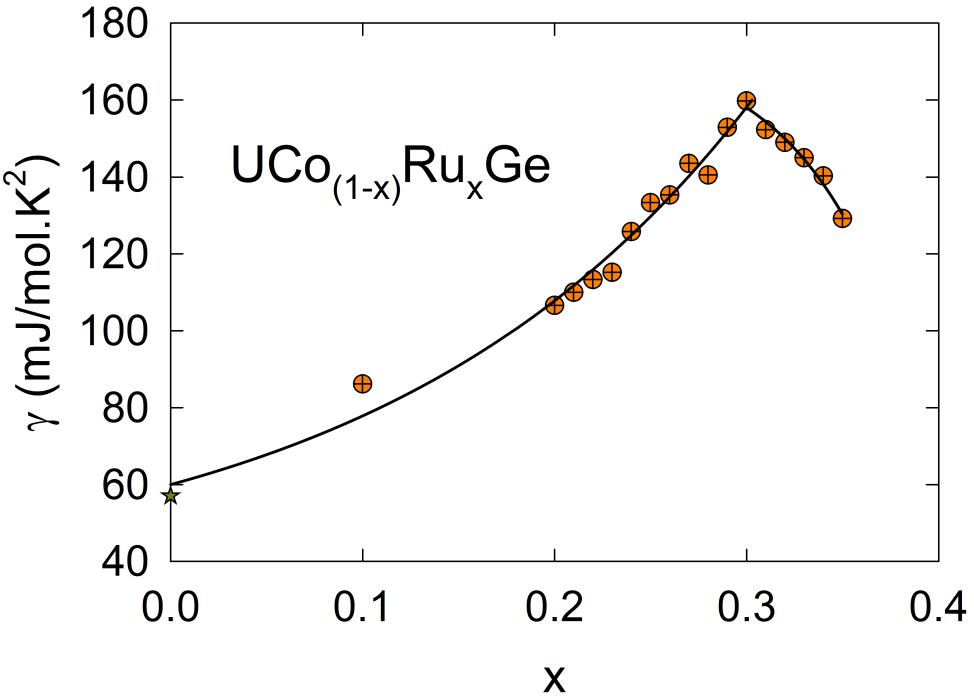

Figure 5.14: Concentration dependence of Sommerfeld gamma coefficient showing maximum value near $x = 30$. Golden star is value for parent UCoGe according to the Gasparini et al.[122]. Black line is only guide for the eye.

x	$\gamma\,(\mathrm{mJ/mol\cdot K^2})$
0	57[122]
0.10	86
0.20	107
0.21	110
0.22	113
0.23	115
0.24	126
0.25	133
0.26	135
0.27	144
0.28	141
0.29	153
0.30	160
0.31	152
0.32	149
0.33	145
0.34	140
0.35	129

Table 5.2: List of the corresponding Sommerfeld gamma coefficients for the samples with different ruthenium concentration x.

5.1.5 Resistivity Measurements

Samples for resistivity measurements were cut by precise wire saw in to the form of small blocks ($1 \times 1 \times 5\,\mathrm{mm}^3$). Contacts were made of a gold wire (with diameter of $25\,\mu$m) spot-welded on the sample surface. Resistivity of the whole series of $UCo_{1-x}Ru_xGe$ for $x \leq 0.31$ was measured in broad temperature range from 0.4 K up to the 300 K. High temperature resistivity for all measured polycrystalline samples shows initial increase up to the maximum at T_0. Same effect is also observed in the resistivity data measured on the single crystal of parent compound UCoGe[84]. It is pronounced only on the temperature dependence of resistivity measured along the c axis[84]. This anomaly is not observed along the magnetic hard axes a and b[84] which shows ordinary metallic behavior. This resistivity increase effect is connected with spin fluctuations when $T^{5/3}$ spin fluctuation model was applicable at temperatures below knee[84]. Our data measured on polycrystalline samples reveal general increasing dependency of the temperature T_0 on the ruthenium content x but with no sign of regular trend. These are resulting from the strong anisotropy of the system. Even small sign of preferred orientation of grains in the poly crystal or its texture can dramatically change the temperature dependence of resistivity of the sample. Some samples exhibited well pronounced maximum at T_0 while the others showed rather broad plateau or even almost metallic features. The first case shows preferred orientation along the magnetic easy axis c while the broad plateau can be sign of orientation along one of the magnetic hard axes (a or b). Nevertheless the

overall increase of T_0 corresponds to the fact that for URuGe compound the knee is not present in the data measured on the polycrystalline samples up to the 300 K[123]. Resulting temperature dependencies of resistivity ratios for selected polycrystalline samples are plotted in Figure 5.15.

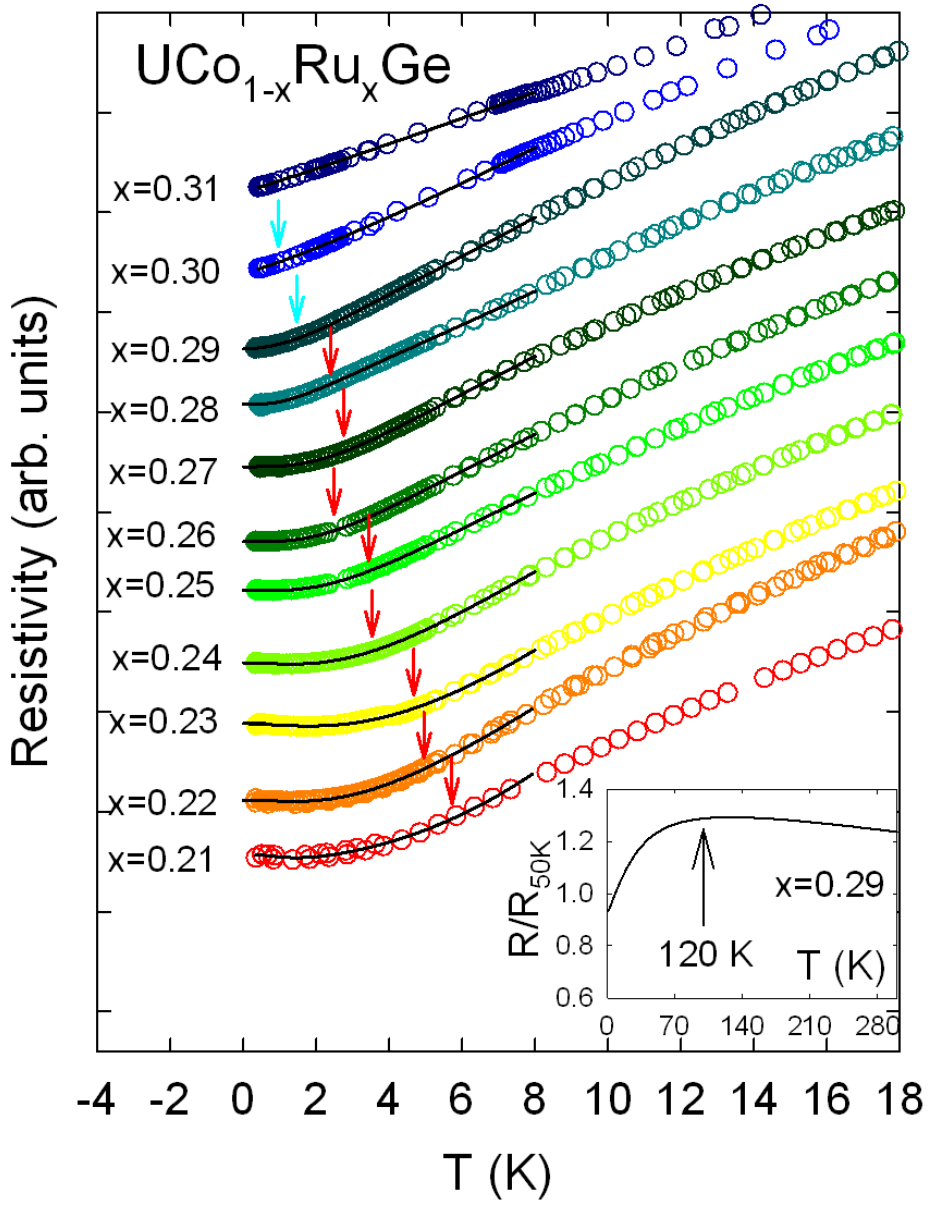

Figure 5.15: Temperature dependence of resistivity for selected polycrystalline samples with gradual ruthenium content. Red arrows denote the Curie temperatures obtained from the Arrott plots, cyan arrows point on the Curie temperatures obtained from the heat capacity data. Solid lines are fits with the $\rho = \rho_0 + AT^n$. All curves are arbitrary horizontally shifted for better clarity. Inset shows typical development of resistivity (for $x = 0.29$) in broad temperature range up to the room temperature. It shows maximum in the resistivity (T_0), in this case approximately at 120 K.

All curves are arbitrary vertically shifted for better clarity. Anomalies connected with the transitions from ferromagnetic to the paramagnetic state are not so clearly visible on the polycrystalline

data. Arrows in Figure 5.15 shows Curie temperatures resulting from analysis of Arrott plots and for the samples with lower T_C are used values from specific heat data. It is obvious, that increased ruthenium content dramatically changes curvature of the low temperature part of resistivity in the $UCo_{1-x}Ru_xGe$ system. While resistivity of the less doped samples shows almost quadratic temperature dependence those with higher ruthenium content scales rather linearly with the temperature. Linear temperature dependence of resistivity is according to the Millis and Hertz[33, 32] sign of Non-Fermi liquid behavior in the three dimensional ferromagnet (as has been mentioned above Moriya[34] and Lonzarich[35] predict $\rho \sim T^{5/3}$). Results of the $\rho = \rho_0 + AT^n$ fits are plotted in the Figure 5.16 and obtained curves are also viewed in the Figure 5.15. It is obvious that for $x = 0.31$ we observe almost linear temperature dependence of resistivity ($n = 1.1$). This is another sign of Non-Fermi liquid behavior near critical concentration x_{cr}.

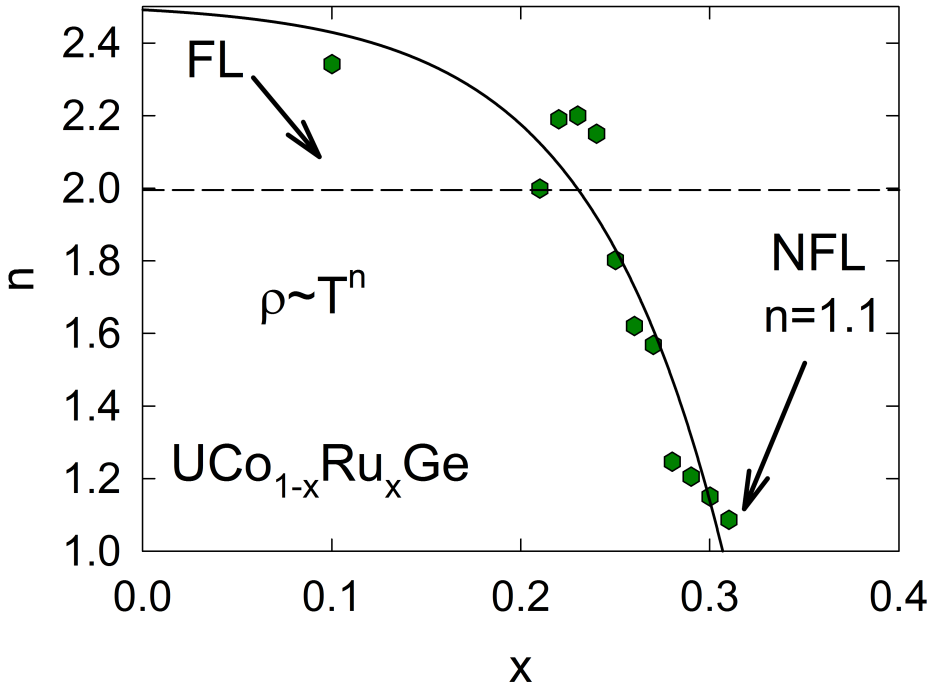

Figure 5.16: Concentration dependence of the n exponent for the low temperature dependence of resistivity according to the equation $\rho = \rho_0 + AT^n$. Dashed line shows the expected value for ordinary Fermi liquid behavior.

5.2 $UCo_{0.88}Ru_{0.12}Ge$ Single Crystal Study

Increase of the magnetic moment (see Figure 5.7) and simultaneous development of the ordering temperature with increasing ruthenium content found in poly crystals study reveal some change of the magnetic properties in the system in microscopic range. Such effects cannot be understand on the basis of standard macroscopic measurements performed in addition on polycrystals. In order to reveal background of this process and to be able to study also anisotropy properties we step to the preparation of the single crystal near the concentration x_{max} where T_C and spontaneous magnetic moment reach their maximum.

5.2.1 Single Crystal Growth and Characterization

Single crystal was prepared by the floating zone method in the optical furnace. Rod of the feed material was used as an initial material for growth. For this purpose is necessary to prepare series of four polycrystalline buttons at first. They were melted in the mono-arc furnace from the initial, properly weighted, amount of the elements with the same purity as in the case of former polycrystalline samples. Special water cooled copper crucible with a channel is used for the preparation of the rod. Polycrystalline buttons are placed in to this channel and consequently melted together under protective argon atmosphere. Typical length of such a rod is about 10 cm and mass is approximately 30 g. Then a part of the rod of about 2 cm is cut by precise diamond saw and serves as a seed for the growing process. This seed is fixed to the corundum holder by tantalum wire and the feed rod is hanged above. Both the seed and feed rod are rotating in opposite directions during the growth. Speed of the rotation was 40 rotations per minute before necking then it was stopped when forming the neck and during the consequent crystal growth. Speed of the vertical movement through the hot zone varied from 6 mm per hour to the 12 mm per hour.

Quality of the as grown crystal was verified by the Laue method. It proved its single crystalline character and high quality. We were also able to orient the single crystal with respect to the crystallographic directions of the unit cell with this method. Body of the crystal was consequently shaped by precise wire saw in to the proper form of the samples for further measurements.

XRPD analysis revealed composition of the crystal as $UCo_{0.88}Ru_{0.12}Ge$.

5.2.2 Magnetization Measurements

Sample for the magnetization measurements was small cube with dimensions of $2 \times 2 \times 2\,\mathrm{mm}^3$ where its faces were perpendicular to the crystallographic directions ($\langle 100 \rangle$ - a, $\langle 010 \rangle$ - b and $\langle 001 \rangle$ - c). The sample was fixed by GE glue in appropriate orientation in the plastic straw for each measurement.

Measurements of the magnetization curves at various temperatures in the applied magnetic field up to the 7 T revealed expected and very strong magneto-crystalline anisotropy. Magnetization loops measured with external field along all three crystallographic directions at the temperature of 1.8 K are plotted in Figure 5.17.

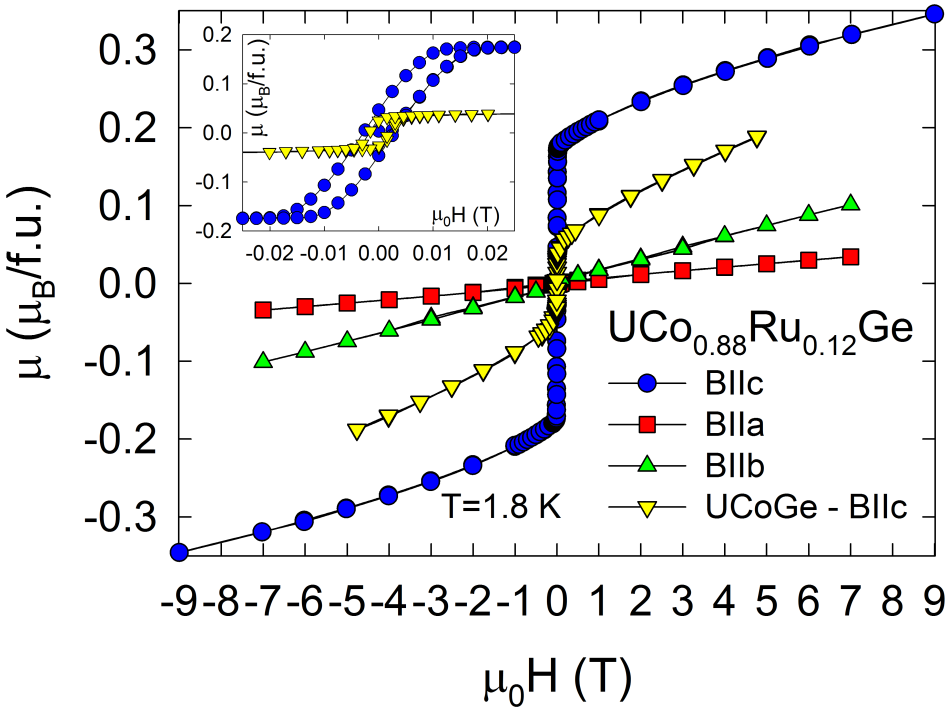

Figure 5.17: Magnetization loops for single crystalline sample with different orientation of an applied external magnetic field. Magnetization loop for the parent compound UCoGe with field aligned with the c axis is plotted for comparison[84]. Inset of the figure shows low field region where small hysteresis is apparent.

Rapid increase of the magnetization with applied external magnetic field along the c axis reveals that this axis is magnetic easy axis. It exhibits spontaneous magnetic moment of $0.21\,\mu_B$ in 1 T. This value is about 85 % higher then for the parent compound [84].

It follows our results from the polycrystalline samples study. Observed small hysteresis is increased in the doped system from initial ~ 4 mT for UCoGe up to the ~ 5.8 mT for $UCo_{0.88}Ru_{0.12}Ge$. As expected magnetization changes slowly when external field is applied along the a and b axis. These two directions corresponds to the magnetically hard axis and behave paramagnetic like. In the region above 1 T increases magnetization for the c axis approximately linearly with the slope of $0.02\,\mu_B \cdot T^{-1}$ with no sign of saturation. Linear increase for a and b direction has the rate of $0.005\,\mu_B \cdot T^{-1}$ and $0.01\,\mu_B \cdot T^{-1}$ respectively. Temperature dependence of magnetization measured along the c and b axis is plotted in Figure 5.18.

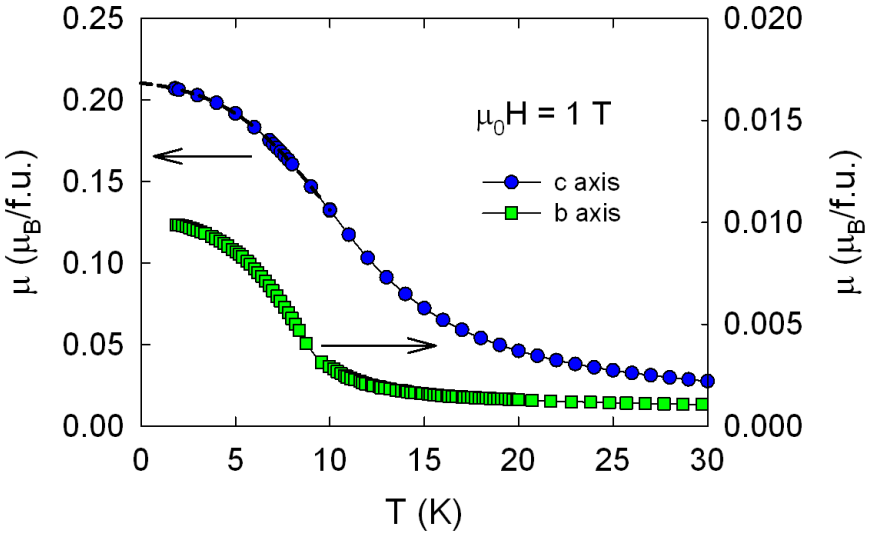

Figure 5.18: Temperature dependence of magnetization measured along c and b axis of the single crystal $UCo_{0.88}Ru_{0.12}Ge$. Values were obtained in external magnetic field of 1 T. Mind the different scale for each axis. Dashed line denotes the extrapolation to the zero temperature.

5.2.3 Polarized Neutron Diffraction

Polarized neutron diffraction is a powerful technique which can give us valuable information about the distribution of spin density within the unit cell. We used this tool to investigate the microscopic mechanism that stands behind the anomalous increase of magnetic moment and T_C up to the concentration x_{max} in comparison to parent UCoGe.

We used for this measurement the same sample as for the magnetization measurements. As has been mentioned before, it is essential to have perfect information about the crystal structure of the investigated material for construction of the spin density map. Thus we performed unpolarized neutron experiment on the D9 device in ILL at first.

We have measured set of more than 350 nonequivalent reflections at the temperature of 11 K (i.e. above T_C). Corresponding structure model resulting from the structure of parent compound[61] was refined by standard Rietveld technique [89] using FullProf[91]/WinPlotr[92] software. Anisotropic extinction corrections for single crystals were used during the refinement. Comparison of the squares of measured ($|F_N|^2_{obs}$) and calculated ($|F_N|^2_{calc}$) structure factors is plotted in Figure 5.19 showing very good agreement of measured and calculated values.

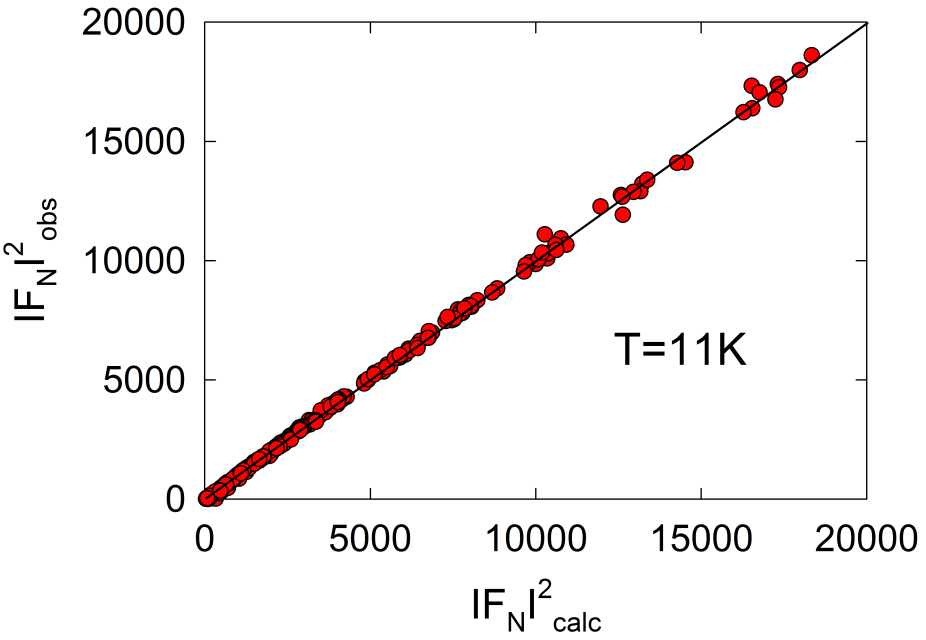

Figure 5.19: Comparison of measured ($|F_{\mathrm{N}}|^2_{\mathrm{obs}}$) and calculated ($|F_{\mathrm{N}}|^2_{\mathrm{calc}}$) structure factors according to the model used for Rietveld refinement. Data were taken on D9 diffractometer in ILL at 11 K.

Refinement adjusted the content of ruthenium in our sample. According to the neutron diffraction it posses $13.5 \pm 0.8\,\%$ of ruthenium on the cobalt position. Obtained cell parameters together with the fraction coordinates are listed in the Table 5.3.

	$a\,(\text{Å})$	$b\,(\text{Å})$	$c\,(\text{Å})$	$V\left(\text{Å}^3\right)$
	6.7998	4.2104	7.2744	208.2652
Space group	Pnma			
	x	y	z	occupancy
U	0.01031(7)	0.25000	0.70547(8)	1.000
Co	0.28375(23)	0.25000	0.41618(24)	0.866(8)
Ru	0.28375(23)	0.25000	0.41618(24)	0.134(8)
Ge	0.19239(8)	0.25000	0.08648(9)	1.000

Table 5.3: Unit cell parameters as a result of a single crystal refinement for $\mathrm{UCo_{0.88}Ru_{0.12}Ge}$.

We have also tried to make a model where ruthenium atoms are placed on the germanium sites, but it was not compatible with measured data.

Consequently followed the polarized neutron diffraction experiment on D3 diffractometer in ILL. We decided to measure in two magnetic fields applied along the c axis (1 T a 9 T) in both cases below ordering temperature (i.e. at 1.65 K). Flipping ratios were collected for the set of Bragg reflections up to the $\frac{\sin\theta}{\lambda} = 0.9\,\text{Å}$.

Magnetic structure factors were evaluated using equation (4.5) with structure factors resulting

from the unpolarized diffraction and flipping ratios from polarized neutron diffraction. Values for both external magnetic field 1 T and 9 T are plotted in Figure 5.20.

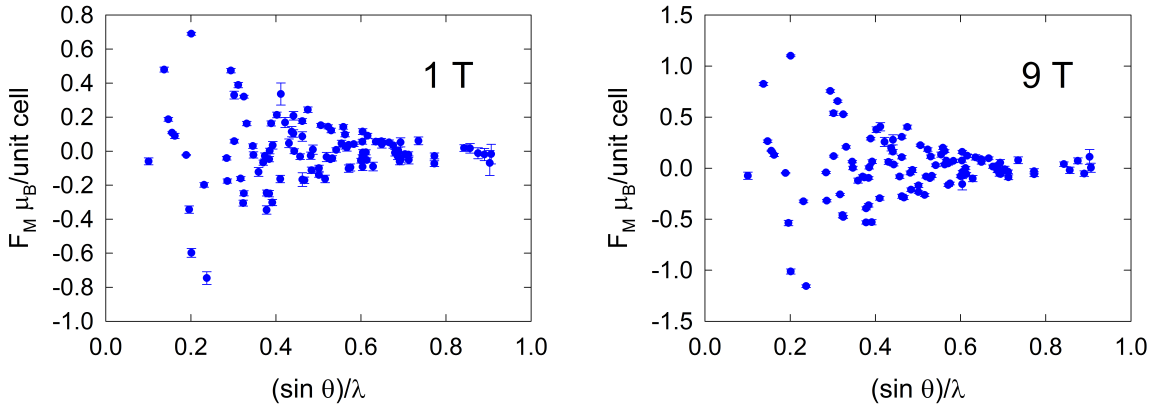

Figure 5.20: Magnetic structure factors calculated from the flipping ratio measurements. Left panel shows results for smaller external field of 1 T, right panel is for 9 T measurements.

Spatial density of the magnetic moment can be in first rough approximation obtain using the inverse Fourier transformation (Equation (4.6)) of the magnetic structure factors. Side effects and disadvantages of this procedure were mentioned above. Nevertheless it is useful tool for the first and rough estimation of the magnetic density within the unit cell. Appropriate calculation was performed using GFourier software[124]. Magnetization density maps are plotted as a projection of one half of the unit cell to the $a - b$ plane in Figure (5.21). It shows that spin density within the unit cell is positive, nevertheless some regions of density are artificial artefacts caused by finite number of measured reflections used as an input to the Fourier transformation.

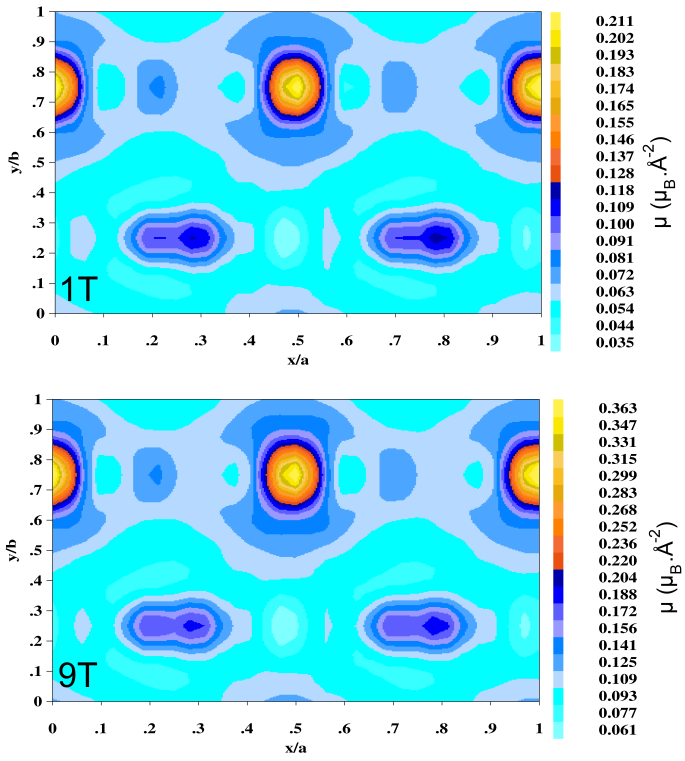

Figure 5.21: Magnetization densities obtained as an inverse Fourier transformation of the magnetic structure factors calculated with GFourier software. Upper panel shows data from 1 T measurement and lower panel from 9 T .

More sophisticated approach is necessary to be used for obtaining results which are in better agreement with real spin density in the unit cell. We used maximum entropy method in MAXENT software as a part of CCSL[125] as a next method. Before computation of distribution of magnetic moment whole unit cell was divided in to the $50 \times 50 \times 50 = 125000$ smaller cells. Algorithm then calculates set of all possible spin density maps according to the measured flipping ratios and consequently choose the one which has the highest informational entropy corresponding to the highest probability. Results of this method are graphically plotted in Figure 5.22. Projection to the $a - b$ plane is again presented as the most illustrative interpretation of the magnetic moments on the atomic positions. Projection to the $a - c$ shows zig-zag chain distribution of uranium atoms along the a axis. In this case we also show comparison with the results from unpolarized experiment showing positions of the atoms.

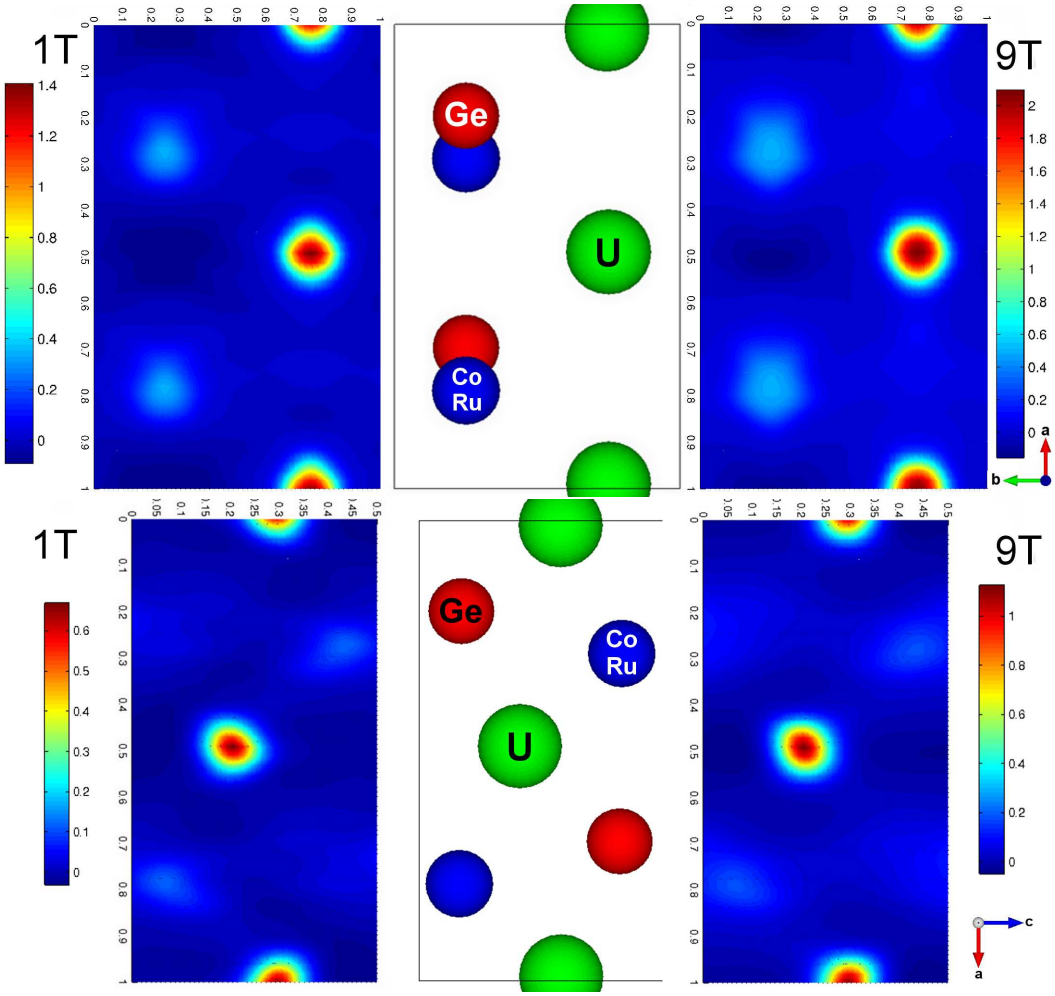

Figure 5.22: Upper part shows projection of the spin density to the $a-b$ plane as a result of the maximum entropy method while the lower part shows projection to the $a-c$ plane. Left panels show data from 1 T scan and right panels show data from higher field (9 T). Positive densities both on the Co(Ru) and U sites shows parallel alignment of the spins.

Results of this method are not burdened by any artificial effects and shows most probable solution that can be applied on the set of measured data. We can observe positive density both on the uranium and cobalt (ruthenium) sites. If we want to estimate magnetic moments centered on these ions we have to integrate densities in some defined volume. For this case we choose simple spheres centered on the atomic positions according to the unpolarized neutron diffraction results. Diameter of the sphere was estimated according to the density extent around the atom. Results of this integration are summarized in the Table 5.4.

Data treatment based on the maximum entropy method cannot provide us information about the spin and orbital component of the magnetic moment of each atom. For this reason is necessary to make up a spin density model and fit its parameters to the measured data. Model works on the basis of dipolar approximation and its fitting was done by FullProf[91]/WinPlotr[92] software. Our model involved magnetic moment centered on the uranium and cobalt ions. Regrettably spherical integrals are similar for both possible ion states of uranium – U^{3+} and U^{4+}. It makes it almost impossible to find the valency of uranium ion within this method. During refining of the magnetic

moment on cobalt ion we took into account only the spin momentum. We also tried to include magnetic density on ruthenium ion but obtained values of magnetic moment showed relative error of more than 250 %. Comparison of the measured flipping ratios and those calculated from the spin density model is plotted in Figure 5.23.

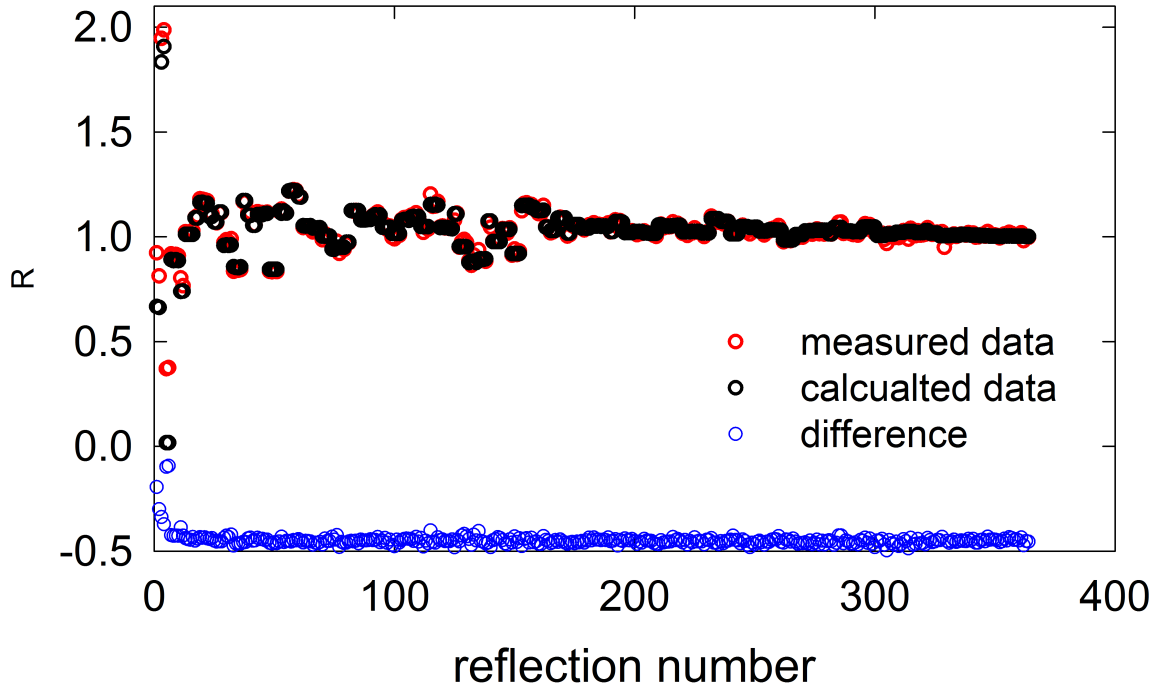

Figure 5.23: Measured flipping ratios and values from the spin density model. Blue circles show difference between measured and calculated data.

This method confirmed positive magnetic density both on the uranium and cobalt site. It also shows expected anti-parallel alignment of orbital and spin component on the uranium ion where orbital momentum is parallel to the momentum on cobalt. Results of this model are summarized in Table 5.4.

If we compare these results with parent compound it reveals significant differences. As has been mentioned above, polarized neutron diffraction experiments on UCoGe reports antiparallel alignment of the magnetic moment on the uranium and cobalt ions. It is contradictory to the situation in the doped system near $x_{\max}$ when our results from the single crystal $UCo_{0.88}Ru_{0.12}Ge$ shows parallel alignment. This reorientation of the magnetic moment on cobalt can lead to the increase of total magnetic moment and Curie temperature which is observed in magnetization data (see Figure 5.7) and in phase diagram in Figure 5.6. Compared quantities and directions of magnetic moments for parent compound and doped system are shown in Figure 5.24.

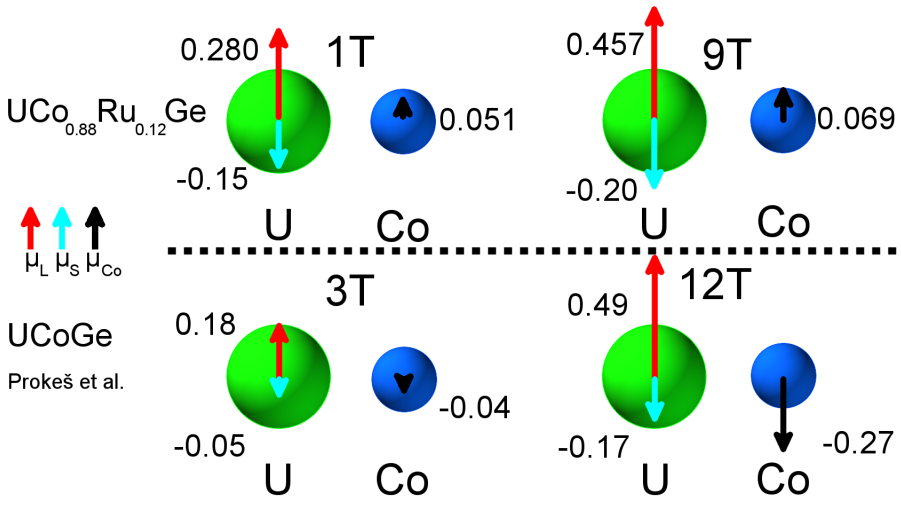

Figure 5.24: Comparison of the direction and values of magnetic moments and their components for the parent UCoGe compound[78] and results of our work on the doped $UCo_{0.88}Ru_{0.12}Ge$. Red arrows show orbital momentum, cyan arrows stands for spin component and black arrows marks momentum on the cobalt site. All values are in the units of Bohr magneton (μ_B) and lengths of all arrows are in the relative scale.

	MAXENT			‖	FullProf				
$\mu\,(\mu_B)$	μ_U	μ_{Co}	μ_{total}	‖	μ_{U_L}	μ_{U_S}	μ_U	μ_{Co}	μ_{total}
1 T	0.11(1)	0.07(1)	0.18(1)	‖	0.280(6)	-0.15(1)	0.13(2)	0.051(6)	0.18(2)
9 T	0.26(3)	0.08(1)	0.32(3)	‖	0.457(7)	-0.20(1)	0.25(2)	0.069(7)	0.32(2)

Table 5.4: Magnetic moments on U and Co positions according to the polarized neutron diffraction experiment on the $UCo_{0.88}Ru_{0.12}Ge$ single crystal. Table compares values obtained after integration of magnetic moment density from maximum entropy method with the values from model refined in FullProf.

5.2.4 Resistivity Measurements

Samples for the resistivity measurement were cut by precise wire saw from the block of accurately oriented single crystal in to the form of small blocks ($1 \times 1 \times 5\,mm^3$). Same as in the case of polycrystalline samples contacts were made of a gold wire welded on the sample. Temperature dependence of resistivity was measured in broad temperature range from 300 K down to the 0.4 K.

Further study of the anisotropy properties of the well doped $UCo_{0.88}Ru_{0.12}Ge$ shows significant difference between resistivity dependence along the b and c axes. Both of them exhibit high anisotropy even from room temperature. Temperature dependence of resistivity for b and c axis is plotted in Figure 5.25. Resistivity is slightly increasing down to the $\sim$ 227 K for current applied along the b axis and then it slowly goes down to the anomaly near 7.6 K corresponding to the Curie temperature. Similar dependence but with more pronounced maximum at far lower temperature $\sim$ 40 K is observed for the c axis. Shoulder on the resistance curve is again present at 7.6 K. Resistivity ratio R/R_{300} dependence for c axis below Curie temperature was fitted by Equation (5.1)[126].

$$\rho = \rho_0 + AT^2 + \frac{T}{\Delta}\left(1 + \frac{2T}{\Delta}\right)\exp\left(-\frac{\Delta}{T}\right) \tag{5.1}$$

Fit reveals that temperature dependence of resistivity obeys Fermi liquid quadratic dependence with A=1092(7) $\cdot 10^{-6}\,\mathrm{K}^{-2}$ together with the electron-spin wave scattering term with the value of gap $\Delta = 22.04(9)\,\mathrm{K}$. According to the Anderson[126] is this fitting reliable only for $T \ll \Delta$. This condition is in our case satisfied. Resulting fit is plotted in the inset of the Figure 5.25. Inset of the Figure 5.25 also shows no trace of anomaly corresponding to the Curie temperature in the external magnetic field of 9 T. The resistivity data are strongly influenced by external magnetic field (9 T) up to temperature 50 K where encounter with zero field data. We used the same equation for fitting the data which were measured for the b axis. In this case energy gap is approximately $\Delta = 29.1(6)\,\mathrm{K}$ and term for Fermi liquid quadratic dependence is A=4.3(1) $\cdot 10^{-4}\,\mathrm{K}^{-2}$.

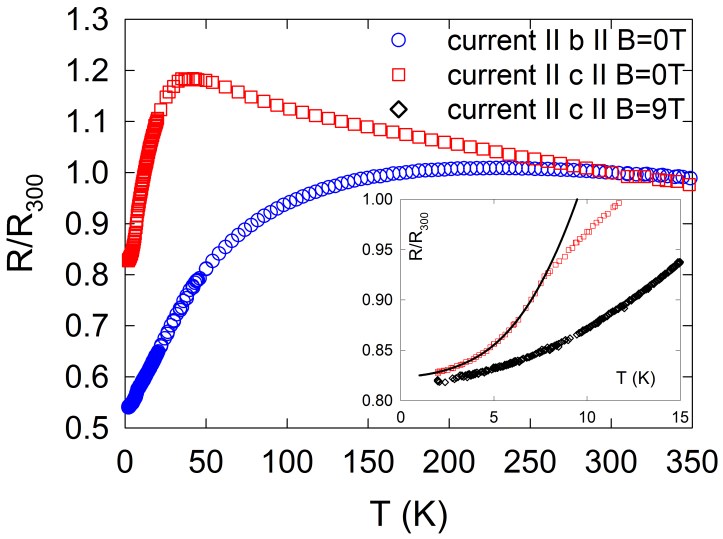

Figure 5.25: Temperature dependence of resistivity measured along the b and c axis of $UCo_{0.88}Ru_{0.12}Ge$ single crystal. Inset shows low temperature region where solid line represents the fit with Equation (5.1) and black diamonds are data from measurement in magnetic field of 9 T.

5.2.5 Dilatometry Measurements

Sample for dilatometry measurement was in the form of a cube (approximately $2 \times 2 \times 2\,\mathrm{mm}^3$) with the faces precisely oriented perpendicular to the a, b and c axis. Each face was consequently polished. Measurement was performed in the laboratory of TU Vienna in helium cryostat at temperatures down to the 3 K using capacitance dilatometry cell[109].

Different magnetic properties and electrical resistivity along all three axes are followed by different response of length to the change of temperature.

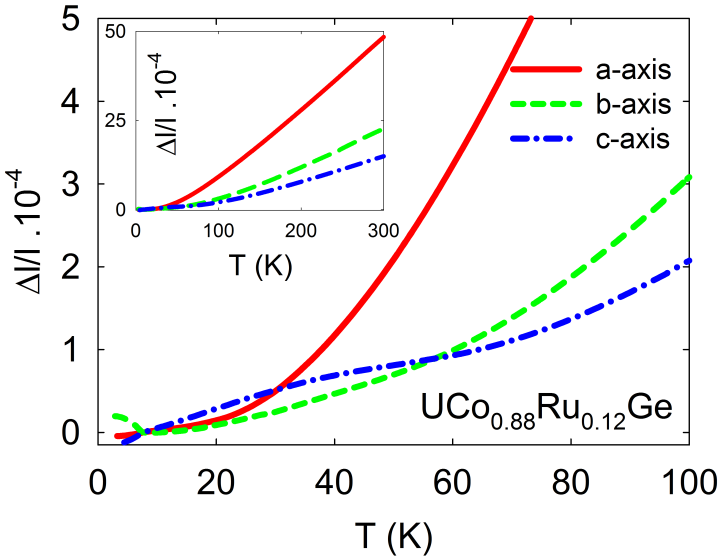

Figure 5.26: Thermal expansion at zero magnetic field for all three axes in the intermediate temperature range. Magnetic easy axis c is elastically hardest axes. Softest magnetic axes a shows highest extension with increased temperature. Inset shows behavior at broad temperature range up to the room temperature. Relative values are shifted so they have zero value at Curie temperature $T_C = 7.6\,\mathrm{K}$.

Thermal expansion measurements shows large anisotropy for all three axes (see Figure 5.26). Elastic properties above 60 K consistently correlate with the magnetocrystalline anisotropy behavior. Magnetic easy axis c (i.e. cell parameter c) shows smallest relative extension. Thus it is elastically hardest axes. Contradictory to that is magnetically hardest a axes that exhibit largest relative change (cell parameter a). This axis shows highest relative length change pointing on the elastically softest direction. And same as for magnetization curves b axis exhibits intermediate behavior. It is like that down to the 60 K where we can observe crossing between b and c axis. It is due to the change of curvature for the c axis below 60 K. Temperature dependence of relative length change exhibits some kind of bump at approximately 40 K. This anomaly has its counterpart at resistivity data measured along the c axis where it also has maximum in temperature dependence (Figure 5.25). Thermal expansion above Curie temperature holds the hierarchy of the axis in the order $a-b-c$ which is only reversed form of sequence $c-b-a$ present in magnetization data. However this similarity is broken below T_C. In ordered state is b axis increased with lowering temperature. On the other hand a and c axes are shortened. Curie temperature estimated from the thermal expansion data is in very good agreement with results of the heat capacity measurements and from temperature dependence of resistivity. All quantities are plotted in Figure 5.27 together with the coefficient of linear thermal expansion $\alpha\,(T)$. Coefficient of linear thermal expansion $\alpha\,(T) = \frac{1}{l}\frac{\partial l}{\partial T}$ is obtained as a numerical derivation of the relative length change with the temperature.

We used thermal expansion data for further investigation of the anisotropic properties of $UCo_{0.88}Ru_{0.12}Ge$. We fitted the data by additive relations assuming the vibrational and electronmagnetic contribution[115] according to the Equation(4.16) and (4.17). Obtained Debye temperatures from the fit for each axis together with the interval where the data were fitted are listed

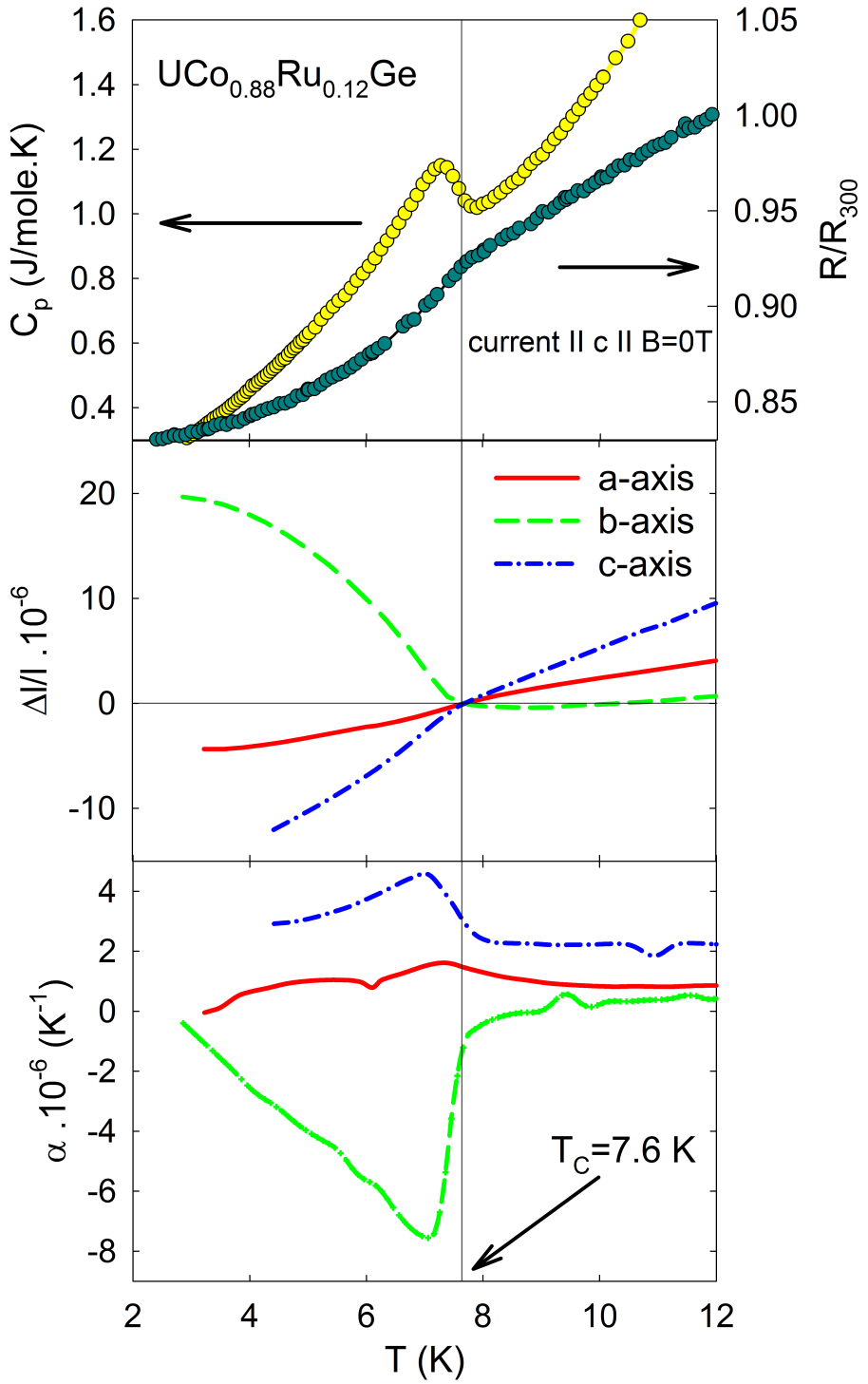

Figure 5.27: Comparison of heat capacity, resistivity along the c axis and thermal expansion data in the vicinity of Curie temperature $T_C = 7.6\,\mathrm{K}$. All quantities are measured in zero magnetic field. Solid line indicates the ordering temperature.

in Table 5.5. These values can be compared with the Debye temperature resulting from the heat capacity measurements. Refinement of the specific heat data revealed Debye temperature of 144 K. High Debye temperature of the magnetic easy axis shows that c direction is much harder than a axis that is almost aligned with the shortest distance between two nearest uranium atoms.

	a axis	b axis	c axis
Θ_{D} (K)	197	345	400
interval of the fit (K)	50-300	50-300	80-300

Table 5.5: Debye temperatures corresponding to all three axes obtained from the fitting of the Equation (4.16) on the thermal expansion data.

In order to find out the uniaxial and hydrostatic pressure dependence of Curie temperature we used the estimation by Ehrenfest relation (Equation (5.2)), where i stands for the different axis

$$\frac{\mathrm{d}T_{\mathrm{C}}}{\mathrm{d}p_i} = \frac{V_m \Delta\alpha_i}{\Delta\left(C/T\right)} \tag{5.2}$$

and $\Delta\alpha_i$ is a step in the linear thermal expansion coefficient and $\Delta\left(C/T\right)$ is a step in the specific heat divided by temperature both at the T_{C}. And finally $V_m = 3.14 \times 10^{-5}\,\mathrm{m}^3 \cdot \mathrm{mol}^{-1}$ is the molar volume of the compound. Value of the step of anomaly at specific heat divided by temperature was determined as $\Delta\left(C/T\right) = 0.061\,(2)\ \mathrm{J} \cdot \mathrm{mol}^{-1} \cdot \mathrm{K}^{-2}$. Uniaxial pressure dependence for each axis is summarized in Table 5.6 together with the estimated step in the coefficients of linear thermal expansion $\Delta\alpha_i$.

	a axis	b axis	c axis
$\Delta\alpha_i\ \left(10^{-6}\mathrm{K}^{-1}\right)$	1.3(1)	-10.0(2)	2.9(1)
$\frac{\mathrm{d}T_{\mathrm{C}}}{\mathrm{d}p_i}\ \left(\mathrm{K} \cdot \mathrm{GPa}^{-1}\right)$	0.67(7)	-5.2(3)	1.5(1)
p_{cr} (GPa)	-11(1)	1.5(1)	-5.1(4)

Table 5.6: Uniaxial pressure dependence for each axis estimated by Ehrenfest relation. p_{cr} is estimation for the critical pressure where Curie temperature goes to zero.

Calculated uniaxial pressure dependencies reveals that ferromagnetic order cannot be suppressed by uniaxial pressure along a and c direction – both values are positive (i.e. negative uniaxial pressure would be necessary). If we simply estimate linear pressure dependence of T_{C} we obtain critical pressure p_{cr} of $-11\,(1)$ GPa and $-5.1\,(4)$ GPa for a and c axis respectively. On the other hand, negative uniaxial pressure dependence for b axis promises possibility for suppression of the ordering temperature. Linear extrapolation gives us critical pressure of 1.5 (1) GPa what is experimentally easily accessible value. We can also calculate hydrostatic pressure dependence. For this purpose we summed coefficients of linear thermal expansion along all three axes and resulting coefficient of volumetric thermal expansion is plotted in Figure 5.28 as a function of temperature.

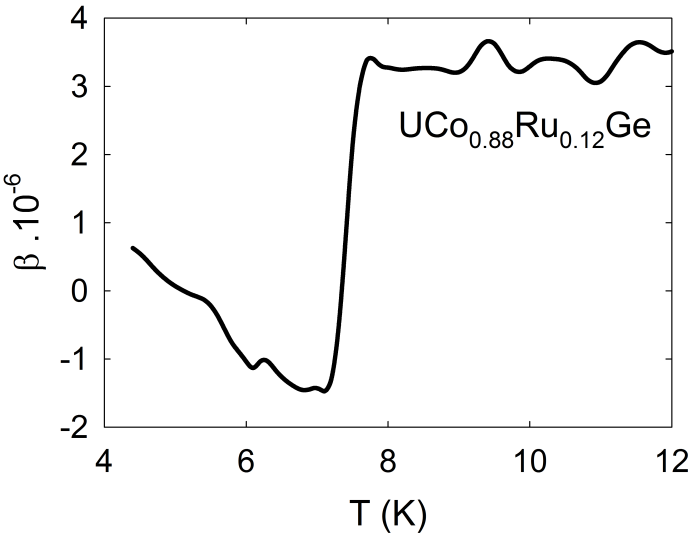

Figure 5.28: Coefficient of volumetric thermal expansion obtained as a sum of linear thermal expansion coefficients for all three directions.

If we use Ehrenfest relation (Equation (5.2)) for the step of volumetric expansion obtained as a sum of linear thermal expansion coefficients estimated as $\Delta\beta = 6.6\,(1)\cdot 10^{-6}\,\mathrm{K}^{-1}$ we obtain negative hydrostatic pressure dependence of $\frac{\mathrm{d}T_\mathrm{C}}{\mathrm{d}p_{hstat}} = -3.4\,(2)\ \mathrm{K}\cdot\mathrm{GPa}^{-1}$ which leads to experimentally accessible value of critical hydrostatic pressure $p_{\mathrm{cr,hydrostat}} = 2.2\,(2)$ GPa where ferromagnetism should disappear.

6 General Discussion

Proper study of the $UCo_{1-x}Ru_xGe$ system revealed linear change of the lattice parameters leading to the overall volume increase. While the cell parameter a is shortened the parameter d_{U-U} is reduced as well. This lead to the increase of the hybridization between $5f$ states on the neighboring uranium ions. As a consequence we should observe suppression of the magnetic order. Nevertheless data from the Arrott plot analysis, AC susceptibility measurement and derivation of the temperature dependence of the magnetization measured on the polycrystalline samples revealed initial steep increase of the Curie temperature and the magnetic moment. Both these quantities reaches their maximum at concentration $x_{max} \approx 0.1-0.12$ where Curie temperature reaches the value of $T_{C,max} \approx 9\,K$ and spontaneous magnetic moment is $0.11\,\mu_B$(see Figure 6.1 and 5.7). This is in agreement with results of Pospíšil et al.[17]. Mechanism that stands behind this increase was studied in the second part of this thesis and will be discussed below. Expected decrease of Curie temperature and the magnetic moment comes after this strengthening of the magnetic order. It is caused by above mentioned contraction of the d_{U-U} parameter and it is also result of the non-isoelectronic substitution of the ruthenium on the cobalt site. While removing one electron from the d shell we increase hybridization of the d and f orbitals and ferromagnetic order is even more reduced. This fact is projected to the decreasing tendency of the Curie temperature which is observed on the magnetization data and specific heat (See panel a) in Figure 6.1).

After proper study of temperature dependence of specific heat and resistivity we observed dramatic change of the behavior of these quantities similar to the case of U(Rh,Ru)Ge[127] and U(Co,Fe)Ge[19] system. Heat capacity data revealed almost linear dependence of the C_m/T in the logarithmic temperature scale for the sample with $x = 0.31$ (see Figure 5.12). It should be the sign of Non-Fermi liquid behavior, according to the Millis and Hertz [33, 32]. Another effect that might point on the dramatic change in the system is rapid increase of the Sommerfeld gamma coefficient of the specific heat (see panel c) in Figure 6.1). It reaches the value of $160\,mJ/mol \cdot K^2$ for $x = 0.3$. Further increase of ruthenium content leads to the decrease of this value.

Refinement of the resistivity revealed another evidence for the Non-Fermi liquid behavior in the system. Fitting of the equation $\rho = \rho_0 + AT^n$ on the low temperature part of the resistivity shows decrease of the n coefficient down to the value of 1.1 (see Figure 5.15 and panel b) in Figure 6.1). Linear temperature dependency of the resistivity is a sign of the Non-Fermi liquid behavior in the three dimensional ferromagnet[33, 32].

All these signs bring us to the conclusion that we have strong evidence of the Non-Fermi liquid behavior within the system for the concentration near critical concentration x_{cr}. Above mentioned findings are graphically summarized in Figure 6.1. This set of three panels shows that there exists some certain critical concentration where ferromagnetic order disappears and Non-Fermi liquid behavior is observed at the same time. Comparison with the results of Huy et al.[127] on the similar U(Rh,Ru)Ge system and Huang et al.[19] on the even more analogous U(Co,Fe)Ge might point on the presence of Ferromagnetic Quantum Critical Point present at the critical concentration x_{cr}. The red stripe in Figure 6.1 marks the region where x_{cr} should be present (i.e. between $x = 0.30$ and $x = 0.31$). For more accurate specifying of the value we took use of the fact, that decrease of Curie temperature scales according to the theoretical predictions as a $T_C \sim (x_{cr} - x)^{3/4}$. Fitting to this dependency resulted in the value for critical concentration of $x_{cr} = 0.308(9)$ (see Figure 5.10).

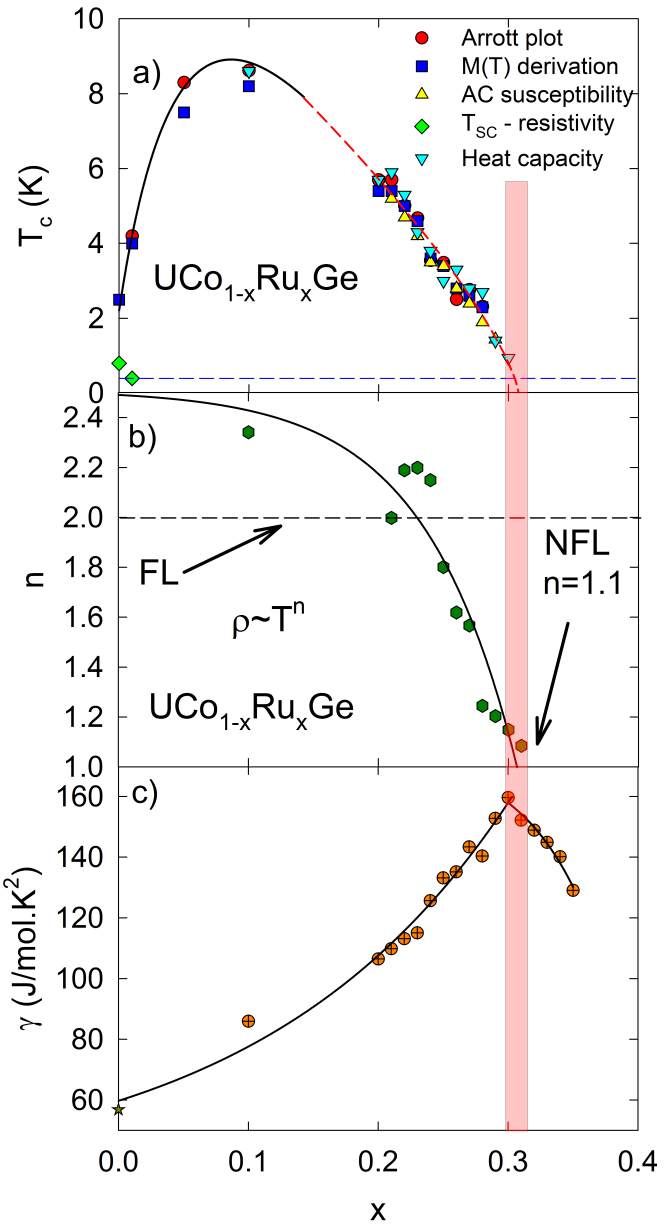

Figure 6.1: Panel a) shows phase diagram based on measurements of polycrystalline samples. T_C is taken as a result of Arrott plot analysis. Other estimations from the derivative of the temperature dependence of magnetization, from the peak of AC susceptibility and from inflection point of specific heat are plotted as well. Plot is supplemented by the results of the resistivity measurement revealing occurrence of superconductivity in the parent UCoGe compound and in the polycrystalline $UCo_{0.99}Ru_{0.01}Ge$. These two data points were taken from work of Pospíšil et al.[17]. Black solid line is only guide for the eye while the red dashed part is a fit of $T_C \sim (x_{cr} - x)^{3/4}$. Details of this fit are described in the text and also plotted in Figure 5.10. Blue dashed line represents the lowest temperature limit for performed measurement(0.4 K). Panel b) shows coefficients n from fitting of the low temperature dependence of resistivity with equation $\rho = \rho_0 + AT^n$. Dashed line shows the expected value for the ordinary Fermi liquid behavior. And finally panel c) shows development of Sommerfeld γ coefficient obtained from the heat capacity data. Data point for parent UCoGe which is marked by gold star is taken from the work of Gasparini et al.[122]. Red stripe shows the region of critical concentration x_{cr} with possible Quantum Critical Point.

Second part of the thesis elucidates the mechanism that stands behind the initial increase of magnetic moment and Curie temperature in the system. We have prepared high quality single crystal near concentration $x_{max}$with composition of $UCo_{0.88}Ru_{0.12}Ge$. It exhibited strong magnetocrystalline anisotropy (see Figure 5.17) and it shows to be uniaxial ferromagnet with c axis as the magnetic easy axis. It is in general agreement with parent UCoGe compound, but the value of spontaneous magnetic moment is significantly higher ($0.21\,\mu_B$). Curie temperature is enhanced as well ($T_C = 7.6\,K$). We performed polarized neutron diffraction on this single crystal in order to find out the values and directions of magnetic moments in the compound. Maximum entropy method revealed magnetic moment both on the uranium and cobalt ions (see Figure 5.22). This is in agreement with the results for the parent compound according to the Prokeš et al.[128]. But contrary to the negative spin density on cobalt site for UCoGe, we observed positive spin density both on the uranium and cobalt ion. This is pointing to the fact, that magnetic moments on the uranium and cobalt in the $UCo_{0.88}Ru_{0.12}Ge$ are no more anti parallel like in the case of UCoGe, but they point in the same direction. This leads to the increase of the magnetic moment and Curie temperature which was observed in previous study on poly crystals 6.2. We were able to distinguish between orbital and spin components of magnetic moment on the uranium ion thanks to the model of magnetic moments density. Results of this data treatment are summarized in Figure 5.24 and in Table 5.4. We propose two mechanisms of the spin reorientation on the cobalt site. Similarly to the spin-flip and spin-flop metamagnetic transitions either gradual or sudden reorientation of magnetic moment on the cobalt ion are possible. Proper study of this reorientation and possible connection with the presence of the superconductivity is necessary and will be discussed in the following section.

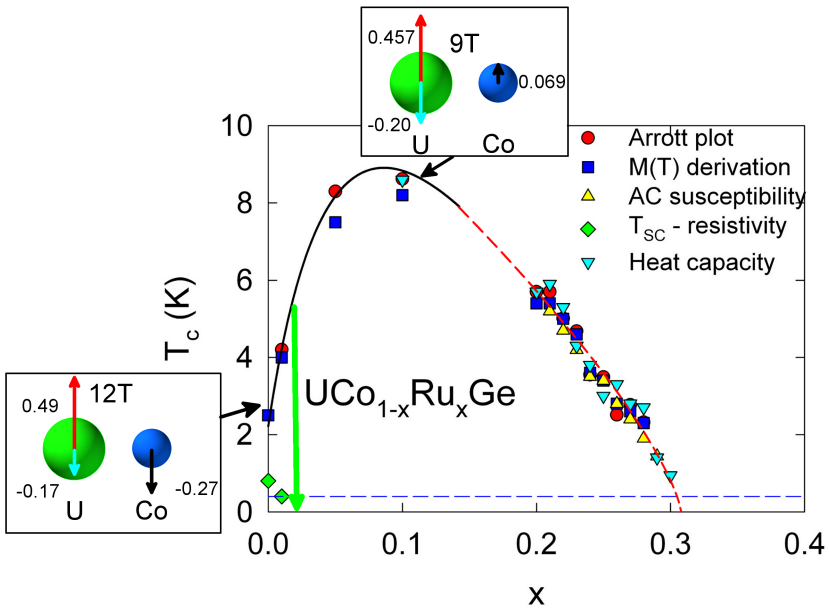

Figure 6.2: Phase diagram of the $UCo_{1-x}Ru_xGe$ system together with the sketches of the orientation of the magnetic moment on the uranium and cobalt site. We used the same notation as in the Figure 5.6. Data for the UCoGe are taken from Prokeš et al.[78]. Green arrow shows the region where magnetic moment on the cobalt site should be zero. It is expected at the same concentration where superconductivity disappears.

Strong anisotropy properties of the $UCo_{0.88}Ru_{0.12}Ge$ single crystal were observed also on the resistivity data. Here we can observe clearly pronounced maximum in the temperature dependence of resistivity at $\sim 40\,K$ if we measured along the c axis. On the other hand temperature dependence of resistivity along the b axis shows only broad plateau. At lower temperatures is resistivity for both the c and b direction quadratic dependent on the temperature. Dilatometry study on the $UCo_{0.88}Ru_{0.12}Ge$ compound revealed that thermal expansion is strongly anisotropic as well. Anomaly at $\sim 40\,K$ for thermal expansion along the c axis might be possible counterpart to the maximum in the temperature dependence of resistivity. Calculations based on Ehrenfest relations (equation (5.2)) using precise dilatometry and heat capacity data were used for estimation of the dependence of T_C on the uniaxial pressure (see Table 5.6). It revealed that uniaxial pressure applied along the a or c axis should increase the Curie temperature while the pressure on the b axis should suppress ferromagnetic order in the compound at 1.5 GPa. Similar result as for the b direction counts also for the hydrostatic case where critical value of the applied pressure should be approximately 2.2 GPa.

7 Conclusions

This work brings unique report on the development of the magnetic order in the $UCo_{1-x}Ru_xGe$ system. Broad range of measurements performed on the polycrystalline samples reveal dramatic increase both of the ordering temperature and the magnetic moment with increasing ruthenium content. Peak of this trend is at concentration $x_{max} \approx 0.1 - 0.12$ where Curie temperature reaches the value of $T_{C,max} \approx 9\,K$ and spontaneous magnetic moment is $0.075\,\mu_B$(see Figure 5.65.7). Background of this magnetic order strengthening in comparison to UCoGe was studied on single crystal with composition $UCo_{0.88}Ru_{0.12}Ge$ that is in vicinity of x_{max}. It exhibits strong magneto-crystalline anisotropy confirming that $UCo_{0.88}Ru_{0.12}Ge$ is strongly uniaxial ferromagnet with easy axis c, same as for UCoGe (see Figure 5.17). In addition this doped system exhibits enhanced magnetic moment of about 85 %. Polarized neutron diffraction experiments performed on this high quality single crystal revealed presence of magnetic moments both on the uranium and cobalt sites. Moments on these ions are oriented parallel 5.24, i.e. opposite to the case of parent UCoGe[78]. This spin reorientation leads to the increase of the total magnetic moment observed in the phase diagram of the system (see Figure 6.2).

Calculations based on Ehrenfest relations (equation (5.2)) using precise dilatometry and heat capacity data revealed strong anisotropy of the system. It is expressed by different response of T_C on the uniaxial pressure (see Table 5.6). Anisotropy of transport properties is also noticeable on the temperature dependence of resistivity (see Figure 5.25). Highly expressed maximum (knee) in the resistivity along the c direction has its counterpart in the dilatometry data (see Figure 5.26).

Rapid increase of the ordering temperature and magnetic moment is changed for concentrations $x > x_{max}$ where steady decrease of these quantities is observed. The tendency how T_C is lowered with control parameter (concentration) x is in very good agreement with theoretical predictions for three dimensional ferromagnets exhibiting Non-Fermi liquid behavior[33, 32]. It is scaled with $T_C \sim (x_{cr} - x)^{3/4}$ where critical concentration can be estimated as $x_{cr} \approx 0.308$ (see Figure 5.10). Signs of Non-Fermi liquid behavior are also observed in the heat capacity (see Figure 5.12 and panel c) in Figure 6.1) and resistivity data (see Figure 5.15 and panel b) in Figure 6.1). It might be a sign of possible presence of the Quantum Critical Point at critical concentration x_{cr}.

Our results show, that U(Co,Ru)Ge system is similar to the previously reported U(Rh,Ru)Ge[127] or U(Co,Fe)Ge[19] where Quantum Critical Point was reported.

Brief outlook of the future plans follows in the next chapter.

8 Future Plans

Next step in our study will be focused on the most interesting part in the phase diagram of the $UCo_{1-x}Ru_xGe$ system - the vicinity of critical concentration x_{cr}. Results of this work shows, that signs of Non-Fermi liquid behavior predict presence of QCP in this region. Studied system, in the vicinity of QCP, should exhibit strong anisotropy properties as well. For this reason and also for more reliable results then from polycrystalline samples we have successfully prepared high quality single crystal with composition of $UCo_{0.7}Ru_{0.3}Ge$ where presence of QCP is expected. Single crystal has been prepared by Czochralski method in tri-arc furnace. Quantum critical features will be intensively studied in upcoming days on grown crystal in detail. We will try to bring precise picture of the behavior near QCP based on the measurement of various quantities and not only at ambient pressure, but under hydrostatic and uniaxial pressure as well. Applying of the pressure should shift the system to the QCP in the same way as in the parent UCoGe.

Further research is planed in the left part of the phase diagram. At first we should bring some theoretical background and possible explanation for the parallel alignment of the moments on uranium and cobalt in $UCo_{0.88}Ru_{0.12}Ge$ crystal. According to that *ab initio* calculations should be performed in similar way as for the parent compound. Then we should focus on the region where we can expect zero magnetic moment on the cobalt site (or its reorientation) in the $UCo_{1-x}Ru_xGe$ system. It should happen for some certain concentration in the region $0 < x \lesssim x_{max}$. Disappearance of superconductivity is also observed in the same range so possible connection of these two effects should be studied as a part of our following research. For this reason we plan another polarized neutron study on the single crystal with composition of $UCo_{0.97}Ru_{0.03}Ge$ where we expect that superconductivity is on the border of its presence (see Figure 6.2). This single crystal has been already prepared by Czochralski method in the tri-arc furnace as well.

Interesting difference in the response of the Curie temperature on the uniaxial pressure that we predicted for the $UCo_{0.88}Ru_{0.12}Ge$ was experimentally investigated in recent days.

References

[1] Heike Kamerlingh-Onnes. *Comm. Phys. Lab. Univ. Leiden*, 122, 1911.

[2] J. Bardeen, L. N. Cooper, and J. R. Schrieffer. Theory of superconductivity. *Physical Review*, 108(5):1175–1204, 1957. PR.

[3] J. Bardeen, L. N. Cooper, and J. R. Schrieffer. Microscopic theory of superconductivity. *Physical Review*, 106(1):162–164, 1957. PR.

[4] J. G. Bednorz and K. A. Müller. Possible hight c superconductivity in the ba-la-cu-o system. *Zeitschrift für Physik B Condensed Matter*, 64(2):189–193, 1986.

[5] Ø Fischer, A. Treyvaud, R. Chevrel, and M. Sergent. Superconductivity in the rexmo6s8. *Solid State Communications*, 17(6):721–724, 1975.

[6] B. T. Matthias, E. Corenzwit, J. M. Vandenberg, and H. E. Barz. High superconducting transition temperatures of new rare earth ternary borides. *Proc Natl Acad Sci U S A*, 74(4): 1334–5, 1977. Matthias, B T Corenzwit, E Vandenberg, J M Barz, H E United States Proc Natl Acad Sci U S A. 1977 Apr;74(4):1334-5.

[7] F. Steglich, J. Aarts, C. D. Bredl, W. Lieke, D. Meschede, W. Franz, and H. Schäfer. Superconductivity in the presence of strong pauli paramagnetism: $Cecu_2si_2$. *Physical Review Letters*, 43(25):1892–1896, 1979. PRL.

[8] S. S. Saxena, P. Agarwal, K. Ahilan, F. M. Grosche, R. K. W. Haselwimmer, M. J. Steiner, E. Pugh, I. R. Walker, S. R. Julian, P. Monthoux, G. G. Lonzarich, A. Huxley, I. Sheikin, D. Braithwaite, and J. Flouquet. Superconductivity on the border of itinerant-electron ferromagnetism in uge2. *Nature*, 406(6796):587–592, 2000. 10.1038/35020500.

[9] Dai Aoki, Andrew Huxley, Eric Ressouche, Daniel Braithwaite, Jacques Flouquet, Jean-Pascal Brison, Elsa Lhotel, and Carley Paulsen. Coexistence of superconductivity and ferromagnetism in urhge. *Nature*, 413(6856):613–616, 2001. 10.1038/35098048.

[10] T. Akazawa, H. Hidaka, T. Fujiwara, T. C. Kobayashi, E. Yamamoto, Y. Haga, R. Settai, and Y. Onuki. Pressure-induced superconductivity in ferromagnetic uir without inversion symmetry. *Journal of Physics: Condensed Matter*, 16(4):L29, 2004.

[11] N. T. Huy, A. Gasparini, D. E. de Nijs, Y. Huang, J. C. P. Klaasse, T. Gortenmulder, A. de Visser, A. Hamann, T. Gorlach, and H. von Lohneysen. Superconductivity on the border of weak itinerant ferromagnetism in ucoge. *Physical Review Letters*, 99(6):067006, 2007. Times Cited: 52 Article English de Visser, A Univ Amsterdam, Van Der Waals Zeeman Inst, Valckenierstr 65, NL-1018 XE Amsterdam, Netherlands Cited References Count: 24 198YZ AMER PHYSICAL SOC ONE PHYSICS ELLIPSE, COLLEGE PK, MD 20740-3844 USA COLLEGE PK.

[12] D. Fay and J. Appel. Coexistence of p-state superconductivity and itinerant ferromagnetism. *Physical Review B*, 22(7):3173–3182, 1980. PRB.

[13] V. Sechovsky and L. Havela. *Chapter 1 Magnetism of ternary intermetallic compounds of uranium*, volume Volume 11, pages 1–289. Elsevier, 1998.

[14] R. Troc and V. H. Tran. Magnetic properties of ut(si, ge) series. *Journal of Magnetism and Magnetic Materials*, 73(3):389–397, 1988.

[15] K. H. J. Buschow, E. Bruck, R. G. van Wierst, F. R. de Boer, L. Havela, V. Sechovsky, P. Nozar, E. Sugiura, M. Ono, M. Date, and A. Yamagishi. Specific heat and magnetic behavior of utge compounds. *Journal of Applied Physics*, 67(9):5215–5217, 1990.

[16] E. Hassinger, D. Aoki, G. Knebel, and J. Flouquet. Pressure-temperature phase diagram of polycrystalline ucoge studied by resistivity measurement. *Journal of the Physical Society of Japan*, 77(7):073703, 2008. Times Cited: 12 Article English Hassinger, E CEA, SPSMS, Inst Nanosci and Cryogenics, 17 Rue Martyrs, F-38054 Grenoble 9, France Cited References Count: 18 328YF PHYSICAL SOC JAPAN EISHIN-KAIHATSU BLDG, 5TH FLR, 5-34-3 SHINBASHI, MINATO-KU, TOKYO 105-0004, JAPAN MINATO-KU.

[17] J. Pospisil, J. P. Vejpravova, M. Divis, and V. Sechovsky. Ferromagnetism in ucoge stabilized by transition metal doping. *Journal of Applied Physics*, 105(7):07E114, 2009. Times Cited: 1 Proceedings Paper English Pospisil, J Charles Univ Prague, Fac Math and Phys, DCMP, Ke Karlovu 5, CR-12116 Prague 2, Czech Republic Cited References Count: 13 453SX AMER INST PHYSICS CIRCULATION and FULFILLMENT DIV, 2 HUNTINGTON QUADRANGLE, STE 1 N O 1, MELVILLE, NY 11747-4501 USA MELVILLE.

[18] S. Sakarya, N. T. Huy, N. H. van Dijk, A. de Visser, M. Wagemaker, A. C. Moleman, T. J. Gortenmulder, J. C. P. Klaasse, M. Uhlarz, and H. Löhneysen. Evolution of ferromagnetic order in urhge alloyed with ru, co and si. *Journal of Alloys and Compounds*, 457(1-2):51–56, 2008.

[19] K. Huang, J. J. Hamlin, R. E. Baumbach, M. Janoschek, N. Kanchanavatee, D. A. Zocco, F. Ronning, and M. B. Maple. Ferromagnetic quantum critical point in $\mathrm{uco}_{1-x}\mathrm{fe}_x\mathrm{ge}$. *Physical Review B*, 87(5):054513, 2013. PRB.

[20] Stephen Blundell. *Magnetism in Condensed Matter (Oxford Master Series in Physics)*. Oxford University Press, USA, 2001.

[21] K.H.J. Buschow. *Concise Encyclopedia of Magnetic and Superconducting Materials*. Elsevier Science, 2005.

[22] C.P. Poole, H.A. Farach, R.J. Creswick, and R. Prozorov. *Superconductivity*. Elsevier Science, 2010.

[23] Börje Johansson and Hans L. Skriver. Electronic structure of the actinide metals. *Journal of Magnetism and Magnetic Materials*, 29(1-3):217–229, 1982.

[24] H. H. Hill. Plutonium 1970 and other actinides. pages 1 – 19.

[25] M. A. Ruderman and C. Kittel. Indirect exchange coupling of nuclear magnetic moments by conduction electrons. *Physical Review*, 96(1):99–102, 1954. PR.

[26] T. Kasuya. A theory of metallic ferro- and antiferromagnetism on zener's model. *Progress of Theoretical Physics*, 16:45–57, 1956.

[27] Kei Yosida. Magnetic properties of cu-mn alloys. *Physical Review*, 106(5):893–898, 1957. PR.

[28] Piers Coleman and Andrew J. Schofield. Quantum criticality. *Nature*, 433(7023):226–229, 2005. 10.1038/nature03279.

[29] D. Belitz and T. R. Kirkpatrick. Quantum phase transitions, n/a 1, 2000 2000.

[30] G. R. Stewart. Non-fermi-liquid behavior in d- and f-electron metals. *Reviews of Modern Physics*, 73(4):797–855, 2001. RMP.

[31] C. L. Seaman, M. B. Maple, B. W. Lee, S. Ghamaty, M. S. Torikachvili, J. S. Kang, L. Z. Liu, J. W. Allen, and D. L. Cox. Evidence for non-fermi liquid behavior in the kondo alloy $y_{1-x}u_xpd_3$. *Physical Review Letters*, 67(20):2882–2885, 1991. PRL.

[32] John A. Hertz. Quantum critical phenomena. *Physical Review B*, 14(3):1165–1184, 1976. PRB.

[33] A. J. Millis. Effect of a nonzero temperature on quantum critical points in itinerant fermion systems. *Physical Review B*, 48(10):7183–7196, 1993. PRB.

[34] T. Moriya and Tetsuya Takimoto. Anomalous properties around magnetic instability
 in heavy electron systems. *Journal of the Physical Society of Japan*, 64(Copyright (C) 1995 The Physical Society of Japan):960, 1995.

[35] G. G. Lonzarich. *Electron*. Cambridge University Press, 1997.

[36] A. A. Abrikosov and I. M. Khalatnikov. The theory of a fermi liquid (the properties of liquid 3 he at low temperatures). *Reports on Progress in Physics*, 22(1):329, 1959.

[37] Moshe Kaveh and Nathan Wiser. Electron-electron scattering in conducting materials. *Advances in Physics*, 33(4):257–372, 1984.

[38] Katsuya Shimizu, Tomohiro Kimura, Shigeyuki Furomoto, Keiki Takeda, Kazuyoshi Kontani, Yoshichika Onuki, and Kiichi Amaya. Superconductivity in the non-magnetic state of iron under pressure. *Nature*, 412(6844):316–318, 2001. 10.1038/35085536.

[39] W. Meissner and R. Ochsenfeld. Ein neuer effekt bei eintritt der supraleitfÃ€higkeit. *Naturwissenschaften*, 21(44):787–788, 1933.

[40] K.H. Bennemann and J.B. Ketterson. *Superconductivity: Conventional and unconventional superconductors. Vol. 1.* Springer, 2008.

[41] J. R. Gavaler. Superconductivity in nb3ge films above 22 k. *Applied Physics Letters*, 23(8): 480–482, 1973.

[42] P. Monthoux, D. Pines, and G. G. Lonzarich. Superconductivity without phonons. *Nature*, 450(7173):1177–1183, 2007. 10.1038/nature06480.

[43] M. Tinkham. *Introduction to superconductivity*. Dover Publications, Incorporated, 1996.

[44] T. R. Kirkpatrick, D. Belitz, Thomas Vojta, and R. Narayanan. Strong enhancement of superconducting t_c in ferromagnetic phases. *Physical Review Letters*, 87(12):127003, 2001. PRL.

[45] V. P. Mineev. Pressure-temperature phase diagram of ferromagnetic superconductors. *Journal of the Physical Society of Japan*, 77(10):103702, 2008. Times Cited: 3 Article English Mineev, V. P INAC SPSMS, Commissariat Energie Atom, F-38054 Grenoble, France Cited References Count: 15 362YQ PHYSICAL SOC JAPAN EISHIN-KAIHATSU BLDG, 5TH FLR, 5-34-3 SHINBASHI, MINATO-KU, TOKYO 105-0004, JAPAN MINATO-KU.

[46] Yoshichika Onuki, Isamu Ukon, Sung Won Yun, Izuru Umehara, Kazuhiko Satoh, Tadashi Fukuhara, Hideyuki Sato, Shigeru Takayanagi, Mikio Shikama, and Akira Ochiai. Magnetic and electrical properties of u-ge intermetallic compounds. *Journal of the Physical Society of Japan*, 61(Copyright (C) 1992 The Physical Society of Japan):293, 1992.

[47] Gendo Oomi, Tomoko Kagayama, Kazutaka Nishimura, S. W. Yun, and Yoshichika Onuki. Electrical resistivity of single crystalline uge2 at high pressure and high magnetic field. *Physica B: Condensed Matter*, 206-207(0):515–518, 1995.

[48] Huxley Andrew, Ressouche Eric, Grenier Beatrice, Aoki Dai, Flouquet Jacques, and Pfleiderer Christian. The co-existence of superconductivity and ferromagnetism in actinide compounds. *Journal of Physics: Condensed Matter*, 15(28):S1945, 2003.

[49] H. Kotegawa, A. Harada, S. Kawasaki, Y. Kawasaki, Y. Kitaoka, Y. Haga, E. Yamamoto, Y. nuki, K. M. Itoh, E. E. Haller, and H. Harima. Evidence for uniform coexistence of ferromagnetism and unconventional superconductivity in uge_2: A ^{73}ge-nqr study under pressure. *Journal of the Physical Society of Japan*, 74(Copyright (C) 2005 The Physical Society of Japan):705, 2005.

[50] A. Huxley, I. Sheikin, and D. Braithwaite. Metamagnetic behavior near the quantum critical point in uge2. *Physica B: Condensed Matter*, 284-288, Part 2(0):1277–1278, 2000.

[51] Andrew Huxley, Ilya Sheikin, Eric Ressouche, Nolwenn Kernavanois, Daniel Braithwaite, Roberto Calemczuk, and Jacques Flouquet. Uge_2: A ferromagnetic spin-triplet superconductor. *Physical Review B*, 63(14):144519, 2001. PRB.

[52] C. Pfleiderer and A. D. Huxley. Pressure dependence of the magnetization in the ferromagnetic superconductor uge_2. *Physical Review Letters*, 89(14):147005, 2002. PRL.

[53] V. Taufour, D. Aoki, G. Knebel, and J. Flouquet. Tricritical point and wing structure in the itinerant ferromagnet uge_2. *Physical Review Letters*, 105(21):217201, 2010. PRL.

[54] Hisashi Kotegawa, Valentin Taufour, Dai Aoki, Georg Knebel, and Jacques Flouquet. Evolution toward quantum critical end point in uge_2. *Journal of the Physical Society of Japan*, 80 (Copyright (C) 2011 The Physical Society of Japan):083703, 2011.

[55] Dai Aoki and Jacques Flouquet. Ferromagnetism and superconductivity in uranium compounds. *Journal of the Physical Society of Japan*, 81(Copyright (C) 2012 The Physical Society of Japan):011003, 2012.

[56] A. V. Andreev, R. Z. Levitin, Yu. F. Popov, and R. Yu. Yumaguzhin. *Sov. Phys. Solid State*, 27, 1985.

[57] L. Havela, L. Neuzil, V. Sechovsky, A. V. Andreev, C. Schmitzer, and G. Hilscher. Magnetic properties of uxco x=sn, al, ga. *Journal of Magnetism and Magnetic Materials*, 54-57, Part 1(0):551–552, 1986.

[58] V. Sechovsky, L. Havela, F. R. de Boer, J. J. M. Franse, P. A. Veenhuizen, J. Sebek, J. Stehno, and A. V. Andreev. Systematics across the utx series (t = ru, co, ni; x = al, ga, sn) of high-field and low-temperature properties of non-ferromagnetic compounds. *Physica B+C*, 142(3): 283–293, 1986.

[59] V. Sechovsky, L. Havela, N. Pillmayr, G. Hilscher, and A. V. Andreev. On the magnetic behaviour of ugat series. *Journal of Magnetism and Magnetic Materials*, 63-64(0):199–201, 1987.

[60] A. Veenhuizen, P., R. de Boer, F., A. Menovsky, A., V. Sechovsky, and L. Havela. Magnetic properties of urual and urhal single crystals. *J. Phys. Colloques*, 49(C8):C8–485–C8–486, 1988.

[61] F. Canepa, P. Manfrinetti, M. Pani, and A. Palenzona. Structural and transport properties of some utx compounds where t=fe, co, ni and x=si, ge. *Journal of Alloys and Compounds*, 234(2):225–230, 1996. Times Cited: 39 Article English Cited References Count: 16 TX651 ELSEVIER SCIENCE SA LAUSANNE.

[62] A. V. Andreev, F. Honda, V. Sechovsky, M. DiviÅ¡, N. Izmaylov, O. Chernyavski, Y. Homma, and Y. Shiokawa. Magnetic properties of single crystalline ufesi. *Journal of Alloys and Compounds*, 335(1-2):91–94, 2002.

[63] Martin Divis, Lutz Steinbeck, Manuel Richter, and Peter Mohn. Density functional prediction of a magnetic ground state of ufesi. *Journal of Alloys and Compounds*, 321(1):10–16, 2001.

[64] K. Prokes, M. Divis, P. Mohn, K. Schwarz, V. Sechovsky, P. Svoboda, M. Richter, K. H. J. Buschow, E. Bruck, and F. R. de Boer. Reduced magnetic moments in unisi. *Journal of Alloys and Compounds*, 269(1-2):43–49, 1998.

[65] Fuminori Honda, Alexander V. Andreev, Vladimir Sechovsky, and Karel Prokes. Magnetic properties of a urhsi single crystal. *Physica B: Condensed Matter*, 329-333, Part 2(0):486–488, 2003.

[66] K. Prokes, V. Sechovsky, R. A. Robinson, R. Sonntag, P. Svoboda, and F. R. de Boer. Commensurate and incommensurate magnetic order of updsi. *Physica B: Condensed Matter*, 241-243(0):687–689, 1997.

[67] F. R. De Boer, E. Bruck, V. Sechovsky, L. Havela, and K. H. J. Buschow. Utx compounds in high magnetic fields. *Physica B: Condensed Matter*, 163(1-3):175–178, 1990.

[68] B. Chevalier, B. Lloret, P. Gravereau, B. Buffat, and J. Etourneau. Kondo fluctuations and magnetism in the new equiatomic ternary compounds uirsi and uirge. *Journal of Magnetism and Magnetic Materials*, 75(1-2):13–18, 1988.

[69] K. Prokes, V. Sechovsky, E. Bruck, F. Bouree, G. Andre, V. H. Tran, R. Sonntag, F. R. de Boer, K. H. J. Buschow, R. Troc, K. Kindo, and H. Maletta. Magnetic ordering in uptsi. *Physica B: Condensed Matter*, 225(3-4):166–176, 1996.

[70] James Jeffrey Hamlin, Ryan Eagle Baumbach, Kevin Huang, Marc Janoschek, Noravee Kanchanavatee, Diego A. Zocco, and M. Brian Maple. Evolution of the magnetic and superconducting states in ucoge with fe and ni substitution. *MRS Online Proceedings Library*, 1264: null–null, 2010.

[71] N. T. Huy, D. E. de Nijs, Y. K. Huang, and A. de Visser. Unusual upper critical field of the ferromagnetic superconductor ucoge. *Physical Review Letters*, 100(7):077002, 2008. Times Cited: 17 Article English Huy, N. T Univ Amsterdam, Van der Waals Zeeman Inst, Valckenierstr 65, NL-1018 XE Amsterdam, Netherlands Cited References Count: 26 265CO AMER PHYSICAL SOC ONE PHYSICS ELLIPSE, COLLEGE PK, MD 20740-3844 USA COLLEGE PK.

[72] A. de Visser, N. T. Huy, A. Gasparini, D. E. de Nijs, D. Andreica, C. Baines, and A. Amato. Muon spin rotation and relaxation in the superconducting ferromagnet ucoge. *Physical Review Letters*, 102(16):167003, 2009. Times Cited: 11 Article English de Visser, A Univ Amsterdam, Van der Waals Zeeman Inst, Valckenierstr 65, NL-1018 XE Amsterdam, Netherlands Cited References Count: 29 437IC AMER PHYSICAL SOC ONE PHYSICS ELLIPSE, COLLEGE PK, MD 20740-3844 USA COLLEGE PK.

[73] E. Slooten, T. Naka, A. Gasparini, Y. K. Huang, and A. de Visser. Enhancement of superconductivity near the ferromagnetic quantum critical point in ucoge. *Physical Review Letters*, 103(9):097003, 2009. Times Cited: 9 Article English Slooten, E Univ Amsterdam, Van der Waals Zeeman Inst, Valckenierstr 65, NL-1018 XE Amsterdam, Netherlands Cited References Count: 26 493FA AMER PHYSICAL SOC ONE PHYSICS ELLIPSE, COLLEGE PK, MD 20740-3844 USA COLLEGE PK.

[74] D. E. de Nijs, N. T. Huy, and A. de Visser. Simultaneous suppression of ferromagnetism and superconductivity in ucoge by si substitution. *Physical Review B*, 77(14):140506R, 2008. Times Cited: 6 Article English De Nijs, D. E Univ Amsterdam, Van Der Waals Zeeman Inst, Valckenierstr 65, NL-1018 XE Amsterdam, Netherlands Cited References Count: 26 295EH AMER PHYSICAL SOC ONE PHYSICS ELLIPSE, COLLEGE PK, MD 20740-3844 USA COLLEGE PK.

[75] M. Divis. Electronic structure and magnetism of ucoge from first principles. *Physica B-Condensed Matter*, 403(13-16):2505–2508, 2008. Times Cited: 7 Article English Divis, M Charles Univ Prague, Fac Math and Phys, Dept Condensed Matter Phys, Ke Karlovu 5, CR-12116 Prague 2, Czech Republic Cited References Count: 11 325ZI ELSEVIER SCIENCE BV.

[76] M. Samsel-Czekala, S. Elgazzar, P. M. Oppeneer, E. Talik, W. Walerczyk, and R. Troc. The electronic structure of ucoge by ab initio calculations and xps experiment. *Journal of Physics-Condensed Matter*, 22(1):015503, 2010. Times Cited: 3 Article English Samsel-Czekala, M IFW Dresden, Leibniz Inst Festkorper and Werkstoffforsch, PF 270116, D-01171 Dresden,

Germany Cited References Count: 27 534IV IOP PUBLISHING LTD DIRAC HOUSE, TEMPLE BACK, BRISTOL BS1 6BE, ENGLAND BRISTOL.

[77] P. de la Mora and O. Navarro. Electronic structure of the ferromagnetic superconductor ucoge from first principles. *Journal of Physics-Condensed Matter*, 20(28):285221, 2008. Times Cited: 4 Article English de la Mora, P Univ Nacl Autonoma Mexico, Fac Ciencias, Dept Fis, Apartado Postal 70 542, Mexico City 04510, DF, Mexico Cited References Count: 24 319QJ IOP PUBLISHING LTD DIRAC HOUSE, TEMPLE BACK, BRISTOL BS1 6BE, ENGLAND BRISTOL.

[78] K. Prokes and A. Gukasov. Magnetization densities in urhsi studied by polarized neutron diffraction. *Physical Review B*, 79(2):024406, 2009. J JAN.

[79] H. Nakotte, A. Purwanto, R. A. Robinson, Z. Tun, K. Prokess, Allen C. Larson, L. Havela, V. Sechovsky, H. Maletta, E. Bruck, and F. R. de Boer. Commensurate and incommensurate magnetic structures of unige. *Physical Review B*, 54(10):7201–7209, 1996. PRB.

[80] V. H. Tran, R. Troc, and G. Andre. Magnetic ordering in urhsi and urhge. *Journal of Magnetism and Magnetic Materials*, 186(1-2):81–86, 1998.

[81] F. Hardy, A. Huxley, J. Flouquet, B. Salce, G. Knebel, D. Braithwaite, D. Aoki, M. Uhlarz, and C. Pfleiderer. phase diagram of the ferromagnetic superconductor urhge. *Physica B: Condensed Matter*, 359-361(0):1111–1113, 2005.

[82] S. Sakarya, N. H. van Dijk, A. de Visser, and E. Brück. Dilatometry study of the ferromagnetic order in single-crystalline urhge. *Physical Review B*, 67(14):144407, 2003. PRB.

[83] Dai Aoki, Frederic Hardy, Atsushi Miyake, Valentin Taufour, Tatsuma D. Matsuda, and Jacques Flouquet. Properties of ferromagnetic superconductors. *Comptes Rendus Physique*, 12(5-6):573–583, 2011.

[84] Jiri Pospisil, Karel Prokes, Manfred Reehuis, Michael Tovar, Jana Poltierova Vejpravova, Jan Prokleska, and Vladimir Sechovsky. Influence of sample preparation technology and treatment on magnetism and superconductivity of ucoge. *Journal of the Physical Society of Japan*, 80 (Copyright (C) 2011 The Physical Society of Japan):084709, 2011.

[85] Jan Czochralski. Ein neues verfahren zur messung der kristallisationsgeschwindigkeit der metalle. *Zeitschrift fur Physikalische Chemie*, 92:219, 1918.

[86] Neil Ashcroft and David Mermin. *Solid State Physics*. Thomson Learning, 1976.

[87] V. Valvoda, M. Polcarová, and P. Lukác. *Základy strukturní analýzy*. Karolinum, 1992.

[88] http://www.bruker.com/.

[89] H. Rietveld. A profile refinement method for nuclear and magnetic structures. *Journal of Applied Crystallography*, 2(2):65–71, 1969.

[90] G. Caglioti, A. Paoletti, and F. P. Ricci. Choice of collimators for a crystal spectrometer for neutron diffraction. *Nuclear Instruments*, 3(4):223–228, 1958.

[91] Juan Rodriguez-Carvajal. Recent advances in magnetic structure determination by neutron powder diffraction. *Physica B: Condensed Matter*, 192(1-2):55–69, 1993.

[92] T. Roisnel and Juan Rodriguez-Carvajal. Winplotr: a windows tool for powder diffraction patterns analysis. In R. Delhez and E.J. Mittemeijer, editors, *EPDIC 7 - Seventh European Powder Diffraction Conference*. Trans Tech Publications.

[93] J. X. Boucherle, J. Y. Henry, R. J. Papoular, J. Rossat-Mignod, J. Schweizer, F. Tasset, and G. Uimin. Polarised neutron study of high-tc superconductors. *Physica B: Condensed Matter*, 192(1-2):25–38, 1993.

[94] R. Pike and P. Sabatier. *Scattering, Two-Volume Set*. 2002.

[95] R. J. Papoular and B. Gillon. Maximum entropy reconstruction of spin density maps in crystals from polarized neutron diffraction data. *EPL (Europhysics Letters)*, 13(5):429, 1990.

[96] Brenda Dougan and ZiLing Xue. Polarized neutron diffraction and its application to spin density studies. *Science in China Series B: Chemistry*, 52(12):2083–2095, 2009.

[97] E. Prince and International Union of Crystallo. *International Tables for Crystallography, Mathematical, Physical and Chemical Tables*. John Wiley and Sons, 2004.

[98] Tibor S. Koritsanszky and Philip Coppens. Chemical applications of x-ray charge-density analysis. *Chemical Reviews*, 101(6):1583–1628, 2001.

[99] http://www.ill.eu/?id=13322.

[100] http://www.ill.eu/?id=13268.

[101] www.qdusa.com.

[102] Y.S. Touloukian. *Thermophysical Properties of Matter: Thermal expansion: metallic elements and alloys, by Y. S. Touloukian and others*. IFI/Plenum, 1970.

[103] C.Y. Ho and R.E. Taylor. *Thermal Expansion of Solids*. Asm International, 1998.

[104] Ch Bittorf, S. Matthies, H. G. Priesmeyer, and R. Wagner. Diffractive determination of thermo-elastic single crystal constants using polycrystalline samples. i. thermal expansion of gamma-tial from 300 to 900k. *Intermetallics*, 7(3-4):251–258, 1999.

[105] John N. Fox. Measurement of thermal expansion coefficients using a strain gauge. *American Journal of Physics*, 58(9):875–877, 1990.

[106] T. E. Finke and T. G. Heberling. Determination of thermal-expansion characteristics of metals using strain gages. *Experimental Mechanics*, 18(4):155–158, 1978.

[107] Joseph Valentich. A vitreous silica tube dilatometer for the measurement of thermal expansion of solids from -195 to 1000 c. *Journal of Materials Science*, 14(2):371–378, 1979.

[108] J. D. James, J. A. Spittle, S. G. R. Brown, and R. W. Evans. A review of measurement techniques for the thermal expansion coefficient of metals and alloys at elevated temperatures. *Measurement Science and Technology*, 12(3):R1, 2001.

[109] M. Rotter, H. Muller, E. Gratz, M. Doerr, and M. Loewenhaupt. A miniature capacitance dilatometer for thermal expansion and magnetostriction. *Review of Scientific Instruments*, 69(7):2742–2746, 1998.

[110] H. Müller and M. Rotter. *Capacitance Dilatometer DIL20-11 - Users Manual*. 2012.

[111] G. Brandli and R. Griessen. Two capacitance dilatometers. *Cryogenics*, 13(5):299–302, 1973.

[112] Jan Genossar and Michael Steinitz. A tilted-plate capacitance displacement sensor. *Review of Scientific Instruments*, 61(9):2469–2471, 1990.

[113] R. Pott and R. Schefzyk. Apparatus for measuring the thermal expansion of solids between 1.5 and 380k. *Journal of Physics E: Scientific Instruments*, 16(5):444, 1983.

[114] C. R. Tilford and C. A. Swenson. Thermal expansions of solid argon, krypton, and xenon above 1 k. *Physical Review B*, 5(2):719–732, 1972. PRB.

[115] Goutam Dev Mukherjee, C. Bansal, and Ashok Chatterjee. Thermal expansion analysis of $fe_{3-x}mn_x$al alloys. *Physical Review B*, 58(10):6172–6179, 1998. PRB.

[116] L. Vegard. Die konstitution der mischkristalle und die raumfÃŒllung der atome. *Zeitschrift fur Physik A Hadrons and Nuclei*, 5(1):17–26, 1921.

[117] Beatriz Cordero, Veronica Gomez, Ana E. Platero-Prats, Marc Reves, Jorge Echeverria, Eduard Cremades, Flavia Barragan, and Santiago Alvarez. Covalent radii revisited. *Dalton Transactions*, 0(21):2832–2838, 2008.

[118] Anthony Arrott. Criterion for ferromagnetism from observations of magnetic isotherms. *Physical Review*, 108(6):1394–1396, 1957. PR.

[119] I. Yeung, R. M. Roshko, and G. Williams. Arrott-plot criterion for ferromagnetism in disordered systems. *Physical Review B*, 34(5):3456–3457, 1986. PRB.

[120] J. Prokleska, J. Pospisil, J. Vejpravova Poltierova, V. Sechovsky, and J. Sebek. Low temperature ac susceptibility of ucoge crystals. *Journal of Physics: Conference Series*, 200:012161, 2010.

[121] J. Mira, J. Rivas, F. Rivadulla, and M. A. Lopez Quintela. Identification of first- and second-order magnetic phase transitions in ferromagnetic perovskites. *Physica B: Condensed Matter*, 320(1-4):23–25, 2002.

[122] A. Gasparini, Y. K. Huang, N. T. Huy, J. C. P. Klaasse, T. Naka, E. Slooten, and A. de Visser. The superconducting ferromagnet ucoge. *Journal of Low Temperature Physics*, 161(1-2):134–147, 2010. Times Cited: 0 Article English de Visser, A Univ Amsterdam, Van der Waals Zeeman Inst, Valckenierstr 65, NL-1018 XE Amsterdam, Netherlands Cited References Count: 50 655AG SPRINGER/PLENUM PUBLISHERS 233 SPRING ST, NEW YORK, NY 10013 USA NEW YORK.

[123] V. H. Tran, R. Troc, and D. Urski. Electrical resistivity investigations of ut(si, ge) series. *Journal of Magnetism and Magnetic Materials*, 87(3):291–298, 1990.

[124] Javier Gonzalez-Platas and Juan Rodriguez-Carvajal. Gfourier, 2007.

[125] P. J. Brown, J.C. Matthewman, W.I.F. David, J.B. Forsyth, J.H. Matthewman, and J.P. Wright. The cambridge crystallographic subroutine library, 1999.

[126] N. Hessel Andersen. *Electrical Resistivity Investigations on Metallic Rare-Earths*, chapter 41, pages 373–387. Springer US, 1980.

[127] N. T. Huy, A. Gasparini, J. C. P. Klaasse, A. de Visser, S. Sakarya, and N. H. van Dijk. Ferromagnetic quantum critical point in urhge doped with ru. *Physical Review B*, 75(21): 212405, 2007. PRB.

[128] K. Prokes, A. de Visser, Y. K. Huang, B. Fak, and E. Ressouche. Anomalous spin distribution in the superconducting ferromagnet ucoge studied by polarized neutron diffraction. *Physical Review B*, 81(18):180407R, 2010. Times Cited: 1 Article English Prokes, K Helmholtz Zentrum Berlin Mat and Energy, Hahn Meitner Pl 1, D-14109 Berlin, Germany Cited References Count: 29 602LX AMER PHYSICAL SOC ONE PHYSICS ELLIPSE, COLLEGE PK, MD 20740-3844 USA COLLEGE PK.

9 Appendix A

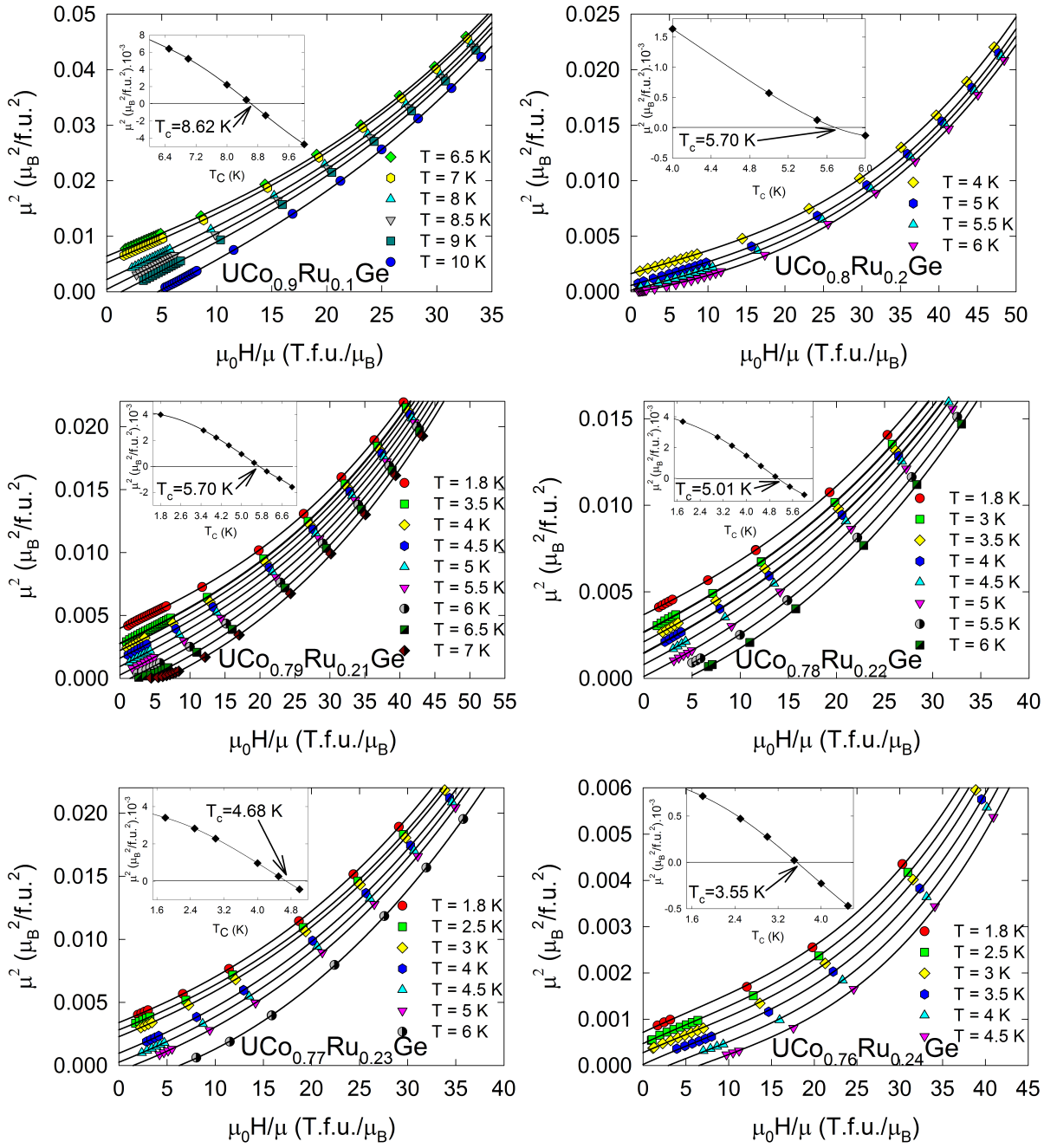

Figure 9.1: Arrott plots measured on the polycrystalline samples with different ruthenium content. Inset in each figure shows construction for the estimation of the Curie temperature.

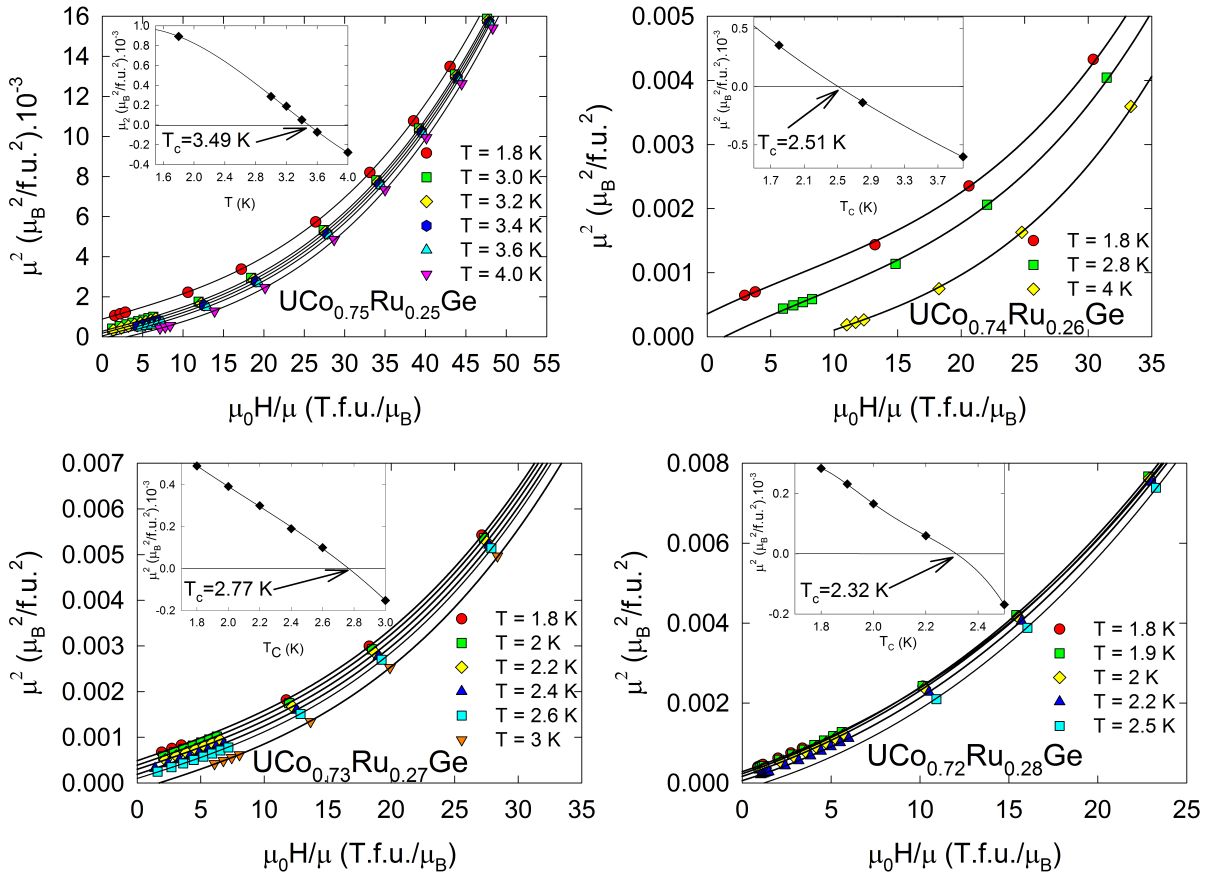

Figure 9.2: Arrott plots measured on the polycrystalline samples with different ruthenium content. Inset in each figure shows construction for the estimation of the Curie temperature.